Few-cycle pulse generation in the mid-infrared and THz spectral domains

PhD Thesis

Roland Flender

Supervisors:

Ádám Börzsönyi PhD, ELI ALPS, ELI-HU Nonprofit Kft.

Viktor Chikán PhD, Kansas State University

Doctoral School of Physics

Faculty of Science and Informatics

University of Szeged

Szeged

2022

Table of Contents

Frequently used acronyms and chemical formulas

AGS	silver gallium sulfide
Al_2O_3	sapphire
AOI	angle of incidence
AOPDF	acousto-optic programmable dispersive filter
BaF_2	barium fluoride
BBAR	broadband antireflection
BBO	beta barium borate
BSC	beam splitting cube
BWO	backward wave oscillator
CCD	charge-coupled device
CEP	carrier to envelope phase
CaF_2	calcium fluoride
CO_2	carbon dioxide
CPA	chirped pulse amplification
CW	continuous wave
DFG	difference frequncy generation
DcM	dichroic mirror
DM	dispersive mirror
eo	extreordinary
FEL	free-electron laser
FIR	far infrared
FOD	fourth order dispersion
FROG	second harmonic frequency-resolved optical gating
FTIR	Fourier-transform infrared spectroscopy
FTL	Fourier-transform limit
FWHM	full-width at half maximum
FWM	four-wave mixing
FWP	full wave plate
GaAs	gallium arsenide
GD	group delay
GDD	group delay dispersion
GaSe	gallium selenide
GVD	group velocity-dispersion
HHG	high harmonic generation
H_2O	water
HWP	half wave plate
IR	infrared
KBR	potassium bromide
KRS-5	thallium bromo iodide
LASER	light amplification by stimulated emission of radiation
LiF	lithium fluoride
LN	lithium niobate
LWIR	longwave infrared
MgF_2	magnesium fluoride
MIR	mid-infrared
MZI	Mach-Zehnder interferometer
NIR	near-infrared
o	ordinary
OAP	off-axis parabolic mirror
OPA	optical parametric amplification

OPCPA	optical parametric chirped pulse amplification
OPD	optical path difference
OR	optical rectification
OSA	optical spectrum analyzer
PC	personal computer
RMSD	root mean square deviation
ROC	radius of curvature
RP	relative phase
SFG	sum frequency generation
SHG	second harmonic generation
Si	silicon
SH-SRI	second harmonic assisted spectrally resolved interferometry
SPM	self-phase modulation
SRI	spectrally resolved interferometry
STD	standard deviation
SWIR	shortwave infrared
TEC	transverse electron current
THz	terahertz
THz-TDS	terahertz time-domain sprectoscopy
THG	third harmonic generation
TOD	third order dispersion
UV	ultra-violet
YAG	yttrium aluminum garnet
ZnS	zinc sulfide
ZnSe	zinc selenide

"In the beginning the Universe was created. This has made a lot of people very angry and been widely regarded as a bad move."

Douglas Adams

1. Introduction

The history of nonlinear optics started with the theory of two-photon absorption, which was predicted in *1931* by *Maria Goeppert Mayer* in her PhD thesis. However, the scientific community had to wait another thirty years for the first experimental evidence. The construction of the first laser (light amplification by stimulated emission of radiation) [1] in *1960* by *T. H. Maiman*, made it possible to develop light sources with sufficient intensity for nonlinear optics. *W. Kaiser* and *P. A. Franken* demonstrated two-photon absorption [2] and second harmonic generation (SHG) [3] in 1961. The development of laser technology led to important scientific breakthroughs in nonlinear optics. *Denes Gabor* won the Nobel Prize in Physics in *1971 "for his invention and development of the holographic method"* [4]. *R. Weiss*, *B. C. Barish* and *K. S. Thorne* were awarded the Nobel Prize in Physics in *2017 "for decisive contributions to the LIGO detector and the observation of gravitational waves"* [5]. Their scientific feat was indirectly made possible by the development of lasers. Finally, it must be mentioned that *G. Mourou* and *D. Strickland* shared the Nobel Prize in Physics in *2018 "for their method of generating high-intensity, ultrashort optical pulses"* [6].

Soon after the discovery of SHG, sum frequency generation (SFG) [7, 8] was demonstrated in *1962* by *M. Bass* and *R. C. Miller*. This nonlinear optical process allowed the development of tunable light sources in the ultraviolet (UV) spectral domain. During the SHG, two photons with equal frequencies ($\omega_1 = \omega_2$) are annihilated and one photon ($\omega_3 = 2 \times \omega_1$) with twice of the initial photons' frequency is generated. Similarly, during SFG, two photons with different frequencies ($\omega_1 \neq \omega_2$) are annihilated and one photon ($\omega_3 = \omega_1 + \omega_2$) with the sum of the initial photons' frequencies is generated. SHG can be considered as a degenerate case of SFG, where the initial photons' frequencies are equal. Another important nonlinear optical phenomenon is difference frequency generation (DFG) [9], which was demonstrated in *1963* by *A. W. Smith*. This nonlinear optical process allowed the development of tunable light sources in the infrared (IR) spectral domain. During DFG, from two photons with different frequencies ($\omega_1 > \omega_2$) the photon with the higher frequency (ω_1) is annihilated, and two other photons are generated (ω_2, $\omega_3 = \omega_1 - \omega_2$). The frequency of one photon equals the other initial photon's frequency (ω_2), therefore now there are two photons ($\omega_2 \rightarrow 2 \times \omega_2$) with the same frequency. The other photon's frequency is equal to the difference between the initial photons' frequency ($\omega_3 = \omega_1 - \omega_2$). Another nonlinear optical phenomenon is optical parametric amplification (OPA) [10, 11], which was presented in *1965* by *S. A. Akhmanov* and *J. A. Giordmaine*. During DFG, the aim is to generate the difference-frequency photon ($\omega_3 = \omega_1 - \omega_2$) of the two initial photons, however the aim during OPA is to

multiply/amplify the lower frequency photon ($\omega_2 \rightarrow 2\times\omega_2$) of the two initial photons This nonlinear optical process is able to effectively multiply/amplify the photons in the IR spectral domain.

G. Mourou and D. Strickland have made important contribution to nonlinear optics by the development of chirped pulse amplification (CPA) [12], which is also known as the "second-generation femtosecond technology" [13]. CPA allowed for the construction of laser systems with peak powers in the terawatt (TW) and petawatt (PW) ranges, generating unprecedented intensities to explore new depths in the field of nonlinear optics. The next important development step in the history of nonlinear optics came in 1992, when A. Dubietis, G. Jonusauskas and A. Piskarskas combined the OPA and the CPA phenomena and developed the optical parametric chirped pulse amplification (OPCPA) scheme [14], which led to a new technological era in laser development, the so called "third-generation femtosecond technology" [13]. This technology made available light sources with even more diverse spectral ranges and improved the spectral tunability of these light sources. The key advantage of this technology over previous ones was that these light sources could operate in different spectral domains simultaneously [13, 15-17]. In addition, if the pump and the signal beams are provided by the same source, the generation of passively stable carrier to envelope phase (CEP) idler beams [18] becomes possible, which is a very important property in relation to few-cycle laser pulses.

One of the current trends in few-cycle pulse development is to move towards longer central wavelengths, to the mid-infrared (MIR) spectral region, where OPCPA sources are routinely built nowadays [15, 19-21]. The advantage of a longer carrier wavelength in these systems is the ponderomotive potential. It is the cycle-averaged vibration energy of a charged particle in an oscillating electric field, and it scales with the square of the carrier wavelength. As a result of this scaling law, the secondary light source pumped with MIR laser systems produce higher cut-off photon energy for high harmonic generation (HHG) [22] and generate higher intensities for terahertz (THz) pulse generation [23-30]. Pulse duration can be further shortened by subsequent self-phase modulation (SPM) in bulk solid-state media [31-36] followed by re-compression. Re-compression can be achieved by propagating the pulses through optical materials with positive or negative group delay dispersion (GDD) available in the MIR spectral domain. Unfortunately, to achieve the shortest possible pulse duration, higher order derivatives of the spectral phase, such as the third order dispersion (TOD) must be compensated for. TOD compensation is challenging, since most of the transparent materials have positive TOD, which is a limiting factor in the postcompression of few-cycle pulses. A possible solution is the use of dispersive mirrors (DMs) [37-41], which can be designed to have an arbitrary spectral phase, and in this case they produce TOD with a negative sign.

THz covers the longwave infrared (LWIR) and the far infrared (FIR) spectral domains. Besides the fact that natural, incoherent THz radiation surrounds us as background radiation, there are several ways to generate coherent THz sources. An important scheme, which is the subject of my doctoral dissertation, is the two-color ionization in gases. This experimental approach results in

spectrally broad coherent THz radiation, which is a useful tool for THz time-domain spectroscopy (THz-TDS) [42] and a potential source as a probe in transient absorption spectroscopy. The THz radiation source is the transverse electron current (TEC) built up inside plasma [43-44], which is a renewable secondary source due to its generating medium: air. The important prerequisite of this THz generation method is the application of an asymmetric electromagnetic field, which accelerates the free electrons from tunnel ionization in one direction more effectively, than in the other, which develops a TEC inside the plasma [43-44]. The two most straightforward ways to achieve an asymmetric electromagnetic field are through the use of few-cycle and/or two-color pulses. The generation of few-cycle pulses is still a challenge, but there are continuous developments in this direction [31-36]. THz pulse generation based on the latter method was demonstrated successfully in 2000 by D. J. Cook [45]. Several scientific studies have shown that the efficiency of this type of THz generation increases with the carrier wavelength of the fundamental pulse [23-30] due to the ponderomotive potential.

The goal of my doctoral dissertation is to explore few-cycle pulse generation in the IR spectral region, especially in the MIR and the THz spectral domains. The scientific background on few-cycle MIR pulses and THz generation from two-color laser induced plasmas is presented in *Chapter 2.* The properties of the different spectral domains of the electromagnetic spectrum are discussed in *Chapter 2.1.* The fundamentals of nonlinear optics are presented in *Chapter 2.2.* The MIR OPCPA system at ELI ALPS Research Institute, which was the light source for the experimental work and the basis for the numerical simulation for THz pulse generation, is discussed in *Chapter 2.3.* The various methods for THz pulse generation, especially the two-color ionization in gases, are discussed in *Chapter 2.4.* The numerical simulations for THz pulse generation are described in detail in *Chapter 2.5.* The spectral phase measurement methods, the conventional spectrally resolved interferometry (SRI) and the second harmonic assisted SRI (SH-SRI) are presented in *Chapter 2.6.* After the discussion of the scientific backgrounds, the experimental and numerical methodology, as well as the new scientific findings of my doctoral work are presented in *Chapter 3.* The results with the conventional SRI and the SH-SRI are discussed in *Chapter 3.1.* The postcompression results of the MIR OPCPA light source at ELI ALPS Research Institute are presented in *Chapter 3.2.* The results of the numerical simulations for THz pulse generation with few-cycle, MIR pulses are discussed in *Chapters 3.3* to *3.6.* Finally, the summary of my doctoral dissertation in English and in Hungarian are presented in *Chapter 4* and *Chapter 5*, respectively. The experiments and calculations for this dissertation were performed at ELI ALPS Research Institute.

“Don't Panic.”

Douglas Adams

2. Scientific background

This chapter briefly summarizes the scientific background required to understand the results of my doctoral dissertation. The electromagnetic spectrum and its subdomains are discussed in *Chapter 2.1.* The fundamentals of nonlinear optics are presented in *Chapter 2.2.* The MIR OPCPA system, which was the light source for my experimental works and the basis for my numerical simulations for THz pulse generation, is discussed in *Chapter 2.3.* The various methods for THz pulse generation, especially the two-color ionization in gases, are discussed in *Chapter 2.4.* The numerical simulations for THz pulse generation are described in detail in *Chapter 2.5.* The spectral phase measurement techniques, the conventional SRI and the SH-SRI are presented in *Chapter 2.6.*

2.1. Electromagnetic spectrum

The electromagnetic spectrum stretches from subhertz over exahertz, and the different spectral domains within it can be classified according to the physical, chemical, and biological effects of the electromagnetic waves. To get an overview on how the different electromagnetic waves interact with matter, the spectral domains, including their boundaries, and their typical light-matter interactions are shown in *Table 2.1.*

The main topic of my doctoral dissertation focuses on the IR spectral domain, whose wavelength range starts at *0.7 μm and ends* at *1 mm*, which corresponds to a frequency range from *430 THz* to *300 GHz*, respectively. This spectral domain was first recognized by *Sir William Herschel* in *1800* [46]. During his experiments, he measured the temperature of each color of sunlight refracted by a prism with a series of thermometers. Herschel showed that the red portion of the spectrum heated up the corresponding thermometer more than the blue part. He also recognized that over the red part, the reference thermometer showed the highest temperature. From these results he concluded that there must be an invisible light beyond the red part of the visible spectrum, which is now called the IR spectral domain and has the following subdomains: the near infrared (NIR) from *0.7 μm* to *1.4 μm*, the shortwave infrared (SWIR) from *1.4 μm* to *3 μm*, the MIR or midwave-IR from *3 μm* to *8 μm*, the LWIR from *8 μm* to *15 μm* and the far infrared FIR from *15 μm* to *1 mm*.

Spectral domain	Wavelength [mm]	Frequency [Hz]	Light-matter interaction
Radio waves	*above* 10^3	*below* 3×10^8	plasma oscillation
Microwaves	10^3 *to* 1	3×10^{11} *to* 3×10^8	plasma oscillation, molecular rotation
Infrared	1 *to* 7×10^{-4}	4.3×10^{14} *to* 3×10^{11}	plasma oscillation (metals only), molecular rotation, molecular vibration
Visible	7×10^{-4} *to* 4×10^{-4}	7.5×10^{14} *to* 4.3×10^{14}	plasma oscillation (metals only), molecular electron excitation
Ultraviolet	4×10^{-4} *to* 10^{-5}	3×10^{16} *to* 7.5×10^{14}	molecular valence electron excitation and ejection, atomic valence electron excitation and ejection
X-rays	10^{-5} *to* 10^{-8}	3×10^{19} *to* 3×10^{16}	atomic core electron excitation and ejection
Gamma rays	*below* 10^{-8}	*above* 3×10^{19}	atomic core electron ejection, atomic nuclei excitation and dissociation

Table 2.1: The spectral domains of the electromagnetic spectrum, their boundaries, and typical light-matter interactions

The IR spectrum has numerous useful applications in spectroscopy, metrology, climatology, astronomy, and defense. IR spectroscopy is a very useful method when it comes to the identification, quantification, and characterization of materials as it has high chemical specificity and is a non-destructive analytical tool. The NIR photons' energy is in the same range as the

transitional energy between the vibrational states of matter, which facilitates their investigation via IR spectroscopy. Similarly, the MIR photons have lower energy, and are therefore suitable to map the fundamental rotational and vibrational states of matter. As we continue to longer wavelengths, the FIR photons allow us to directly excite the low-frequency vibration states of solids and the rotational states of molecules in the gas phase. With the typical IR spectroscopic absorption technique, the transmission of the sample, illuminated with IR radiation, carries quantitative and qualitative information about the sample, which can be deduced from the position and magnitude of spectral attenuation. The measurement can be performed with either monochromatic or multichromatic radiation, but the latter method is preferred due to its multiple advantages. One of the most well-known techniques available for the analysis of changes in the IR spectral domain is called Fourier transform infrared spectroscopy (FTIR) [47]. In this case the broadband light source illuminates the sample and is analyzed by an interferometer, typically a Michelson type. The interferometer splits the incoming light into two parts, which create interference at the output of the interferometer as a function of the optical path difference (OPD) between the two arms. The spectral composition of the beam is recovered through Fourier analysis from the interferograms recorded at different OPDs by a personal computer (PC). This method has several advantages over other methods based on monochromatic light sources: The first one is the multiplex or *Fellgett's* advantage. Information is collected simultaneously at all wavelengths, wherefore the signal-to-noise ratio is higher at any given measurement time. The second one is the throughput or *Jacquinot's* advantage. In the case of monochromatic measurements, the monochromator has slits at the entrance and at the exit, which thoroughly limits the amount of useful light. In contrast, there is no such restriction when an interferometer is used. Therefore, the signal-to-noise ratio will be higher at any given spectral resolution. The last one is the wavelength accuracy or *Connes'* advantage. In case of FTIR, the wavelength is calibrated to the internal laser beam, which provides and internal reference. This method is much more accurate and stable than the monochromatic devices, where the scale highly depends on the mechanical position of the diffraction grating.

In THz spectroscopy, THz-TDS [48] is a widespread measurement method. It is similar to FTIR in the sense that the measurements are also performed in the time domain instead of the spectral domain. However, in contrast to FTIR, in addition to the amplitude information, the phase information also can be recovered, which allows us to extract the complex refractive index of materials interacting with the THz beam. The schematic figure of the THz-TDS method is shown in *Figure 2.1*. In this method, the driving system is usually an intensive few-cycle laser system. The pulses are divided into two parts: the more intense one generates the THz pulse, while the other detects it. The THz pulse can be generated with several methods, a more detailed description of which can be found in *Chapter 2.4*. During the process, the THz beam is typically collimated with an off-axis parabolic (OAP) mirror and refocused on the sample with another OAP. After the sample, the THz beam is collimated again and focused on the THz detector together with the reference beam. The signal from the detector is digitized and analyzed by a PC, which also controls the motorized delay stage in the reference beam path. The latter is needed because – as I mentioned earlier – the measurement takes place in the time domain instead of the spectral domain.

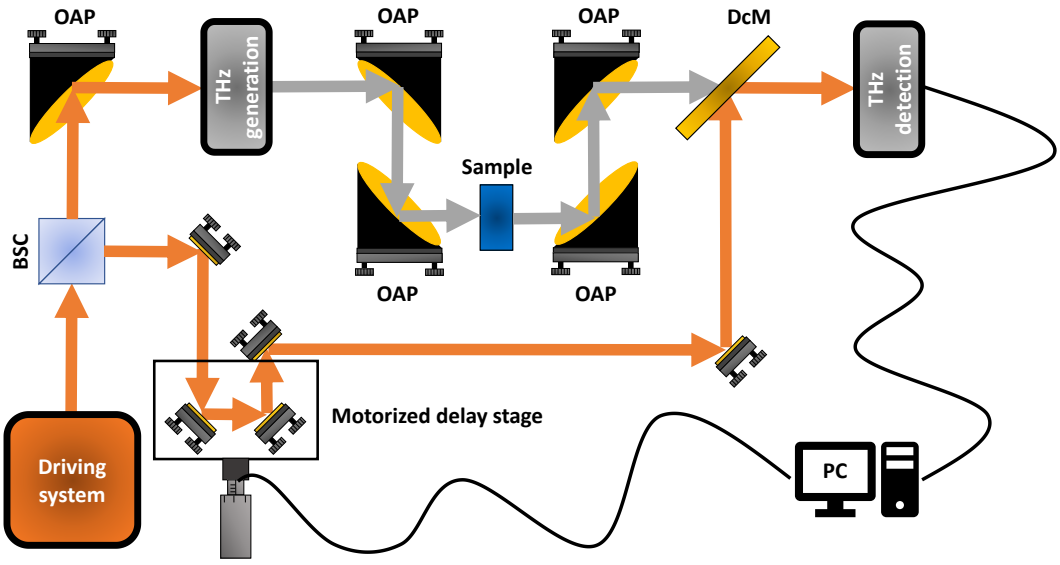

Figure 2.1: The schematic figure of the THz-TDS method. BSC – beam splitting cube, OAP – off-axis parabolic mirror, DcM – dichroic mirror, PC – personal computer

THz radiation has several advantages in the field of spectroscopy: for example, most packaging materials, such as paper, cardboard, and textile, are transparent in this spectral range [49]. Furthermore, due to its low photon energy, it is non-ionizing radiation, which makes it suitable for testing chemical and biological samples without risk [49]. Finally, many materials, such as explosives, narcotics, and medicines, have unique spectral characteristics in the THz spectral domain, which allows for their identification [49]. Due to the above properties, this type of spectroscopy method has undergone significant development in the recent past.

2.2. Nonlinear optics

When the dielectric material is irradiated with an electic field, it will react to it and this reaction is called the dielectric polarization. If the excitation is weak, the response will be linear. In this case, we are talking about linear optics. The dielectric polarization of the dielectric material is defined as follows:

$$P(t) = \epsilon_0 \chi^{(1)} E(t), \tag{2.1}$$

where ε_0 is the vacuum's permittivity (8.85×10^{-12} *F/m*), $\chi^{(1)}$ is the first order of susceptibility and *E(t)* is the applied electric field. When the electric field is intense enough, *Equation 2.1* changes as follows:

$$P(t) = \varepsilon_0\left(\chi^{(1)}E(t) + \chi^{(2)}E^2(t) + \chi^{(3)}E^3(t) + \cdots\right), \tag{2.2.a}$$

$$P_1(t) = \epsilon_0 \chi^{(1)} E(t), \tag{2.2.b}$$

$$P_2(t) = \epsilon_0 \chi^{(2)} E^2(t), \tag{2.2.c}$$

$$P_3(t) = \epsilon_0 \chi^{(3)} E^3(t), \tag{2.2.d}$$

where $\chi^{(2)}$ and $\chi^{(3)}$ are the second and the third orders of susceptibility, respectively. The symbol $\chi^{(1)}$ is in the order of unity, while $\chi^{(2)}$ and $\chi^{(3)}$ are in the order of 1.94×10^{-12} *m/V* and 3.76×10^{-24} m^2/V^2, respectively [50]. Based on the above, the second term of the dielectric polarization ($P_2(t)$) is comparable to the first term ($P_1(t)$), when the applied electric field is in the order of 5.14×10^{11} *V/m*, which is the atomic unit of the electric field [50]. Likewise, the third term of dielectric polarization ($P_3(t)$) is comparable to $P_1(t)$, when the applied electric field is in the order of 2.64×10^{23} *V/m*, which is the square of the atomic unit of the electric field [50]. The following subchapters discuss the different second and third order nonlinear optical processes.

2.2.1.Second order nonlinear processes

I must start this chapter with an important note: second order nonlinear optical processes only happen in materials without central symmetry, otherwise $\chi^{(2)}$ is zero. First, let us consider a monochromatic electric wave:

$$E(t) = Ee^{-i\omega t} + Ee^{i\omega t}\,, \tag{2.3}$$

where ω is the angular frequency. The second term is the complex conjugate of the first term. If we apply *Equation 2.3* in *Equation 2.2.c*, we obtain the following:

$$\begin{aligned} P_2(t) &= \varepsilon_0\chi^{(2)}E^2(t) = \varepsilon_0\chi^{(2)}\left(Ee^{-i\omega t} + Ee^{i\omega t}\right)^2 \\ &= \varepsilon_0\chi^{(2)}\left(2\langle E\rangle^2 + E^2e^{-i2\omega t} + E^2e^{i2\omega t}\right). \end{aligned} \tag{2.4}$$

The first term of *Equation 2.4* is the so-called optical rectification (OR), which is a static electric field. The second term of *Equation 2.4* is the SHG, and the third term is the complex conjugate of the second term. As mentioned earlier, during this phenomenon two photons with equal frequency are annihilated ($\omega_1 = \omega_2$) and one photon with twice of the initial photons' frequency is generated ($\omega_3 = 2\times\omega_1$). The schematic process of SHG is shown in *Figure 2.2*.

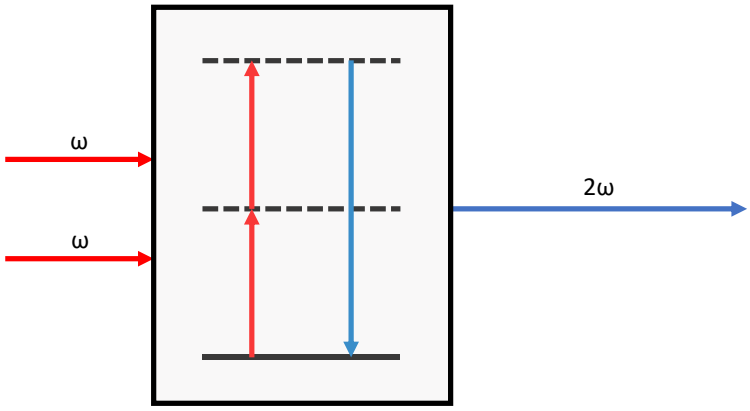

Figure 2.2: The schematic process of SHG. The solid line is the ground level, and the dashed lines are virtual levels.

In the next step let us consider a dichromatic ($\omega_1 \neq \omega_2$) electric wave:

$$E(t) = E_1e^{-i\omega_1 t} + E_2e^{-i\omega_2 t} + E_1e^{i\omega_1 t} + E_2e^{i\omega_2 t}\,, \tag{2.5}$$

where the first term is an electric wave with ω_1 angular frequency and the second term is another electric wave with ω_2 angular frequency. The last two terms are the complex conjugate of the first two terms. If we apply *Equation 2.5* in *Equation 2.2.c*, we obtain following:

$$P_2(t) = \varepsilon_0\chi^{(2)}E^2(t) = \varepsilon_0\chi^{(2)}\left(E_1e^{-i\omega_1 t} + E_2e^{-i\omega_2 t} + E_1e^{i\omega_1 t} + E_2e^{i\omega_2 t}\right)^2$$

$$= \varepsilon_0\chi^{(2)}(2\langle E_1\rangle^2 + 2\langle E_2\rangle^2) \quad (2.6.a)$$

$$+\varepsilon_0\chi^{(2)}\left(E_1^2e^{-i2\omega_1 t} + E_1^2e^{i2\omega_1 t}\right) \quad (2.6.b)$$

$$+\varepsilon_0\chi^{(2)}\left(E_2^2e^{-i2\omega_2 t} + E_2^2e^{i2\omega_2 t}\right) \quad (2.6.c)$$

$$+\varepsilon_0\chi^{(2)}\left(E_1E_2e^{-i(\omega_1+\omega_2)t} + E_1E_2e^{i(\omega_1+\omega_2)t}\right) \quad (2.6.d)$$

$$+\varepsilon_0\chi^{(2)}\left(E_1E_2e^{-i(\omega_1-\omega_2)t} + E_1E_2e^{i(\omega_1-\omega_2)t}\right), \quad (2.6.e)$$

where *Equation 2.6.a* is the OR of the dichromatic wave, while *Equation 2.6.b* and *Equation 2.6.c* are the SHG of the electric waves. *Equation 2.6.d* is the SFG. As mentioned earlier, during this process two photons with different frequencies ($\omega_1 \neq \omega_2$) are annihilated and one photon with the sum frequency ($\omega_3 = \omega_1 + \omega_2$) of the initial photons' frequencies is generated. The schematic process of SFG is shown in *Figure 2.3*.

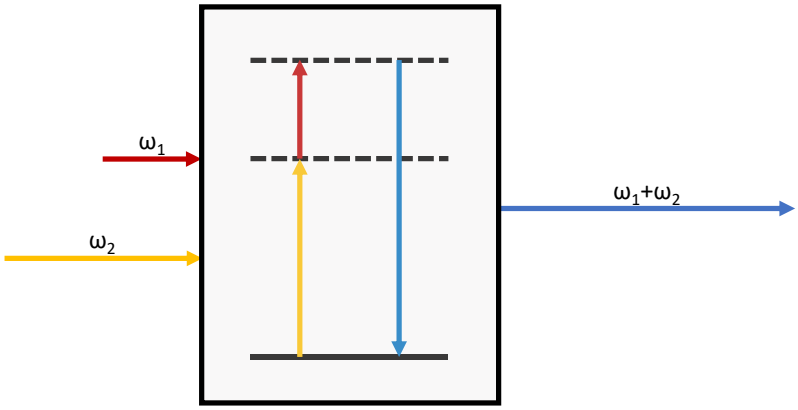

Figure 2.3: The schematic process of SFG. The solid line is the ground level, and the dashed lines are virtual levels.

Equation 2.6.e is the DFG, which phenomenon starts with two photons ($\omega_1 > \omega_2$). During the process, the higher frequency photon (ω_1) is annihilated, and two photons (ω_2, $\omega_3 = \omega_1 - \omega_2$) are generated, one with the frequency equaling the frequency of the lower frequency photon (ω_2) and another with the difference frequency ($\omega_3 = \omega_1 - \omega_2$) of the initial photons. As one can see, the DFG process multiplies/amplifies the lower frequency photon (ω_2), therefore it is also called OPA. The schematic process of DFG is shown in *Figure 2.4.* The SFG and DFG are practical solutions to generate tunable sources in the UV or in the IR spectral domains. The combination of the OPA and CPA schemes are the so-called OPCPA [14], where the pulses are stretched before the OPA process and are recompressed after it. Thanks to this, higher peak powers become available compared to the conventional OPA.

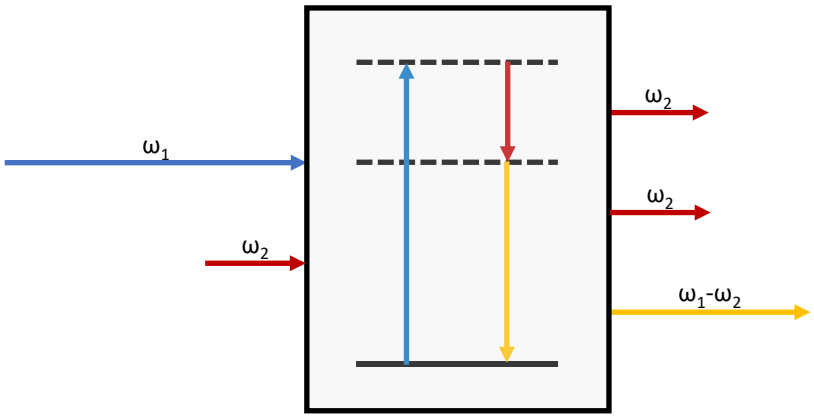

Figure 2.4: The schematic process of DFG. The solid line is the ground level, and the dashed lines are virtual levels.

As one can see, there are four different second order nonlinear optical processes (OR, SHG, SFG and DFG), however usually only one of them is intense enough to generate a significant amount of photons. The energy and the impulse conversion determine which process is the dominant:

$$\hbar\omega_p = \hbar\omega_s + \hbar\omega_i \,, \tag{2.7.a}$$

$$n(\omega_p)\hbar\omega_p/_c = n(\omega_s)\hbar\omega_s/_c + n(\omega_i)\hbar\omega_i/_c \,, \tag{2.7.b}$$

where $\hbar$ is the Planck constant over 2π (1.05×10^{-34} *J/s*), c is the speed of light (3.00×10^{8} *m/s*) and $n(\omega)$ is the material's refractive index. *Equations 2.7.a* and *2.7.b* are usually satisfied for only second order nonlinear optical process.

2.2.2.Third order nonlinear processes

In contrast to the second order nonlinear optical processes, the third order nonlinear processes take place in any material. First, let us consider a monochromatic electric wave. If we apply *Equation 2.3* in *Equation 2.2.d*, we obtain the following

$$P_3(t) = \varepsilon_0\chi^{(3)}E^3(t) = \varepsilon_0\chi^{(3)}\left(Ee^{-i\omega t} + Ee^{i\omega t}\right)^3$$
$$= \varepsilon_0\chi^{(3)}\left(E^3e^{-i3\omega t} + 3E^3e^{-i\omega t} + E^3e^{i3\omega t} + 3E^3e^{i\omega t}\right). \tag{2.8}$$

The first term of *Equation 2.8* is the third harmonic generation (THG). During this process, three photons with the same frequency are annihilated ($\omega_1 = \omega_2 = \omega_3$) and a single photon with a frequency equaling three times the initial frequency is generated ($\omega_4 = 3\times\omega_1$). The schematic process of THG shown in *Figure 2.5*.

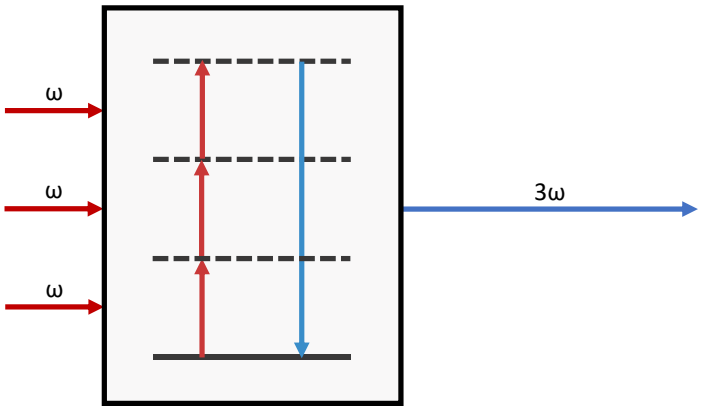

Figure 2.5: The schematic process of THG. The solid line is the ground level, and the dashed lines are virtual levels.

If we apply *Equation 2.3* in *Equation 2.2* and only consider $P_1(t)$ and $P_3(t)$, we obtain the following equation:

$$P(t) = \varepsilon_0\chi^{(1)}\left(Ee^{-i\omega t} + Ee^{i\omega t}\right)$$
$$+\varepsilon_0\chi^{(3)}\left(E^3e^{-i3\omega t} + 3E^3e^{-i\omega t} + E^3e^{i3\omega t} + 3E^3e^{i\omega t}\right), \quad (2.9)$$

where the first term of *Equation 2.9* is $P_1(t)$. As mentioned earlier, the second term is the THG. Let us take a closer look at the second term and extract the common parts. Then we obtain the following equation:

$$P(t) = \varepsilon_0(\chi^{(1)} + 3\langle E\rangle^2\chi^{(3)}) \times \left(Ee^{-i\omega t} + Ee^{i\omega t}\right)$$
$$+\varepsilon_0\chi^{(3)}\left(E^3e^{-i3\omega t} + E^3e^{i3\omega t}\right). \quad (2.10)$$

The $(\chi^{(1)}+3\langle E\rangle^2\chi^{(3)})$ part is replaceable with the expression of χ_{eff}, which is connected to the refractive index of the material as follows:

$$n^2 = 1 + \chi_{eff} = 1 + \chi^{(1)} + 3\langle E\rangle^2\chi^{(3)}. \quad (2.11)$$

A material's refractive index can be characterized with a linear refractive index (n_0), which is constant and with a nonlinear refractive index (n_2), which depends on the intensity. The common expression of the refractive index is the following:

$$n = n_0 + n_2 I = n_0 + n_2\langle E\rangle^2. \quad (2.12)$$

Let us square *Equation 2.12* and substitute it in *Equation 2.11*. After neglecting the fourth order terms, we get the following expression:

$$n_0^2 + 2n_0n_2\langle E\rangle^2 = 1 + \chi^{(1)} + 3\langle E\rangle^2\chi^{(3)}. \quad (2.13)$$

From *Equation 2.13* the n_0 and n_2 can be expressed as follow:

$$n_0 = \sqrt{1 + \chi^{(1)}}, \quad (2.14.a)$$

$$n_2 = {}^{3\chi^{(3)}}\Big/_{2n_0}. \quad (2.14.b)$$

Based on the above, the second term of *Equation 2.9* is responsible for the n_2 index, which is connected to $\chi^{(3)}$.

Let us briefly talk about some of the consequences of n_2. First, we must discuss the phenomenon of self-focusing, which was predicted in the early *1960s* [51, 52] and demonstrated later in the same decade [53, 54]. Due to n_2, the refractive index of the material temporary changes, when high intensity beams propagate through it. When the intensity profile of the beam is inhomogeneous, the refractive index profile will be also inhomogeneous. Thanks to this, most materials act like a focusing lens, when they interact with high peak power pulses. If the beam's intensity is greater than the critical peak power (P_{cr}), it will be self-focusing after a certain propagation distance. This can be described as follows:

$$P_{cr} = {\alpha\lambda^2}/{4\pi n_0 n_2}\,, \tag{2.15}$$

where λ is the carrier wavelength of the beam and α is a constant, characteristic of the intensity profile of the beam. In case of a Gaussian intensity profile, the value of α is *1.8962* [55].

Another effect of n_2 is SPM, which was first demonstrated in *1967* [56] by *F. Shimizu*. When pulses propagate through matter, their spectral phase shifts as follows:

$$\delta\varphi(t) = {n(t)d\omega}/{c}\,, \tag{2.16}$$

where *d* is the material's thickness. If we substitute *n* from *Equation 2.12*, we get the following:

$$\delta\varphi(t) = {n_0 d\omega}/{c} + {n_2 I(t) d\omega}/{c}\,, \tag{2.17}$$

where the first term is the linear and the second term is the nonlinear spectral phase shift. The first time derivate of *Equation 2.17* gives us the angular frequency shift as follows:

$$\delta\omega(t) = {d\delta\varphi(t)}/{dt} = {dI(t)}/{dt}\,.\,{n_2 d}/{c}\,. \tag{2.18}$$

Equation 2.18 clearly shows that ω shifts depending on the temporal intensity profile of the pulse. This process is typically characteristic of ultrashort pulses, where the temporal intensity profile changes rapidly. Thanks to this, the ω of the ultrashort pulses' front and back parts shift to higher and lower frequencies, respectively. This leads to spectral broadening. With proper, subsequent recompression this phenomenon can shorten the pulse duration down to the few-cycle regime [31-36].

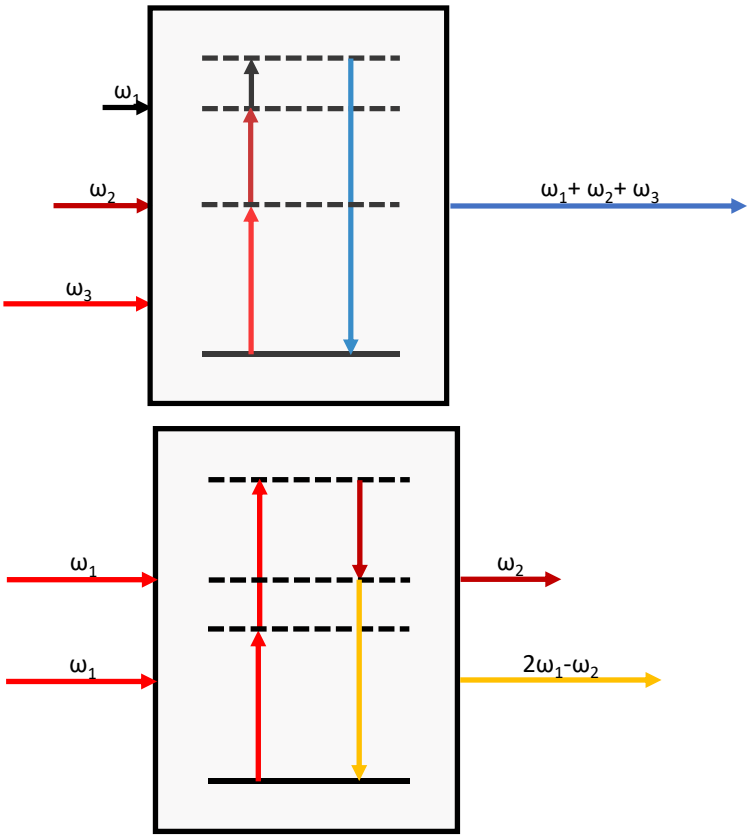

Figure 2.6: The schematic process of FWM. The solid line is the ground level, and the dashed lines are virtual levels.

Let us now consider the general case of a trichromatic ($\omega_1 \neq \omega_2 \neq \omega_3$) electric wave:

$$E(t) = E_1 e^{-i\omega_1 t} + E_2 e^{-i\omega_2 t} + + E_3 e^{-i\omega_3 t} + c.c\,, \tag{2.19}$$

where the first three terms are the electric waves with ω_1, ω_2 and ω_3 angular frequencies, respectively. The symbol *c.c* is the complex conjugate of the first three terms. If we apply *Equation 2.19* in *Equation 2.2.c*, we obtain the following equation:

$$P_3(t) = \varepsilon_0 \chi^{(3)} E^3(t) \tag{2.20}$$

$$= \varepsilon_0 \chi^{(3)} \left(E_1 e^{-i\omega_1 t} + E_2 e^{-i\omega_2 t} + E_3 e^{-i\omega_3 t} + c.c.\right)^3$$

$$= \varepsilon_0 \chi^{(3)} \left(E_1^3 e^{-i3\omega_1 t} + E_2^3 e^{-i3\omega_2 t} + E_3^3 e^{-i3\omega_3 t} + c.c.\right)$$

$$+\varepsilon_0 \chi^{(3)} \left(3E_1^2 E_2 e^{-i(2\omega_1 \pm \omega_2)t} + 3E_1^2 E_3 e^{-i(2\omega_1 \pm \omega_3)t} + c.c.\right)$$

$$+\varepsilon_0 \chi^{(3)} \left(3E_2^2 E_1 e^{-i(2\omega_2 \pm \omega_1)t} + 3E_2^2 E_3 e^{-i(2\omega_2 \pm \omega_3)t} + c.c.\right)$$

$$+\varepsilon_0 \chi^{(3)} \left(3E_3^2 E_1 e^{-i(2\omega_3 \pm \omega_1)t} + 3E_3^2 E_2 e^{-i(2\omega_3 \pm \omega_2)t} + c.c.\right)$$

$$+\varepsilon_0 \chi^{(3)} \left(3E_1 \langle E_1 \rangle^2 e^{-i\omega_1 t} + 6E_1 \langle E_2 \rangle^2 e^{-i\omega_1 t} + 6E_1 \langle E_3 \rangle^2 e^{-i\omega_1 t} + c.c.\right)$$

$$+\varepsilon_0 \chi^{(3)} \left(6E_2 \langle E_1 \rangle^2 e^{-i\omega_2 t} + 3E_2 \langle E_2 \rangle^2 e^{-i\omega_2 t} + 6E_2 \langle E_3 \rangle^2 e^{-i\omega_2 t} + c.c.\right)$$

$$+\varepsilon_0\chi^{(3)}\left(6E_3\langle E_1\rangle^2 e^{-i\omega_3 t}+6E_3\langle E_2\rangle^2 e^{-i\omega_3 t}+3E_3\langle E_3\rangle^2 e^{-i\omega_3 t}+c.c.\right)$$
$$+\varepsilon_0\chi^{(3)}\left(6E_1E_2E_3e^{-i(+\omega_1+\omega_2+\omega_3)t}+c.c.\right)$$
$$+\varepsilon_0\chi^{(3)}\left(6E_1E_2E_3e^{-i(+\omega_1+\omega_2-\omega_3)t}+c.c.\right)$$
$$+\varepsilon_0\chi^{(3)}\left(6E_1E_2E_3e^{-i(+\omega_1-\omega_2+\omega_3)t}+c.c.\right)$$
$$+\varepsilon_0\chi^{(3)}\left(6E_1E_2E_3e^{-i(-\omega_1+\omega_2+\omega_3)t}+c.c.\right).$$

As one can see, in this case *22* different frequency components can be generated. The general name of this process is four-wave mixing (FWM). Two schematic processes of FWM are shown in *Figure 2.6.*

2.3. The applied MIR OPCPA system

In this chapter, I briefly describe the applied MIR OPCPA system, which is developed together by Fastlite and ELI ALPS, the full description is available in the literature [21, 57]. My experimental works were done with this light source and the parameters of my numerical simulations were based on it too, that is why I felt it is important to dedicate a separate chapter to this system. The OPCPA system is pumped with an ytterbium-yttrium aluminum garnet (Yb-YAG) thin-disk regenerative amplifier (*Trumpf Scientific Lasers – Dira-200-100*), which is seeded by a preamplified fiber oscillator. The pump source delivers pulses with *2 mJ* energy at *100 kHz* repetition rate (P_{avg}=*200 W*). The central wavelength is around *1030 nm* and the pulse duration is around *1.1 ps* full-width at half maximum (FWHM); both parameters are defined by the emission spectrum of the Yb-YAG. The spatial profile of the pump source is almost Gaussian (M^2<*1.3*).

The optical layout of the OPCPA system is presented in *Figure 2.7*. A small portion of the pump beam (*~10 μJ*) is focused in a *10 mm* thick YAG crystal, where the filamentation occurs. The spectrum is broadened over *2 μm* and the *1.3–1.9 μm* part is shaped by a lithium niobate ($LiNbO_3$ or LN) acousto-optic programmable dispersive filter (AOPDF) (*Fastlite – Dazzler*). AOPDF is responsible for several tasks, including spectral selection, pulse-stretching, high order spectral phase precompensation and finally the stabilization and the control of the CEP. After this, the already shaped and stretched seed and another portion of the pump beam (*~25 μJ*) are used for DFG in a *1 mm* thick magnesium oxide (MgO) doped, periodically poled LN (PPLN) nonlinear crystal. The carrier wavelength of the idler pulse is around *3.2 μm* and extends from *2.7 μm* to *3.6 μm*. The pump, the signal and the idler beams are separated with two DcMs. The first one separates the pump beam from the signal and idler beams, while the second one separates the signal and idler beams. The pulse energy after the DFG stage is *0.9 μJ*. If the pump and the signal beams originate from the same source, the idler beam is passively CEP stable after DFG [18]. After the DFG stage, the idler beam is further amplified in the following three OPA stages. The second stage (OPA2 in *Figure 2.7*) is pumped with *125 μJ* pulse energy and the applied nonlinear crystal is *0.7 mm* thick MgO-PPLN. After this stage, another two DcMs are used to separate the beams. The pulse energy after the OPA2 stage is *8 μJ*. The third OPA stage (OPA3 in *Figure 2.7*) is pumped with *400 μJ* pulse energy and the applied nonlinear crystal is *1.5 mm*

thick LN. In this stage a non-collinear arrangement is used, which means that the beams propagate in different directions, therefore no DcMs are required for separation. The pulse energy after the OPA3 stage is *40 μJ*. The fourth and final OPA stage (OPA4 in *Figure 2.7*) is pumped with *1.4 mJ* pulse energy, and the applied nonlinear crystal is *1.5 mm* thick LN. In this stage, we also use a non-collinear arrangement. The pulse energy after the OPA4 stage is *165 μJ*.

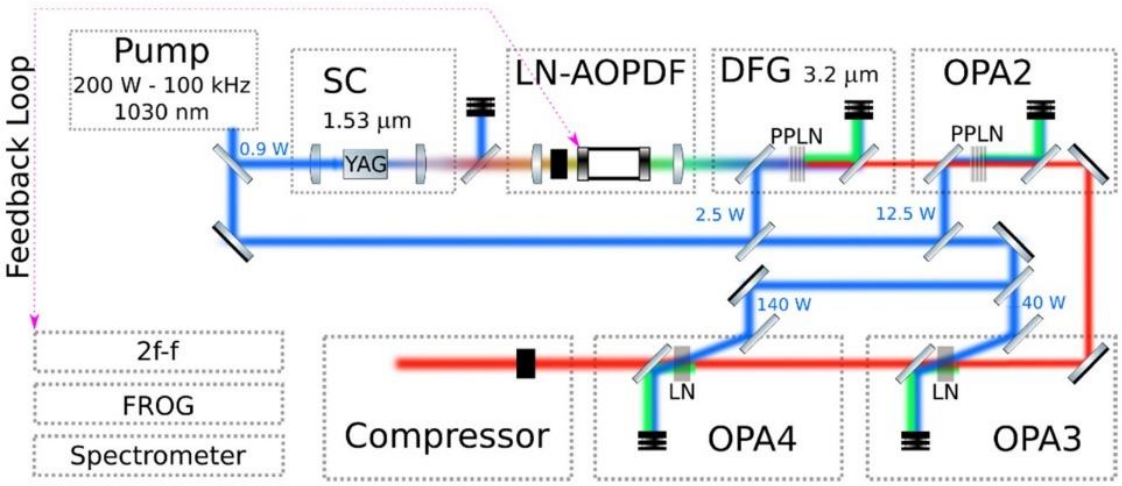

Figure 2.7: The optical layout of the MIR OPCPA system. SC – supercontinuum generation. LN-AOPDF – $LiNbO_3$ acousto-optic programmable dispersive filter. DFG – difference-frequency generation. OPA – optical parametric amplifier. 2f-f – collinear "2f-to-f" interferometer. FROG – scanning second-harmonic frequency-resolved optical gating. PPLN – periodically poled MgO:LiNbO3 crystal. LN – bulk LiNbO3 crystal. Blue – 1.03 μm. Green – <2.06 μm. Red – >2.06 μm. [21]

Figure 2.8 shows the spectrum at the output of the MIR OPCPA system. The measurement duration was *8 h* and a single spectrum was recorded every minute. The spectrum extends from *2.8 μm* to *3.7 μm*. The modulations in the spectrum at *2.8–2.9 μm* reveal water vapor absorption. *Figure 2.8.a* is an overlay of the spectrum from the *8 h* measurement. Given the very small fluctuations of the spectral intensity, the authors of the above-mentioned articles computed and plotted the probability density function of the spectral intensity. The color scale is a logarithmic scale and spans over several orders of magnitude. *Figure 2.8.b* shows in a more conventional way the stability of the spectral shape over more than *8 h*.

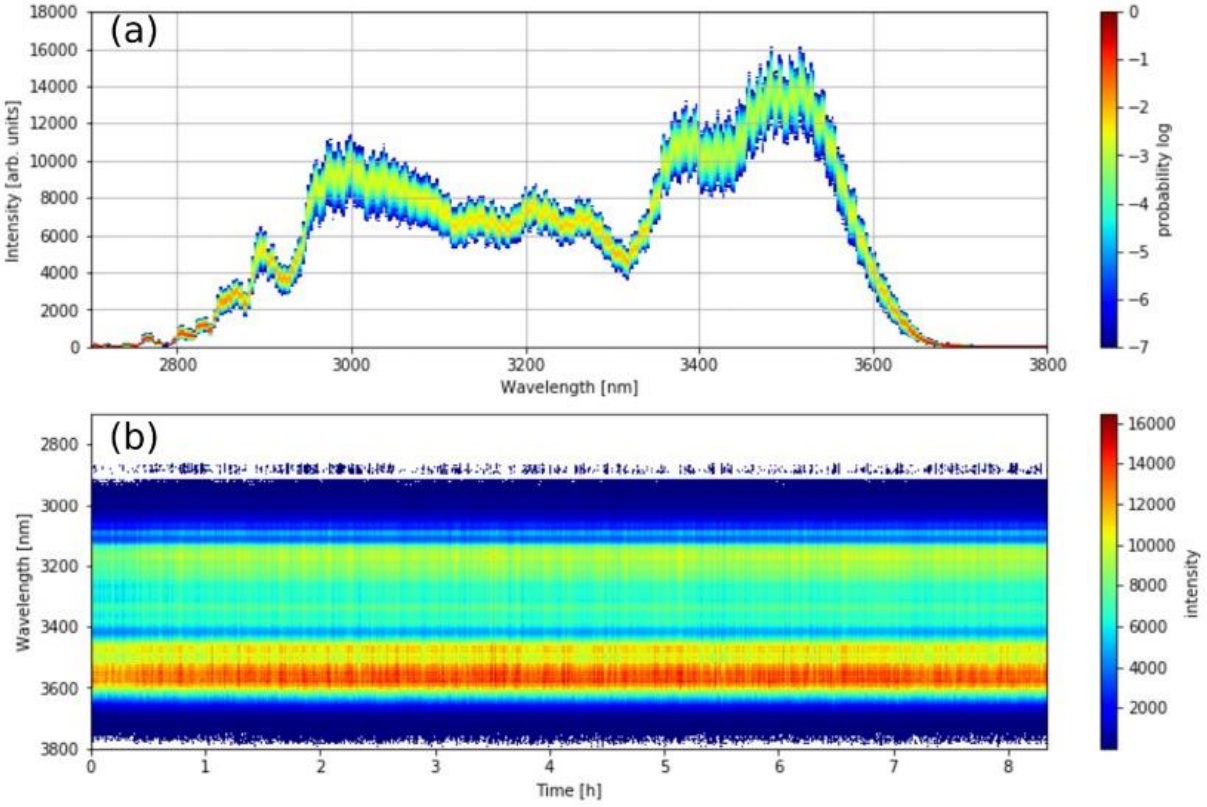

Figure 2.8: a.) Overlay of 500 output spectra taken during 8 hours. Each column is a histogram of intensity computed for a particular wavelength. b.) Output spectrum as a function of time. [21]

In the same articles [21, 57], SH frequency-resolved optical gating (FROG) [58-60] was used to characterize the temporal profile of the pulse at the output of the system. (The results are shown in *Figure 2.9.*) In this technique, the measured pulse is split into two beams, which are focused into a nonlinear crystal in a non-collinear arrangement. The type of the crystal depends on the central wavelength of the measured pulse. The nonlinear crystal generates SHG and SFG simultaneously, which propagate in different directions due to the non-collinear arrangement. The spectrum of the SFG measured as a function of the time delay between the two beams, which is called FROG trace (see in *Figure 2.9.a).* An algorithm numerically simulates the FROG trace and iteratively changes the input parameters (spectral phase and intensity) to minimize the difference between the measured and simulated traces. If the difference is below a threshold value, which can be set in the program, the algorithm stops. The retrieved pulse duration is *38.2 fs* FWHM with a Fourier transform limit (FTL) of *35.5 fs* FWHM. Since the duration of an optical cycle at *3.2 μm* is *10.7 fs*, pulse duration is less than four optical cycles [21].

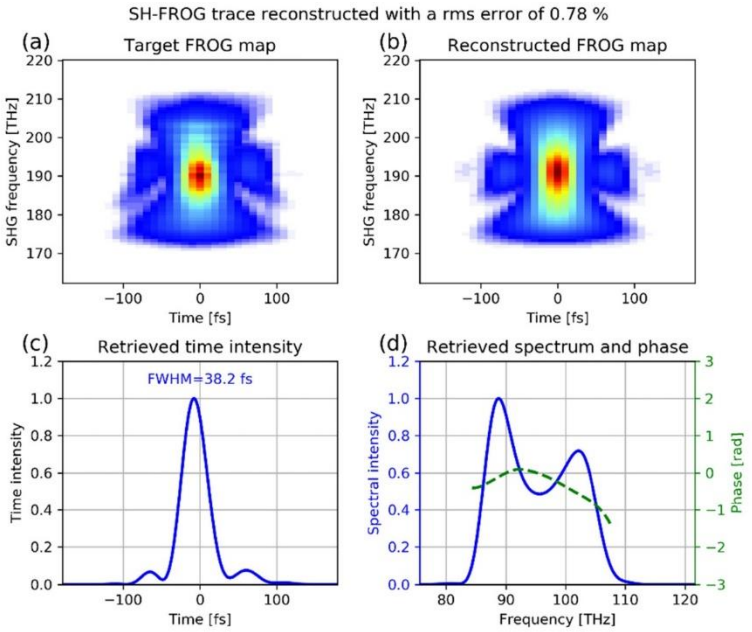

Figure 2.9: a.) Experimental FROG trace. b.) Retrieved FROG trace. c.) Reconstructed time-dependent intensity. d.) Reconstructed spectrum and spectral phase. [21]

The measurement of the Strehl ratio performed by the authors of the above-mentioned articles with a Shack-Hartman wavefront sensor (*Phasics – SID4*) led to a calculated value of *0.87* [21]. The related M^2 value deduced from the wavefront measurements was *~1.4* [21]. This means that the focused intensity is 87% percent of the ideal case, when the wavefront aberrations can be neglected. The measured pulse is focused with a microlens array on a charge-coupled device (CCD) camera. In the ideal case, the initial wavefront is flat, whereby the focal spots of the microlens array are located along a square grid on the CCD. In most cases, the initial wavefront is aberrated, whereby the focal spots are shifted from the ideal square grid. From the magnitude and the direction of these shifts one can retrieve the initial wavefront.

The authors of the above-mentioned articles built a homemade f-2f interferometer, where the collimated beam with *6 µJ* pulse energy propagates through a thin silver gallium sulfide ($AgGaS_2$ or AGS) nonlinear crystal to generate a SH beam, which interferes with the supercontinuum produced in a thin YAG crystal. A *45°* polarizer couples the polarizations of the 2f and the f beams. The spectral beating at *~1.55 µm* between the supercontinuum and the SH is recorded by a fast fringe detector for *8 h* at *10 kHz* repetition rate, which means that a single interferogram is acquired from every ten laser pulses. A digital output is used to feed back the CEP offset to the AOPDF at *10 kHz* and correct for CEP fluctuations. *Figure 2.10* demonstrates the CEP stability measured for *8 h*. The CEP noise is *65 mrad* RMS over the entire measurement time [21].

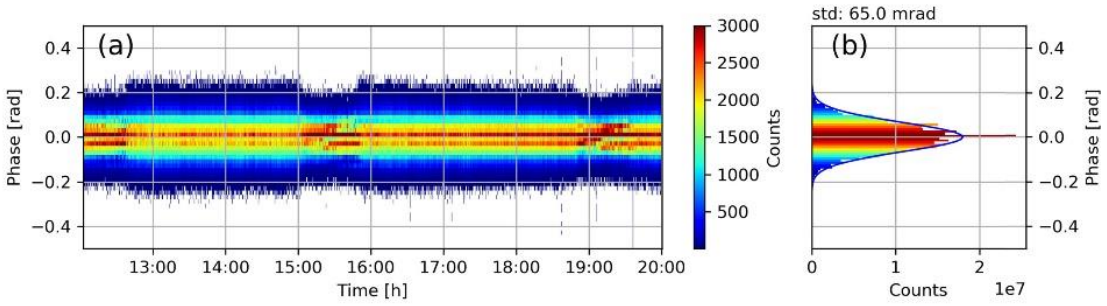

Figure 2.10: Measured CEP noise over 8 h. a.) Temporal evolution of CEP fluctuations: each column is a histogram of measured CEP offsets for 20,000 shots, b.) histogram of the total distribution of measured CEP offsets. [21]

2.4. THz pulse generation

The spectral region of THz radiation (1 mm–10 μm) falls between the microwave and the IR domains, and this region is often referred to as the "THz gap". The name originates from the fact that it was difficult in the past to generate this radiation. On the one hand, this wavelength range was too short for the common electronic methods. On the other hand, it was too long for the common photonic methods. Basically, THz radiation, which was the gap between the electronic and photonic waves for a long time, is an important source in imaging and spectroscopy due to its non-ionizing nature [48-49]. In the following chapters, several common THz pulse generation methods will be reviewed to provide a conceptual basis for the research results presented in subsequent chapters.

2.4.1. Two-color ionization of gases

THz pulse generation from two-color pulse ionized plasma is currently in the focus of research because of its simplicity and potential use as renewable, secondary sources for THz spectroscopy [48-49]. In this method, the source of radiation is the TEC inside the laser induced plasma [43-44]. The most important step in this process is the formation of an asymmetric electric field, which accelerates free electrons in one direction more efficiently than in the other direction, resulting in a non-vanishing TEC build-up inside the plasma [43-44]. The two simplest options to achieve an asymmetrical driving force in electrons in the plasma are few-cycle or two-color pulses. Although the generation of few-cycle pulses is challenging, there are continuous developments in this direction [31-36]. In my view, this method will become even more important as laser technology develops towards the regime of few-cycle pulses. THz pulses based on the two-color pulse method have been successfully demonstrated [45]. In this scheme, the two-color pulses are created through the combination of the fundamental beam and its SH to engineer an asymmetric electric field for THz pulse generation. The combined electric fields produce tunnel ionization of the atoms or molecules, whereupon the free electrons accelerate in the asymmetric electric field. It has been found that in case of linearly polarized pulses this process is most effective when both pulses are polarized parallelly.

There are two main, but conceptually different explanations of the physical processes for THz pulse generation from gases: the FWM-OR [45] and the TEC model [43-44]. The former one describes the physical phenomena as the THz pulse is generated in a third-order nonlinear process, where χ_3 originates from the plasma [45]. In this model, two fundamental photons (ω_F) and one SH photon ($\omega_{SH} = 2\times\omega_F$) generate the THz photon ($\omega_{THz} = \omega_{SH} - \omega_F - \omega_F$) by FWM-OR. The latter describes the physical process as the pulses build up a TEC in the plasma, which radiates an electromagnetic wave with an angular frequency inversely proportional to the pulse duration [43-44]. Although both descriptions explain most of the experimental results, it has been observed that TEC works better in the low frequency domain (<10 THz) [61-62], therefore the numerical simulations presented in this thesis used this model [43-44].

Briefly, the numerical model starts with the SHG with the slowly varying amplitude approximation [50]. First, the nonlinear crystal is split into several thin slices, where the nonlinear wave equations (*Equation 2.21* and *2.22*) are solved:

$$\frac{dA_1}{dz} = \frac{2id_{eff}\omega_1^2}{k_1c^2}A_2A_1^*e^{-i\Delta kz} \text{ and} \tag{2.21}$$

$$\frac{dA_2}{dz} = \frac{2id_{eff}\omega_2^2}{k_2c^2}A_1^2e^{i\Delta kz}\,, \tag{2.22}$$

where A_1 (A_2) is the amplitude, ω_1 (ω_2) is the angular frequency, and k_1 (k_2) is the wavenumber of the fundamental (SH) wave. In this numerical simulation, Z-cut gallium selenide (GaSe) was chosen as the nonlinear crystal for SHG because of the investigated spectral domain. The refractive index [63] and the effective nonlinear coefficient (d_{22}=*86 pm/V*) [64] of the nonlinear crystal is well known from literature. The value of d_{eff} is calculated with $d_{22}\times cos(\theta)$ in case of the GaSe, where θ is the phase matching angle. The value of θ is calculated with $2\times k_1=k_2(\theta)$ for Type-I (ooe) phase matching. In this case, the fundamental wave is ordinary (o) polarized, while the SH wave is extraordinary (eo) polarized. The transparency window of the nonlinear crystal is very broad (*0.8 µm–36.1 µm*) [63], although Type-I phase matching for SHG is limited to a narrower bandwidth (*2.15 µm–15.15 µm*). The reasons behind this will be explained later. After solving the nonlinear wave equations (*Equation 2.21* and *2.22*) numerically for a short distance (Δz), the linear wave equations (*Equation 2.23* and *2.24*) were solved as follows:

$$A_1(z+\Delta z) = A_1(z)e^{-i2\pi n_1\Delta z/\lambda_1} \text{ and} \tag{2.23}$$

$$A_2(z+\Delta z) = A_2(z)e^{-i2\pi n_2\Delta z/\lambda_2}\,, \tag{2.24}$$

where λ_1 (λ_2) is the carrier wavelength of the fundamental (SH) waves and n_1 (n_2) is the refractive index of the nonlinear crystal at λ_1(λ_2). The complex amplitudes were calculated at each wavelength while taking the material dispersion into account. The nonlinear (*Equation 2.21* and *2.22*) and linear (*Equation 2.23* and *2.24*) wave equations were solved sequentially for each thin slice. This numerical model was used for the calculations of the energies, the spectral intensity and the pulse phase. During SHG, the reflection losses on both surfaces, the temporal walk-off and the dispersion are also considered. An illustrative result of the SHG is shown in *Figure 2.11*. The fundamental wave is represented in red color, while the SH wave is represented in blue color. The carrier wavelength of the fundamental pulse is *3200 nm* and the spectral bandwidth supports

42.7 fs (4 optical cycle) pulse duration in FTL. The peak power is *2.5 GW*, while the intensity on the GaSe crystal is 1.5×10^{15} *W/m*^{2}, which is equal to *0.75 GV/m*. The temporal and spectral profiles are also chosen to be Gaussian. The thickness of the nonlinear crystal is chosen as *30 μm* during this illustrative numerical simulation.

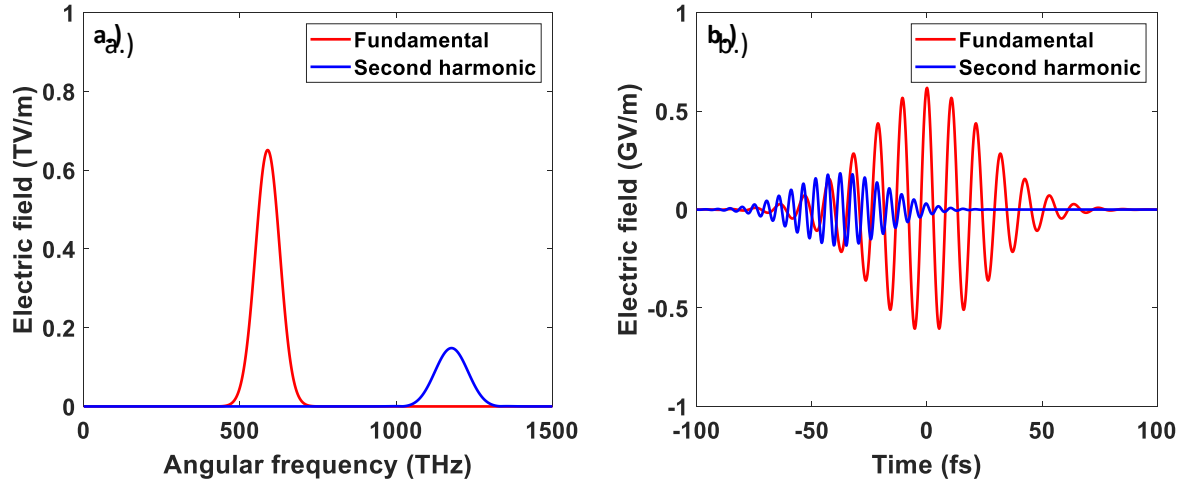

Figure 2.11: An illustrative result of the SHG a.) in the spectral and b.) in the temporal domain. The fundamental beam is represented in red color, while the SH beam is represented in blue. The carrier wavelength of the fundamental pulse is 3200 nm and the spectral bandwidth supports 42.7 fs (4 optical cycle) pulse duration in FTL. The peak power is 2.5 GW, while the intensity on the GaSe is 1.5×10^{15} W/m^2, which is equal with 0.75 GV/m. The temporal and spectral profiles are also chosen to be Gaussian. The thickness of the nonlinear crystal is chosen as 30 μm during this illustrative numerical simulation.

In the next step, I calculated the focusing of the beams based on the ABCD law [65]. In this numerical simulation, to avoid any unwanted absorption during propagation, the full beam path was considered to be in dry nitrogen, while dispersion was assumed to follow the generalized Sellmeier equation [66].

In the focus, the tunnel ionization rate was calculated based on the Ammosov-Delone-Krainov (ADK) formula [67-68], which can be written as:

$$W = 1.61\omega_{au}\frac{Z^2}{n_{eff}}\left(10.87\frac{Z^2}{n_{eff}^4}\frac{E_{au}}{E}\right)^{2n_{eff}^{-1.5}} e^{\left(-\frac{2}{3}\frac{Z^3}{n_{eff}^3}\frac{E_{au}}{E}\right)}, \tag{2.25}$$

where ω_{au} (4.1×10^{16} *Hz*) and E_{au} (5.14×10^{12} *V/m*) are the atomic units of the angular frequency and the electric field, respectively. E is the combined electric field of the fundamental and its corresponding SH pulses, Z is the residual charge of the parent ion seen by the free electron. The effective quantum number, n_{eff} is defined by the following:

$$n_{eff} = Z\Big/\sqrt{I_N/I_H}\,, \tag{2.26}$$

where I_H and I_N are the ionization potentials of hydrogen (*13.6 eV*) and nitrogen (15.58 eV) [68], respectively. The electron density (n_e) was calculated using *Equation 2.25* and the rate equations, which can be written as:

$$n_e = N_1, \tag{2.27}$$

$$\frac{dN_0}{dt} = -W_1 N_0, \tag{2.28}$$

$$\frac{dN_1}{dt} = W_1 N_0 - W_2 N_1 \text{ and} \tag{2.29}$$

$$\frac{dN_2}{dt} = W_2 N_1 , \tag{2.30}$$

where N_0, N_1 and N_2 are the density of the unionized, singly, and doubly ionized nitrogen, respectively. An illustrative result of tunnel ionization is shown in *Figure 2.12*. The ionization rate is represented in red color and the electron density is represented in black color. The percentage refers to the amount of ionized nitrogen compared to the amount of the initial nitrogen. The initial density of nitrogen is 2.5×10^{25} m^{-3}. The electric field of the fundamental and its corresponding SH are *30.9 GV/m* and *9.2 GV/m*, respectively. The maximum of the first and second ionization rates are 8.5×10^{11} s^{-1} and 2.3×10^{7} s^{-1}, respectively. One can see that the second ionization rate is more than four orders of magnitude less than the first ionization rate. Therefore, the second and higher order ionizations rates can be neglected in my doctoral thesis due to the moderate intensity of the applied electric fields.

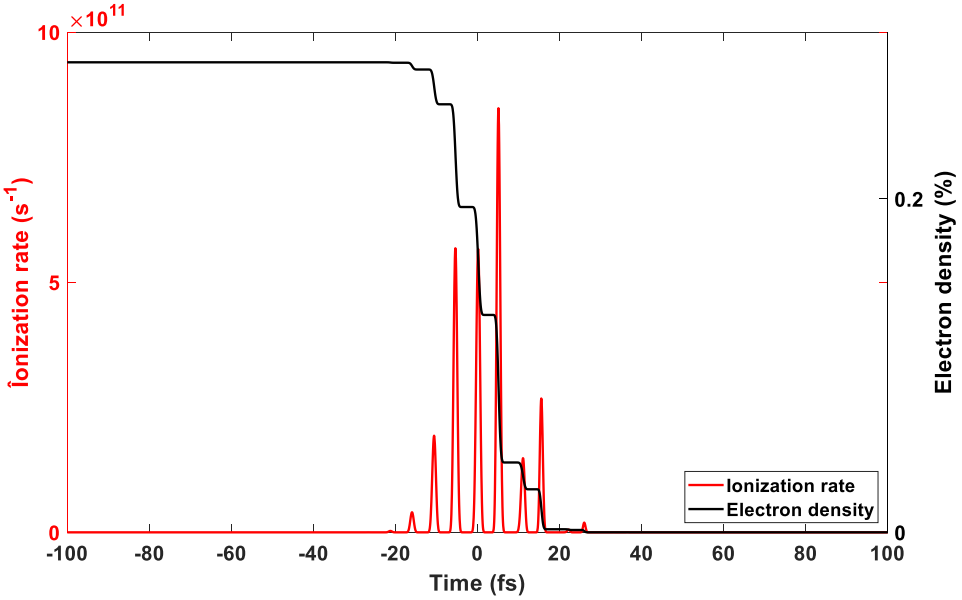

Figure 2.12: An illustrative result of tunnel ionization. The ionization rate represented in red color and the electron density represented in black color. The percentage value shows the amount of ionized nitrogen compared to the initial nitrogen. The initial density of nitrogen is 2.5×10^{25} m^{-3}. The electric field of the fundamental and its corresponding SH are 30.9 GV/m and 9.2 GV/m, respectively.

Once the electrons are free due to tunnel ionization at $t=t'$, they are accelerated by the asymmetric electric field. The time dependent velocity of the free electrons is defined by the following:

$$v_e(t,t') = -\frac{e}{m_e}\int_{t'}^{t} E(t)dt\,, \tag{2.31}$$

where e and m_e are the charge ($1.60\times10^{-19}\ C$) and the mass ($9.11\times10^{-31}\ kg$) of the electrons, respectively. The free electrons not only oscillate in the asymmetric electric field, but also drift in a transverse direction. After both the density (n_e) and velocity (v_e) of the free electrons are known, one can calculate the TEC as follows:

$$J_e(t) = -\int e\,v(t,t')dn_e(t')\,. \tag{2.32}$$

An illustrative result of the TEC is shown in *Figure 2.13.* The electron's velocity is represented in red color and the TEC is represented in black color. The electric field of the fundamental and its corresponding SH are the same as before.

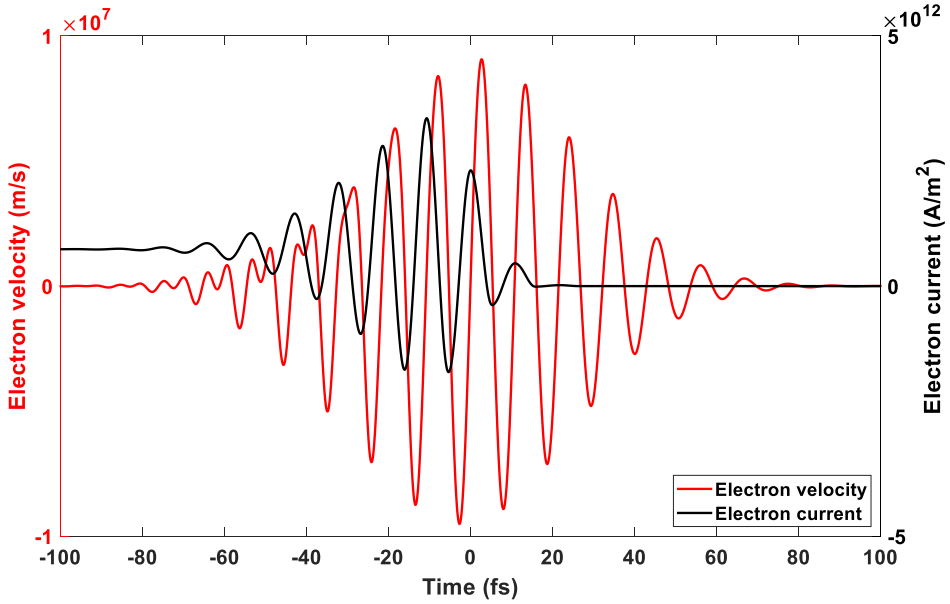

Figure 2.13: An illustrative result of the transverse electron current. The electron's velocity is represented in red color and the TEC is represented in black color. The electric field of the fundamental and its corresponding SH are 30.9 GV/m and 9.2 GV/m, respectively.

The electromagnetic field emitted by the TEC is proportional with its first-time derivative (dJ_e/dt); an illustrative spectrum is shown in *Figure 2.14.a*. The corresponding spectral domains for the THz, the fundamental and the SH are highlighted in grey, red and blue colors, respectively. As one can expect, THz radiation is in the low angular frequency part of the spectrum. An illustrative THz pulse is shown in *Figure 2.14.b*, the electric field is represented in grey, while its envelope in black.

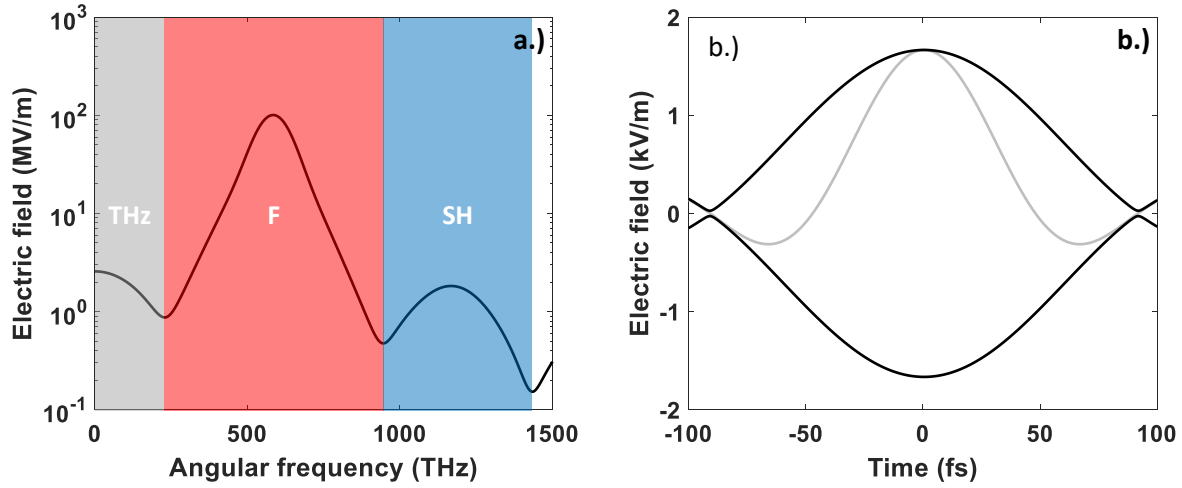

Figure 2.14: a.) An illustrative result of the spectrum is emitted by the transverse electron current. The corresponding spectral domains for the THz, the fundamental (F) and the second harmonic (SH) are highlighted in grey, red and blue colors, respectively. b.) An illustrative result of the THz radiation in temporal domain. The electric field represented in grey color, while its envelope in black color. The electric field of the fundamental and its SH are 30.9 GV/m and 9.2 GV/m, respectively.

The asymmetry of the electric field is crucial for the TEC's development. In the case of the two-color pulses, the asymmetry is associated with the relative phase (RP) between the two pulses. When it is $\pm\pi/2$ *rad*, the acceleration of free electrons becomes the most asymmetric, and a significant TEC builds up inside the plasma [43-44]. An application difficulty is to achieve an appropriate control over the RP, and thanks to this control over the intensity of THz pulses. There are several solutions to achieve sufficient control over the RP. One way is to use a pair of DcMs to separate and recombine the two-color pulses with a sufficient time delay introduced between them with different OPDs. Another way is to simultaneously propagate the two-color pulses on a common path through the same material, which has different phase and group velocities at the two wavelengths, therefore it develops a RP shift during propagation [30, 69].

In recent studies, several groups have demonstrated that the efficiency of THz pulse generation increases with the carrier wavelength [23-30]; some of the different scaling laws are presented in *Table 2.2*. As mentioned earlier, the main reason is the ponderomotive potential, which scales with the square of the carrier wavelength. Another reason is the smaller group and phase velocity difference between the two-color pulses in the MIR spectral domain [24, 26-27, 30]. This provides an improved temporal overlap between the pulses; however, the small phase velocity difference also makes it difficult to achieve appropriate control over the RP. After SHG, phase matching ensures that the RP is *0 rad*. As a friendly reminder, THz pulse generation is the most efficient, when the RP is $\pm\pi/2$ *rad*. This inconvenience can be overcome with different techniques. One obvious solution is the application of DcMs, however the availability of broadband and efficient mirrors in the MIR spectral domain is quite limited. Another popular solution is the co-propagation of the two-color pulses in ambient air. It is a straightforward application when the driving laser is

in the NIR spectral domain, such as a Ti:Sapphire laser (λ=*800 nm*), in which case a few centimeters of co-propagation is sufficient to tune the RP to $\pm\pi/2$ *rad*. However, when the driving source is in the MIR spectral domain, such as a MIR OPCPA (λ=*3-8 μm*), several meters of co-propagation is required to tune the RP to the same extent. An alternative solution is co-propagation in the same material [30, 69]. Different fluorides, especially lithium fluoride (LiF) and calcium fluoride (CaF_2) are excellent choices for this application [30]. First, both materials have negative group velocity dispersion (GVD), which compensates the typical nonlinear crystals' positive GVD, and thanks to this, both materials improve the temporal overlap of the two-color pulses. Second, both materials' refractive indexes change slowly in the MIR spectral domain, therefore the difference between the phase velocities is small. Consequently, a commercially available thickness is necessary to tune the RP to $\pm\pi/2$ *rad*. Finally, it is a highly compact solution compared to the previous two options.

Wavelength (µm)	Scaling law	References
0.8–4.0	$\lambda^{2.6}$	[69]
08–1.8	$\lambda^{4.6}$	[23]
0.8–2.0	$\lambda^{1.7\text{-}2.4}$	[24]
1.0–10.0	$\lambda^{1.8\text{-}2.1}$	[28]
1.2–1.5	$\lambda^{7.8\text{-}9.4}$	[28]
1.3–2.2	$\lambda^{4.6\text{-}8.1}$	[28]
2.4–2.6	$\lambda^{11.4\text{-}14.5}$	[28]
2.2–15.1	$\lambda^{9.0\text{-}9.3}$	[30]
2.2–15.1	$\lambda^{3.4\text{-}3.6}$	[30]
2.2–15.1	$\lambda^{2.1\text{-}2.3}$	[30]

Table 2.2.: The different scaling laws of the efficiency of THz pulse generation.

There are numerous solutions to combine the driving pulses and their SH pulses. One of the simplest optical layouts is the so-called common path scheme as shown in *Figure 2.15*. For the sake of THz pulse generation, the driving pulse is focused into ambient air. A nonlinear crystal is placed before the focus to generate the SH pulses; the type of the nonlinear crystal is chosen based on the carrier wavelength of the pulses. In the case of NIR and MIR driving pulses, the typical choices are beta barium borate (BBO) [23, 45, 70-78] and GaSe [30, 69, 79], respectively. Both nonlinear crystals are used in Type-I phase matching (ooe) for SHG, which means that the fundamental pulses and their SH pulses are o and eo polarized, respectively. This means that the two-color pulses are perpendicularly polarized, which is the exact opposite of the optimum THz pulse generation. There are numerous solutions to overcome this inconvenience and tune the polarization of the two-color pulses. First, there are dual-waveplates, which function as a full wave plate (FWP) at the fundamental wavelength and as a HWP at the SH wavelength. Sadly, there are no available dual wave plates in the MIR spectral domain to the best of my knowledge. Second, it

is possible to detune the Type-I phase matching condition to achieve a partial overlap between the polarization of the two-color pulses [72], which improves the efficiency of THz generation, but at the same time it deteriorates that of SH generation. Since both processes are determinative, there is always an optimal condition, where THz pulse generation is the most intense. In this approach, the minor part of the driving pulse is o polarized, while the major part is eo polarized. The former generates SH pulses in the nonlinear crystal, while the latter, which is parallelly polarized with the SH pulses, generates THz pulses in the focus with the help of the SH pulses.

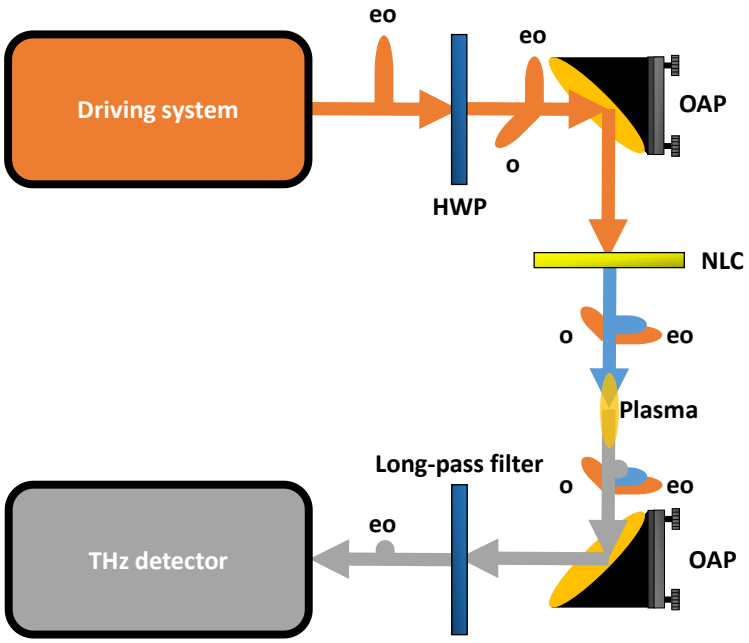

Figure 2.15: The schematic optical layout of the common-path scheme for THz pulse generation. The orange indicates the driving beam, the blue indicates its SH, and the grey indicates the THz pulses. HWP – Half-Wave Plate, NLC – nonlinear crystal, OAP – Off-axis parabolic Mirror, o – ordinary polarization, eo – extraordinary polarization.

2.4.2.Alternative methods for THz generation

In addition to the above-described method, there are several other ways to generate pulsed or continuous wave (CW) THz radiation, but they all utilize nonrenewable medium. The most common methods will be briefly discussed in this chapter. More detailed descriptions can be found in the related literature [80].

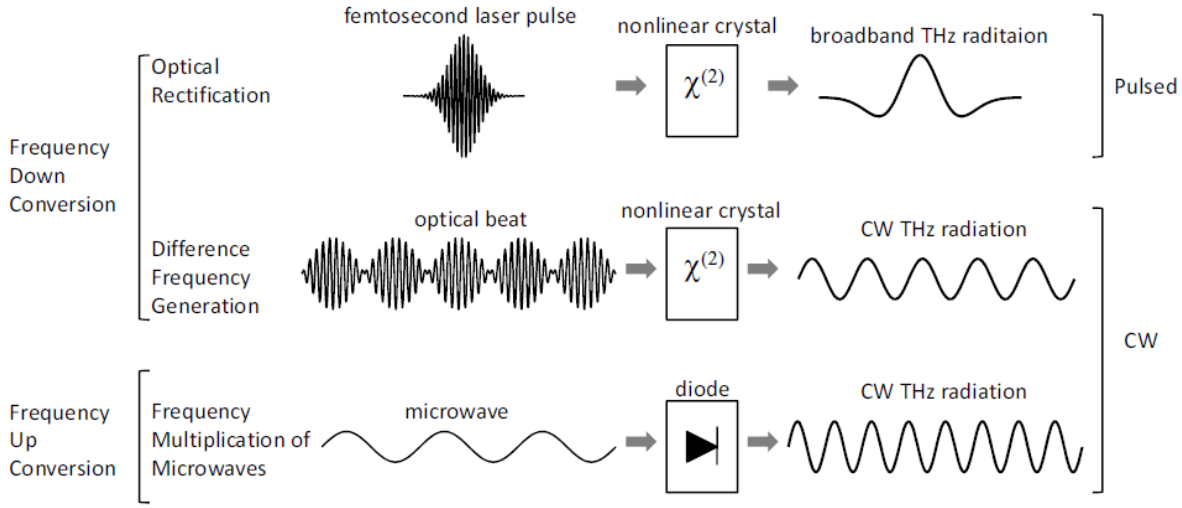

Figure 2.16: Pulsed and CW THz source generation in nonlinear media. (Fig. 1.2 from reference 80.)

One possible way to generate pulsed or CW THz radiation is frequency down-conversion in nonlinear crystals. These sources are based on OR and/or DFG, which are second order nonlinear processes (see *Chapter 2.2.1*). Few-cycle pulses with a broadband spectrum generate broadband THz pulses, the electric field of which has the shape of the envelope of the initial pulse; this process is based on OR [80]. Similarly, CW sources generate CW THz radiation, the frequency of which is equal with the beating frequency between the initial sources; this process is based on DFG [80]. The schematic figure of pulsed and CW THz source generation in nonlinear media is shown in *Figure 2.16*. Another possible way to generate CW THz radiation is frequency up-conversion in nonlinear diodes. These sources are based on HHG, which is a highly nonlinear process. The nonlinear didoes convert the incoming microwaves into their harmonic waves [80]. The schematics of this method are also shown in *Figure 2.16*.

Time-varying currents and accelerating charged particles radiate electromagnetic waves, which can be in the THz spectral domain with properly selected parameters. Photoconductive antennas excited with few-cycle pulses or CW sources are popular choices when it comes to pulsed or CW THz radiation generation. Photoconductive antennas consist of two electrodes made from metal, which are deposited on a substrate made from a semiconducting material. The photocarriers are generated when a few-cycle pulse or CW source illuminates the gap between the metal electrodes. The metal electrodes are connected to a static current, which accelerate the photocarriers. The photocurrent is time-varying, and will look like the envelope of the few-cycle pulse or the beating between the CW sources. Thanks to this, few-cycle pulses with a broadband spectrum generate broadband THz pulses [80]. This technique is known as photo mixing. The schematics of pulsed and CW THz source generation with photoconductive antenna are shown in *Figure 2.17*.

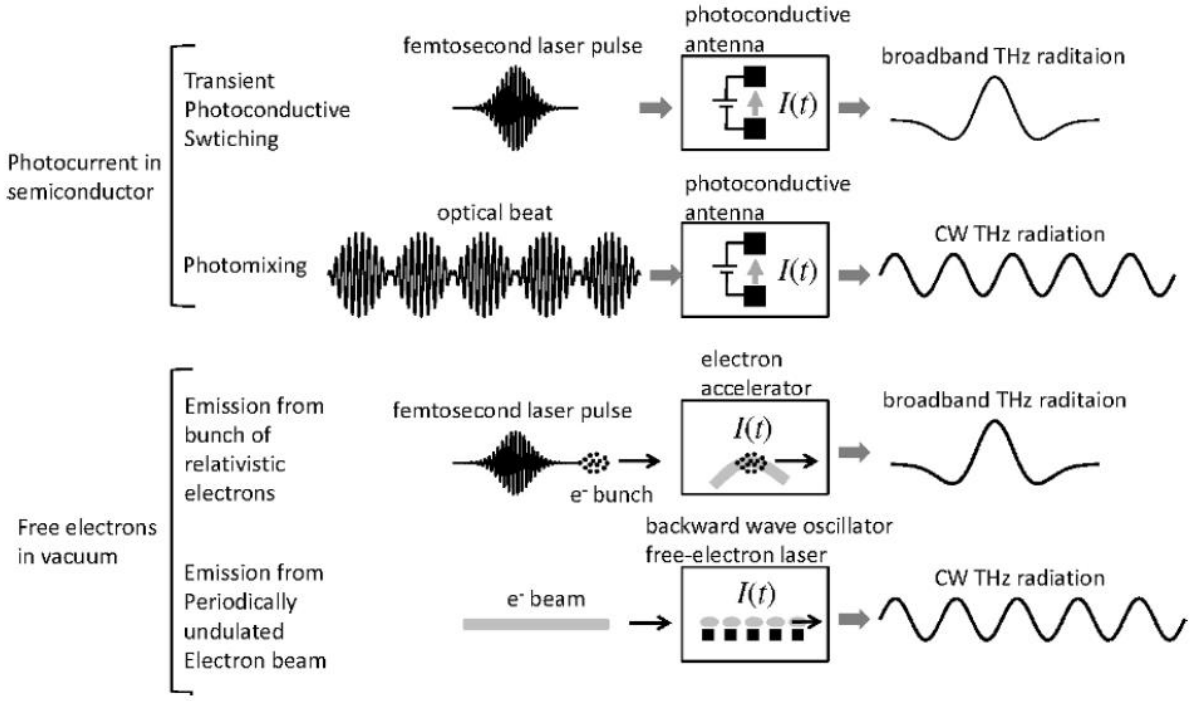

Figure 2.17: Pulsed and CW THz source generation from accelerating electrons. (Fig. 1.3 from reference 80.)

Electron accelerators (free electron lasers and synchrotron sources) represent an additional THz radiation source. They produce relativistic electrons, which can be used to generate extremely bright THz radiation. A few-cycle pulse forces an electron source to generate ultrashort pulses made from electrons. Then, the electron pulse is accelerated to relativistic speed. After this, the relativistic electrons are forced to deaccelerate or change the direction of acceleration. The change in the acceleration of the charged particles generate THz radiation [80]. The schematics of THz source generation with electron accelerators are shown in *Figure 2.17*.

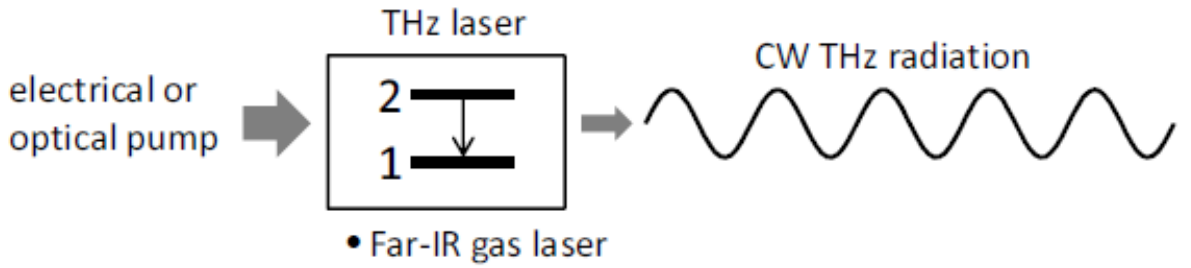

Figure 2.18: Laser based THz source. (Fig. 1.4 from reference 80.)

Free-electron lasers (FELs) are large facility-based, while backward wave oscillators (BWOs) are laboratory-size THz sources. Despite the size difference, the process of THz radiation generation is very similar. In both sources, free electrons undulate periodically, but while BWOs

use a metal grating for undulation, FELs employ a magnet array [80] to achieve the same. The schematics of THz source generation with FELs and BWOs are shown in *Figure 2.17*.

Other THz laser sources exploit population inversion between two energy levels of the system (see *Figure 2.18*). Gas laser sources operating in the FIR spectral regime use the energy levels of molecular rotations [80]. The transition wavelength of these sources falls into the THz spectral domain.

2.5. Spectrally resolved interferometry

The are several measurement methods developed for the spectral phase characterization of optical elements. SRI is one of the most widely used and reliable techniques [81-82]. It is a simple, linear, one-dimensional, and high precision measurement method. In most cases, it utilizes a two-arm interferometer, which can be a Mach-Zehnder (see *Figure 2.19.a*) or Michelson (see *Figure 2.19.b*) type arrangement, illuminated by a broadband light source and detected by a high spectral resolution spectrometer. With the appearance of spectrometers providing high spectral resolution, it became clear that the most accurate evaluation methods are the ones based on the FT [83-86].

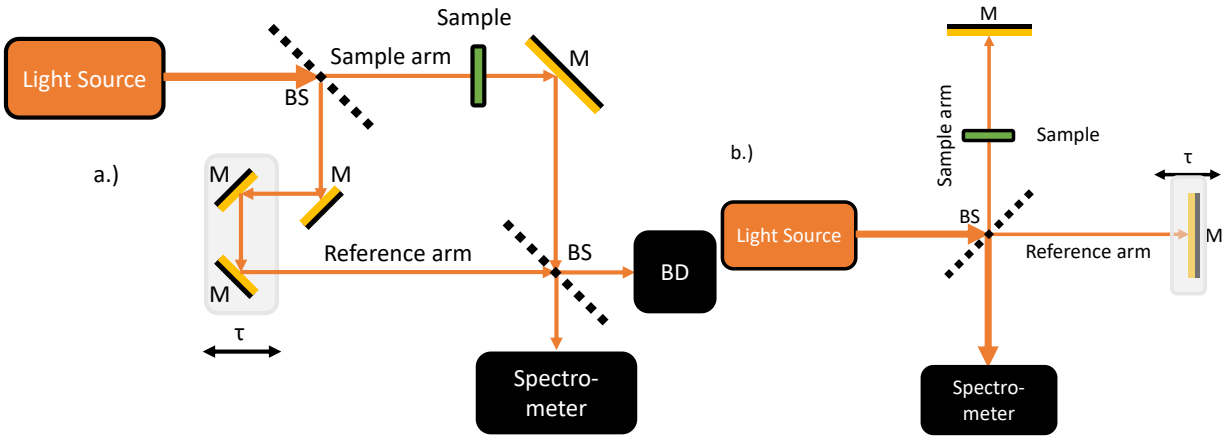

Figure 2.19: Schematic SRI setup based on a.) the Mach-Zehnder and b.) the Michelson arrangement. M – mirror, BS – beam splitter, BD – beam dump.

Both types of interferometers have two arms, a sample and a reference. The length of the former one is immutable, and the sample is inserted in it, while the length of the latter one is adjustable. There is spectral interference between the two arms, which depends on the time delay (τ) between the two arms, and is recorded by the spectrometer at the output of the interferometer. The spectrally resolved interference can be written as follows:

$$I(\omega) = I_S(\omega) + I_R(\omega) + 2\sqrt{I_S(\omega)I_R(\omega)}\cos\big(\varphi(\omega)\big)\,, \qquad (2.33)$$

where $I_S(\omega)$ and $I_R(\omega)$ are the measured spectral intensity in the sample and reference arms, respectively. The symbol $\varphi(\omega)$ is the spectral phase difference between the two arms, and can be written as follows:

$$\varphi(\omega) = \varphi_S(\omega) + {}^{\omega}/_{c}\,(l_S - l_R) = \varphi_S(\omega) + \omega\tau\,, \tag{2.34}$$

where $\varphi_S(\omega)$ is the spectral phase of the sample, and l_S and l_R are the lengths of the sample and reference arms, respectively. The measured spectral phase can be expressed in a Taylor series around the central frequency (ω_0) as follows:

$$\varphi(\omega) \approx \varphi(\omega_0) + \sum_{n=1}^{N} \frac{1}{n!} \frac{d^n\varphi(\omega)}{d\omega_0} \times (\omega - \omega_0)^n\,. \tag{2.35}$$

The relation between the spectral phase of the measurement and the sample, and their corresponding derivatives are the following:

$$\varphi(\omega_0) = \varphi_S(\omega_0) + \omega_0\tau\,, \tag{2.36.a}$$

$$GD(\omega_0) = GD_S(\omega_0) + \tau\,, \tag{2.36.b}$$

$$GDD(\omega_0) = GDD_S(\omega_0)\,, \tag{2.36.c}$$

$$TOD(\omega_0) = TOD_S(\omega_0)\,, \tag{2.36.d}$$

$$FOD(\omega_0) = FOD_S(\omega_0)\,, \tag{2.36.e}$$

where GD, GDD, TOD and FOD are the abbreviations of group delay, group delay dispersion, third and fourth order dispersion, respectively. As one can see, there is a difference between the sample's and the measured spectral phase (*Equation 2.36.a*) and there is a difference in GD too (*Equation 2.36.b*). However, the GDD of the measurement and the sample (*Equation 2.36.c*), the TOD (*Equation 2.36.d*), the FOD (*Equation 2.36.e*) and other higher order derivatives are equal.

An important question is the physical meaning of the different derivatives of the spectral phase, which have a significant effect on the temporal shape of the pulses (*Figure 2.20*). GD shifts the pulses in time, while the direction of the shift depends on the sign of GD (*Figure 2.20.a*). GDD stretches the pulses in time (*Figure 2.20.b*). If the sign is positive, one can talk about positively chirped pulses, in which case the "red" part of the spectrum propagates further than the "blue" part. In the other case, when the sign is negative, one can talk about negatively chirped pulses, when the "blue" part of the spectrum propagates further than the "red" part. However, the temporal shape in the case of positive or negative sign GDDs is the same as one can see in *Figure 2.20.b*. TOD develops side peaks in the temporal domain, and the orientation of these peaks depend on the sign of the TOD (*Figure 2.20.c*). FOD also stretches the pulse in time, just like the GDD, but it develops shoulders (*Figure 2.20.d*). However, the temporal shape in the case of positive or negative FOD are the same as one can see in *Figure 2.20.d*. In general, these effects shape the temporal profile of the pulses together. In most cases it is sufficient to compensate the GDD to achieve short pulses. However, if one wants to achieve a pulse duration of a few optical cycles, the TOD and sometimes the FOD must also be compensated.

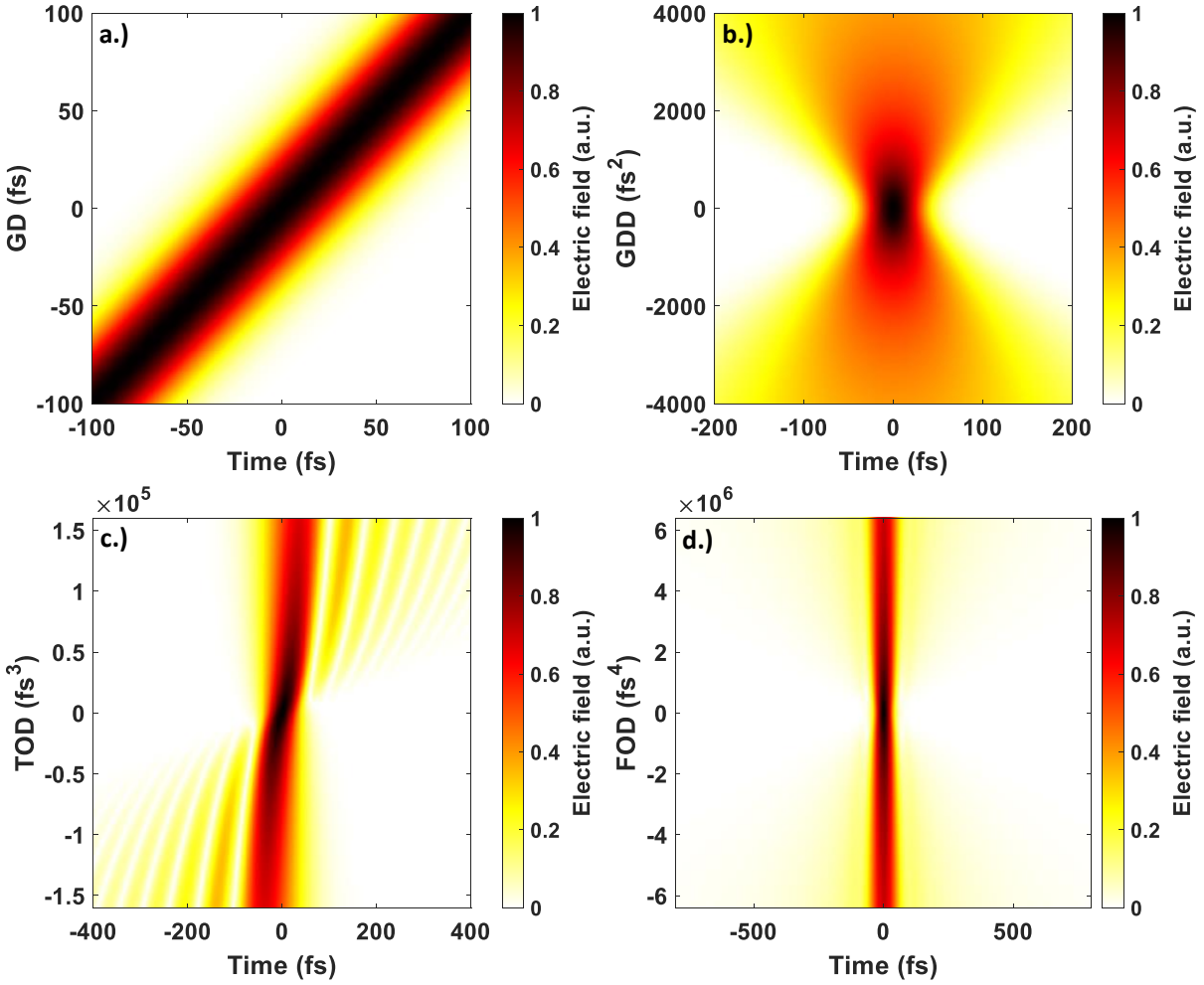

Figure 2.20: The effect of a.) GD, b.) GDD, c.) TOD and d.) FOD on the temporal profile of the pulse. The carrier wavelength is 3200 nm and the FTL pulse duration is 42.7 fs (4 optical cycles).

The recorded spectrally resolved interference can be evaluated with several methods some of which require the production of normalized interference, which is the following:

$$\cos\big(\varphi(\omega)\big) = \big(I_S(\omega) + I_R(\omega) + I(\omega)\big) \Big/ 2\sqrt{I_S(\omega) I_R(\omega)}. \tag{2.37}$$

In this case, the amplitude of the normalized interference – which is needed for the cosine function fit method – is constant. There are two more evaluation methods which use the extreme values (minimums or maximums) of the normalized interference. Extreme values appear, when the first derivative of *Equation 2.37* is equal to zero:

$$\frac{d\cos\big(\varphi(\omega)\big)}{d\omega} = -\sin\big(\varphi(\omega)\big)\frac{d\varphi(\omega)}{d\omega} = 0 \tag{2.38}$$

The stationary phase point method [87] is based on the condition of $\frac{d\varphi(\omega)}{d\omega} = 0$, while the minima maxima method [87] is based on the condition of $-\sin(\varphi(\omega)) = 0$. The aforementioned methods are described in detail in the relevant literature [87].

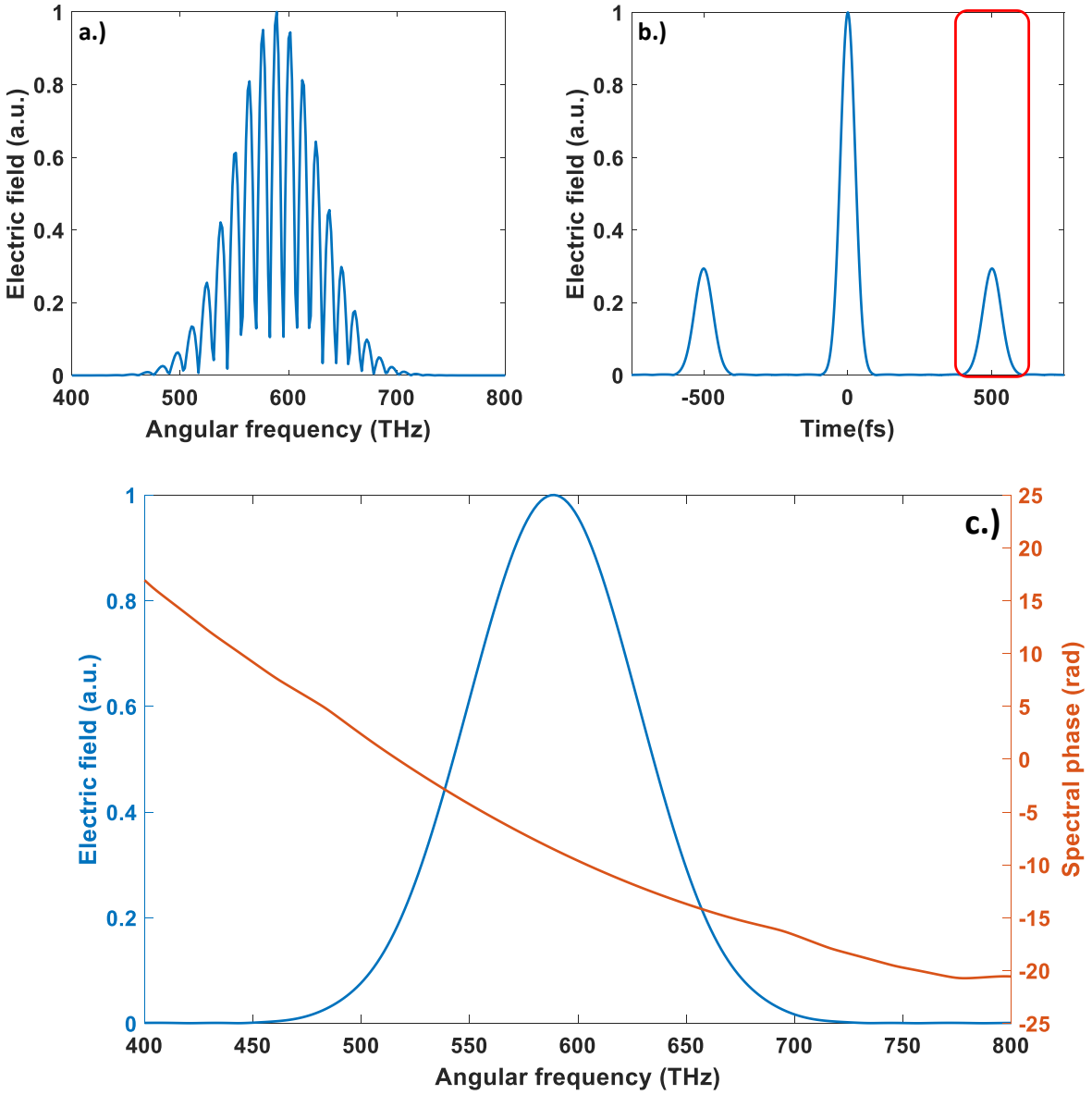

Figure 2.21: a.) The measured interference. b.) The temporal profile after the inverse Fourier transformation. The temporal profile filtered around the +τ (highlighted in red color) c.) The recovered spectral profile and phase after the FT.

The method applied in this thesis is the so-called FT method [83-89]. An illustration of the different steps of the applied method can be seen in *Figure 2.21.* In the first step, we need to take the square of the measured interference (see *Figure 2.21.a*), because in the next step we need to

apply the inverse FT (*Equation 2.21*), which connects the spectral and temporal domains of the electric fields. The inverse FT of the spectral domain is the following:

$$F\{E(\omega)\} = F\{E_S(\omega)\} + F\{E_R(\omega)\} + F\left\{2\sqrt{E_S(\omega)E_R(\omega)}\cos\left(\varphi(\omega)\right)\right\}. \quad (2.39)$$

In the temporal domain we have the following:

$$E(t) = E_S(t) + E_R(t) + E_I(t-\tau) + E_I(t+\tau), \quad (2.40)$$

where $E(t)$, $E_S(t)$ and $E_R(t)$ are the inverse FT of $E(\omega)$, $E_S(\omega)$ and $E_R(\omega)$, respectively. The spectral envelope of the pulses from the sample ($E_S(\omega)$) and reference ($E_R(\omega)$) arms are a slowly varying function of ω, hence $E_S(t)$ and $E_R(t)$ will have around zero time delay as one can see in *Figure 2.21.b*. In contrast with the former, the interference part ($2\sqrt{E_S(\omega)E_R(\omega)}\cos\left(\varphi(\omega)\right)$) is a rapidly varying function of ω, hence $E_I(t-\tau)$ and $E_I(t+\tau)$ will have around $-\tau$ and $+\tau$ time delay as one can see in *Figure 2.21.b*. As a reminder, $\pm\tau$ is the time delay between the two arms of the interferometer. In the following step we need to filter out the peak around $+\tau$. The filtered region is highlighted in red color as one can see in *Figure 2.21.b*. The final step is the FT of temporal domain, where we obtain a complex result. The amplitude is the spectral profile, while the angle is the spectral phase as one can see in *Figure 2.21.c*.

The evaluation of the conventional SRI and the SH-SRI is the same as described earlier. The only difference is that the recovered spectral phase of the SH-SRI is two times the actual spectral phase. This is because in the SH-SRI scheme, the pulses after the interferometer are sent through a nonlinear crystal for SHG. Similarly, the recovered GD, GDD, TOD and FOD are 4, 8, 16 and 32 times the actual values, respectively. The SH-SRI method is discussed in detail in *Chapter 3.1*. This chapter only presents the necessary deviation.

To prove the aforementioned statement, a simple theoretical model is used to describe the process [36]. A one-dimensional pulse with k_F wave number travels in z direction. The complex electric field (E_F) can be described with its real amplitude (A_F) and its complex phase (θ_F). Let us also assume that the pulse is quasi-monochromatic with ω central frequency, so its phase changes almost linearly with time. The deviation from this linear evolution is described with its temporal phase φ. The electric field of such a pulse can be written as:

$$E_F = A_F \times e^{i\theta_F} = A_F \times e^{i\left(k_F z - \omega t + \theta_F(t)\right)}. \quad (2.41)$$

The generated SH electric field is also a wave with a wave number k_{SH} traveling in z direction, and has twice the frequency of the fundamental. It can be written as:

$$E_{SH} = A_{SH} \times e^{i\theta_{SH}} = A_{SH} \times e^{i\left(k_{SH} z - 2\omega t + \theta_{SH}(t)\right)}. \quad (2.42)$$

The two electric fields are coupled by the nonlinear polarization of the material [50]. The coupling strength depends on the effective value of the d matrix (d_{eff}), which is the effective nonlinear coefficient used to describe the conversion efficiency of nonlinear processes. The spatial evolution and the phase of the SH amplitude are described as follows:

$$dA_{SH}/_{dz} \times e^{i\theta_{SH}} = {2id_{eff}(2\omega)^2}/_{c^2 k_{SH}} \times (A_F)^2 \times e^{2i\theta_F}\,. \tag{2.43}$$

For *Equation 2.43* to be fulfilled, both the amplitude and the spectral phase of the left and right sides must be equal. The spectral phase relation between the fundamental and SH pulses is described as:

$$\theta_{SH} = 2\theta_F + {\pi}/{2}\,. \tag{2.44}$$

Furthermore, let us assume that in the SH generation process the phase-mismatch is zero ($\Delta k = k_{SH} - 2k_F = 0$), which is an acceptable approximation for the whole fundamental spectrum in most cases. Here the temporal phase of the SH pulse can be calculated using the following equation:

$$\varphi_{SH}(t) = 2\varphi_F(t) + {\pi}/{2}\,. \tag{2.45}$$

At the output of the interferometer, the two fundamental pulses are separated by a few picoseconds, which is significant compared to their durations. This prevents parametric processes between the two pulses in the nonlinear crystal. Therefore, we can treat the two SH generation processes separately as follows:

$$E_{SRI} = A_{SH} \times e^{i\theta_{SH_1}} + A_{SH} \times e^{i\theta_{SH_2}}\,. \tag{2.46}$$

The intensities of the two pulses can be recorded by a spectrometer. The resulting interference is described as:

$$I_{SRI} \sim E_{SRI} \times {E_{SRI}}^* = 2A_{SH}^2\left(1 + \cos\left(\theta_{SH_2} - \theta_{SH_2}\right)\right)\,. \tag{2.47}$$

Using again the condition that the phase-mismatch is canceled, we get the following equation:

$$I_{SRI} \sim \left(1 + \cos\left(2\varphi_{F_2}(t) - 2\varphi_{F_2}(t)\right)\right), \tag{2.48}$$

which proves that the spectral phase recovered from the interference at the SH wavelength is indeed twice the initial spectral phase difference between the two arms of the interferometer. Upon dividing the spectral phase by two and expanding it around the fundamental central frequency, one can easily extract the spectral phase derivatives at the fundamental frequency too. One can see that based on this description, the presented method works similarly for third and higher order harmonic generation.

"I refuse to answer that question on the grounds that I don't know the answer."

Douglas Adams

3. Scientific results

In this chapter, I briefly summarize the results of my experimental and numerical research that form the backbone of this doctoral dissertation. The results with the SH-SRI technique are introduced in *Chapter 3.1*. The postcompression of the MIR OPCPA system at ELI ALPS Research Institute is presented in *Chapter 3.2*. The numerical simulations of THz pulse generation with few optical cycle MIR pulses are discussed in *Chapters 3.3 to 3.6.* My corresponding thesis points are the following:

T.1: I developed a spectrally resolved interferometer assisted by second harmonic generation. Thanks to this innovation, I was able to overcome the limited spectral resolution of commercially available spectrometers in the mid infrared spectral domain. I achieved this by transferring the spectral phase information in the near infrared spectral domain, where commercial spectrometers with higher spectral resolution are more common. I verified the newly developed second harmonic assisted spectrally resolved interferometer with materials with well-known spectral phase. I also compared it with the conventional spectrally resolved interferometer in terms of root mean square deviation and standard deviation, and it was found to perform better in both terms. Using this technique, I was able to measure the group delay spectrum of the newly manufactured dispersive mirror pair designed for postcompression in the mid infrared spectral domain, and I found good agreement with the designed value. [36]

T.2: I used the dispersive mirror pair characterized in the first thesis point and developed the postcompression stage of the mid infrared laser system at ELI ALPS Research Institute. I tested several available materials for self-phase modulation. Barium fluoride, potassium bromide, and silicon were found to be best in terms of transmission and spectral broadening. I also tested different combinations of these materials, and the barium fluoride and silicon pair was found to have the highest potential peak power. I was able to compress the pulse almost down to the Fourier transform limit with the help a calcium fluoride window and three dispersive mirrors. I managed to shorten the pulse duration, which was originally five optical cycles (*~50 fs)* to less than two optical cycles (*~20 fs*) during postcompression. During my work, another aim was to increase the peak intensity of the system. Here I achieved a *30.3%* increment. [36]

T.3: I investigated the possibility of using the mid infrared system at ELI ALPS Research Institute to generate terahertz pulses in nitrogen plasma with two-color pulses. With numerical simulation I investigated the efficiency improvement in terahertz pulse generation with mid and longwave infrared two-color pulses compared to near infrared two-color pulses with the same input pulse parameters. I investigated the spectral domain from *2.15 μm* to *15.15 μm* and tested different thicknesses of the nonlinear crystal. I found that the scaling law of the terahertz

pulse generation increases with increasing nonlinear crystal thickness. From this I concluded that terahertz pulse generation is very sensitive to second harmonic generation. Furthermore, I investigated the scaling law with different cutoff frequencies and found that it slowly increases with decreasing cutoff frequency. From this I concluded that the lower frequency part of the terahertz spectrum is more sensitive to the driving wavelength. Finally, I found that terahertz radiation generated with mid infrared ($3.3\ \mu m$) and longwave infrared ($7.3\ \mu m$) is by one and two orders of magnitude more intense than the terahertz radiation generated with near infrared ($0.8\ \mu m$) two-color pulses. [30]

T.4: I investigated the relative phase tuning ability of thin dielectric plates with mid infrared, two-color pulses during terahertz pulse generation in nitrogen plasma. My aim was to determine which material is best suited for fine-tuning the relative phase between the two-color pulses, and thus also for optimizing the peak intensity of the terahertz pulse. I investigated terahertz pulse generation with several materials, transparent in the mid infrared spectral domain. I also simulated the terahertz pulse generation with different material thicknesses and angles of incidence. I found that the best candidates are different fluorides, especially lithium and calcium fluoride. These materials have negative group velocity dispersion, and thanks to this they are not just able to control the relative phase between the two-color pulses but also improve the temporal overlap between them, which further increases the efficiency of terahertz pulse generation. [30]

T.5: I investigated terahertz pulse generation in nitrogen plasma as a function of pulse duration and polarization angle. I identified three distinctly different regions, where the optimal pulse parameters for the most efficient terahertz pulse generation are different. The first or conventional region is where the two-color pulse scheme is dominant above *3.2* optical cycles (*34.1 fs* at $3.2\ \mu m$). The second or unconventional region is, where the one-color pulse scheme is dominant below *1.7* optical cycles (*18.1 fs* at $3.2\ \mu m$). The last or semi-conventional/transitional region is, where the two-color pulse scheme is still dominant, but the sign of the relative phase is also determinative. In the conventional region, two-color pulses with opposing relative phases generate terahertz pulses with the same absolute peak power, but this is not true in the transitional region. In addition, I found that the lower boundary of the conventional region increases with increasing central wavelength, while the upper boundary of the unconventional region decreases with increasing central wavelength. [79]

T.6: I investigated the carrier to envelope and the relative phases effect on terahertz pulse generation as a function of pulse duration and polarization angle. As the pulse duration gets shorter, terahertz pulse generations moves away from the conventional to the unconventional scheme. That is why the sensitivity of the terahertz pulse generation to the carrier to envelope phase increases, while sensitivity to the relative phase decreases with decreasing pulse duration. As the pulse duration decreases, the need for the second harmonic pulse also decreases, which also reduces the effect of the relative phase. As the pulse duration increases, the number of individual optical cycles increases, which reduces the difference between them, and consequently diminishes the impact of the carrier to envelope phase. Furthermore, I also investigated the effect of the polarization angle of the fundamental pulse on these sensitivities.

I found that the switching point, the point where the two sensitivities are equal, increases with a decreasing polarization angle. As the polarization angle decreases, the efficiency of second harmonic generation also decreases, which reduces the importance of the relative phase. This, in turn, increases the position of the switching point. [79]

3.1. Second harmonic assisted SRI

In this thesis point I present the second harmonic assisted SRI (SH-SRI) method. The evaluation of the methods is described in detail in *Chapter 2.5*. First the experimental arrangements of the conventional and the SH-SRI are introduced, after which the measurements of the optical windows with both techniques are discussed and compared. Finally, the measurement of the dispersive mirror pair is presented and compared with both techniques.

3.1.1. Experimental setups

The light source for the conventional and the SH-SRI was the MIR OPCPA system at ELI ALPS Research Institute (see the description of the system in *Chapter 2.3*). The schematic layout of the conventional SRI setup is shown in *Figure 3.1.a.* The arrangement is based on the Mach-Zehnder interferometer (MZI), where the input beam is divided into two roughly equal parts by a CaF_2 beam splitter. The sample and reference arms both contain three unprotected flat gold mirrors (GMs). The two beams are combined by the same type of CaF_2 beam splitter as the first one. Note that both the sample and the reference beams underwent one transmission and one reflection on the CaF_2 beam splitters, which nullifies the spectral phase difference between the two arms in an empty interferometer. After combination, the beams were focused on the entrance slit on a MIR spectrometer (Fastlite – Mozza), which had a spectral resolution of $5\ cm^{-1}$ ($\sim 2.5\ nm$). The spectrum recorded by the MIR spectrometer after combination is shown in *Figure 3.1.b*.

The schematic layout of the SH-SRI setup is shown in *Figure 3.2.a*. The interferometer is based on the same MZI as shown in *Figure 3.1.a*. However, this time the output of the MZI went through an SHG stage instead of a MIR spectrometer. The combined beams were focused by a *150 mm* focal length, CaF_2 plan-convex lens with broadband antireflection (BBAR) (*2–5 μm*) coating into a *100 μm* thick, silver gallium sulfide ($AgGaS_2$ or AGS) crystal ($\theta=39°$, $\varphi=45°$) placed at the focus for SHG. Both the fundamental and SH beams collimated by another *150 mm* focal length CaF_2 lens with BBAR (*1.4–1.7 μm*) coating at the SH wavelength. Thereafter, the fundamental and the SH beams were separated by a DcM (transmitting the fundamental and reflecting the SH wavelength). Finally, the SH beams were sent to a *Yokogawa – AQ6375B*-type NIR optical spectrum analyzer (OSA), the spectral resolution of which is *0.05 nm*. The higher spectral resolution (compared to the MIR spectrometer) supported a higher temporal delay between the two arms of the MZI – resulting in a denser fringe pattern in the recorded spectrum – and consequently allowed for more accurate GD spectra retrieval. The recorded spectrum with the NIR OSA is shown in *Figure 3.2.b.*

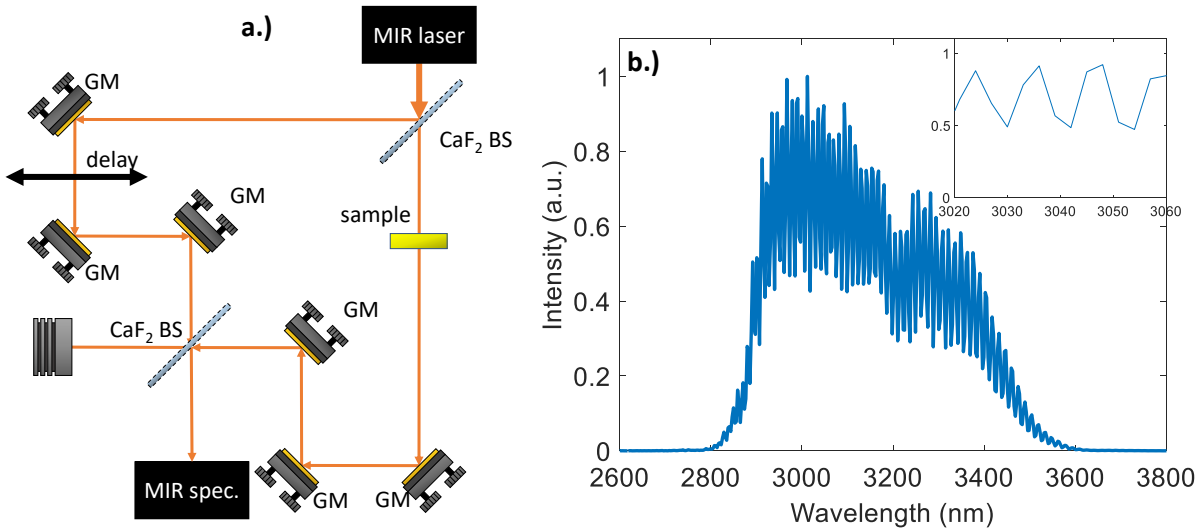

Figure 3.1: a.) Schematic layout of the SRI setup. BS – beam splitter, GM – gold mirror. b.) Interference fringes recorded with the MIR spectrometer at a central wavelength of 3170 nm. The group delay between the arms was 2.7 ps, and a 3 mm thick YAG window was included in the sample arm. The inset shows the recorded interference fringes in a smaller region for better visibility.

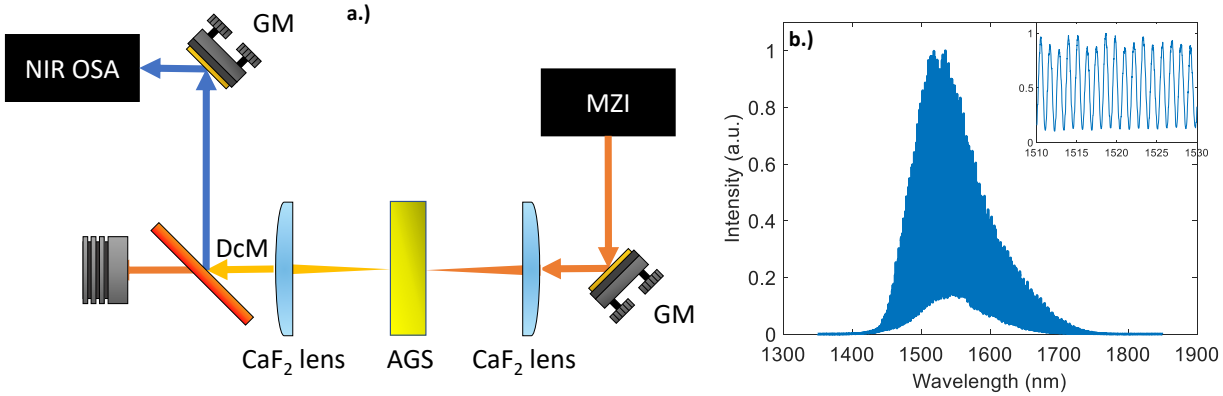

Figure 3.2: a.) Schematic drawing of the SH-SRI setup. DcM – dichroic mirror, GM – gold mirror, MZI – Mach-Zehnder interferometer (the same as in Fig. 3.1.a.), OSA – optical spectrum analyzer. b.) Interference fringes recorded with the NIR OSA at a central wavelength of 1550 nm. The group delay between the arms was 10.1 ps, and a 3 mm thick YAG window was included in the sample arm. The inset shows the recorded interference fringes in a smaller region for better visibility.

3.1.2. Validation of the SH-SRI technique

In this chapter the performance of the conventional and the SH-SRI methods are examined and compared through the characterization of the GD spectrum of well-known optical windows transparent in the MIR spectral domain. The evaluation of the recorded interference is based on the FT method (see *Chapter 2.5*) in both techniques. As the basis of the comparison, I chose the

extracted GD spectrum instead of the spectral phase spectrum, because the measured GD spectrum is unambiguous up to an additive constant offset (see *Equation 2.36.b*). Note that the spectra of higher order derivatives would be free from the above-mentioned constant offset (see *Equation 2.36.c-e*), however, the accuracy of the retrieved spectra would decrease at the same time. The GD spectrum was obtained from the spectral phase spectrum with numerical derivation. One of the examined values was the root mean square deviation (RMSD) between the measured and the calculated GD spectra. The other considered quantity was the standard deviation (STD) of the measured GD spectra. The calculated GD spectra were extracted from the Sellmeier equations of the given materials with numerical derivation.

The inspected spectral region for the conventional SRI ranged from *2900 nm* to *3400 nm*, which corresponded to *1450 nm* and *1700 nm* for the SH-SRI, which was limited by the spectral bandwidth of the SHG, as shown in *Figure 3.2.b*. Although the conventional SRI technique itself is able to inspect a broader (fundamental) spectral region, for the sake of better comparison with SH-SRI, only a narrower spectral region was used for evaluation. For both the conventional and the SH-SRI techniques, 100 spectra were recorded at the same delay and evaluated employing the FT method [83-86]. The measured materials were barium fluoride (BaF_2) [90], CaF_2 [90], thallium bromo iodide (KRS-5) [91], silicon (Si) [92] and yttrium aluminum garnet (YAG) [93].

As an example, the GD spectra of a *3 mm* thick YAG window measured by the conventional and the SH-SRI methods are displayed in *Figures 3.3.a-b*, respectively. The GD spectrum has a negative (positive) slope in the frequency (wavelength) domain, corresponding to the negative GDD of the material at this central wavelength. Similarly, the GD spectra of a *2 mm* thick Si window are presented in *Figures 3.4.a-b* They have a positive (negative) slope in the frequency (wavelength) domain, corresponding to the positive GDD of the material. The RMSD and the STD calculated for all the measured windows are summarized in *Table 3.1*. It can be concluded that the SH-SRI technique yielded better results both in terms of RMSD and STD.

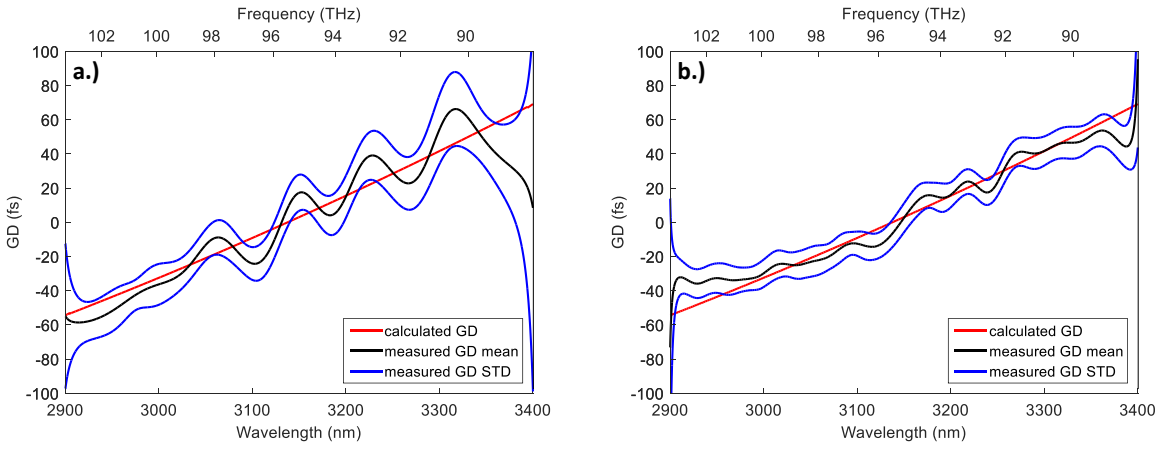

Figure 3.3: The retrieved GD spectrum of the 3 mm thick YAG window with a.) the conventional SRI and b.) the SH-SRI.

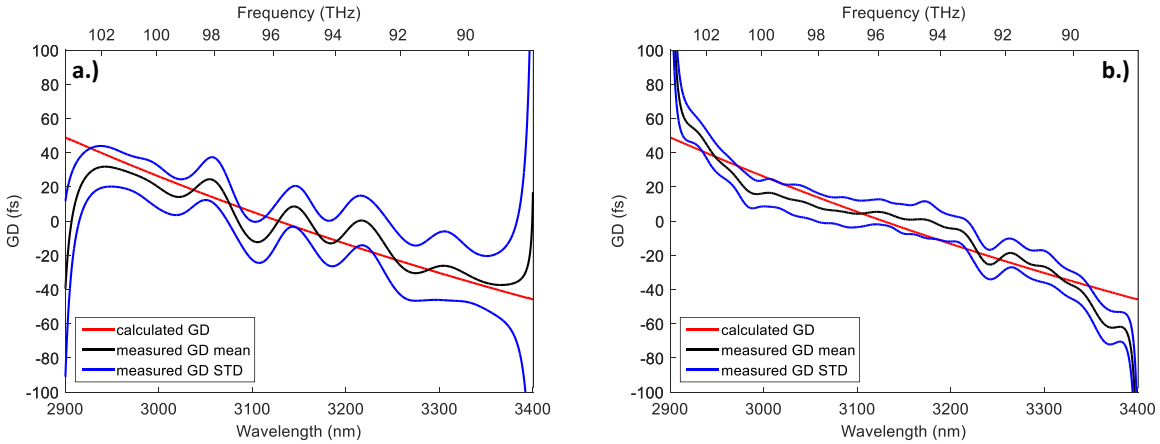

Figure 3.4: The retrieved GD spectrum of the 2 mm thick Si window with a.) the conventional SRI and b.) the SH-SRI.

Windows	GD_{SRI} (fs)		$GD_{SH\text{-}SRI}$ (fs)	
	RMSD	STD	RMSD	STD
BaF_2 (3 mm)	9.46	11.94	3.92	8.18
CaF_2 (3 mm)	7.94	12.50	4.32	7.50
KRS-5 (4 mm)	7.91	10.83	6.08	8.01
Si (2 mm)	8.79	12.79	6.81	8.35
YAG (3 mm)	8.61	11.12	4.57	7.78

Table 3.1: The RMSD and the STD of the GD spectrum in case of conventional and SH-SRI measurements in the spectral range of 3000 nm to 3300 nm.

There were significant differences between the results obtained by the two interferometric techniques. The first difference was in the shape of the GD spectra. It was clearly visible that in case of the conventional SRI method all GD spectra were slightly modulated, while those retrieved by the SH-SRI technique were smoother. Since the spectral resolution of the conventional SRI method was quite low, these fluctuations did not have any physical meaning; they were simply artifacts. The second observable difference, which in fact results from the higher spectral resolution, was the GD peak at *3250 nm*, which was only detectable with the SH-SRI technique. This GD peak was observed above *3.34 ps* time delay between the two arms of the interferometer, where the NIR OSA was still able to resolve the interference pattern, while the MIR spectrometer was not. Since its magnitude was found proportional to the time delay between the two arms of the interferometer, I concluded that it originated from a component of air, and was most probably caused by the absorption of methane (CH_4), as the relevant absorption lines show good agreement with the measurements [94]. This result serves as a nice example of how advantageous the enhanced spectral resolution of the SH-SRI technique was.

3.1.3. Dispersive mirror spectral phase characterization

As I mentioned earlier, reasonable dispersion management was achieved in the MIR spectral domain, simply by using transparent materials having the correct sign and sufficient magnitude of GDD to flatten the spectral phase. However, all transparent materials have positive TOD in the

MIR spectral domain, which limits the compression of pulses above two optical cycles. To overcome this limitation, DMs with positive GDD and negative TOD were designed and manufactured by *OPTOMAN* [95]. A multilayer coating – consisting of 25 alternating layers with a total thickness of 7.4 μm – was deposited on the mirrors by using the ion beam sputtering technology [95]. A special time control strategy was used for the precise termination of layers because in-situ optical monitoring in the MIR spectral domain is very complicated [95]. The key feature of these DMs are its GDD value, which gradually increases with the wavelength [95]. By using a DM pair with mirrors placed at two different angles of incidences (AOIs) (*10°* and *25°*) GDD oscillations can be somewhat minimized to obtain a smoother spectral phase response [95].

The GD of the DMs was measured with both the conventional and the SH-SRI methods, by placing the mirrors in the sample arm of the interferometer. In the MZI, the sample beam undergoes two reflections from two GMs, placed at *25°* and *10°* AOIs, respectively. Both AOIs correspond to the design angles of the DM pair. Exchanging two GMs with the two DMs one after the other and then both simultaneously, allowed me to measure their GD spectra without changing the optical path difference between the two arms of the MZI. The baseline data of the empty interferometer was obtained by using exclusively GMs in the setup. The baseline data acquired above was then subtracted from the resulting GD spectra in all the other measurement series. This way the effect of the CH_4 absorption was also nullified. The measured GD spectra of the DM pair with the conventional and the SH-SRI methods are shown in *Figures 3.5.a-b*, respectively. In the case of the SH-SRI method, there is excellent agreement between the designed and measured GD spectra. The RMSD and the STD of the DM measurements are summarized in *Table 3.2*.

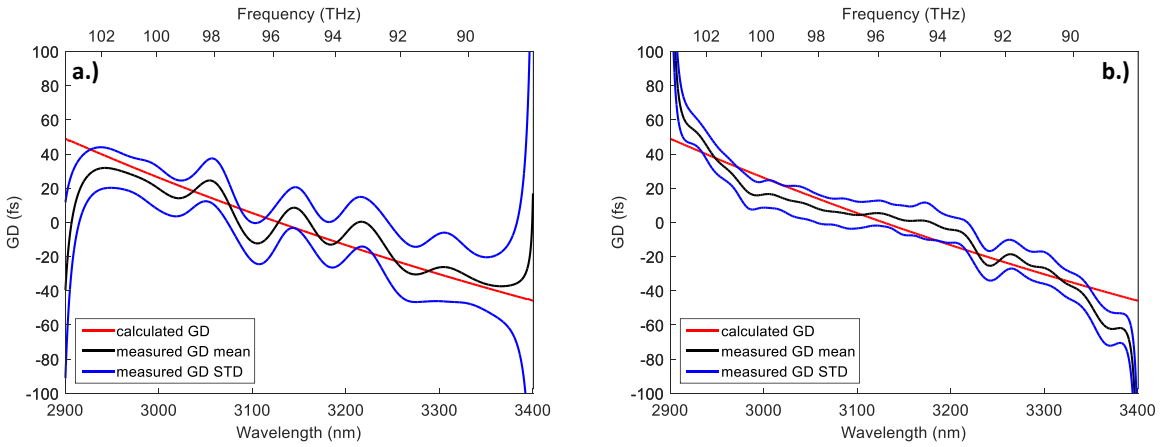

Figure 3.5: The retrieved GD spectrum of the DM pair (10° and 25° AOI) with a.) the conventional SRI and b.) the SH-SRI.

The GD spectra measured with the SH-SRI technique have lower RMSD and STD than the GD spectra measured with the conventional SRI technique. The advantage of the SH-SRI technique is even more obvious when the GD values are small, like in the case of the DMs presented here. According to my measurements, the GDD and the TOD of the DM pair at the central wavelength are *274* fs^2 and *–7204* fs^3, respectively, while the corresponding design values are *270* fs^2 and *–7000* fs^3. One can see that the measured and the design values match very well,

the small differences can be attributed to the uncertainties of the measurements. It can be seen from my results that the DM pair indeed produces positive GDD and negative TOD, so in principle it can be used in combination with material dispersion to compensate the spectral phase of few optical cycle, MIR pulses up to the fourth order of dispersion.

Setup configuration	GD_{SRI} (fs)		$GD_{SH\text{-}SRI}$ (fs)	
	RMSD	STD	RMSD	STD
1 DM (10° AOI)	7.83	11.83	2.10	7.87
1 DM (25° AOI)	4.31	11.44	1.82	10.88
DM pair (10° and 25° AOI)	8.83	10.07	1.64	10.61

Table 3.2: The RMSD and the STD of the GD spectrum in case of the conventional and the SH-SRI measurements in the spectral range of 3000 nm to 3300 nm.

3.1.4.Discussion

In this thesis point the conventional and the SH-SRI techniques are introduced. The key in the latter method is the SHG, which allows for high resolution GD retrieval by transferring spectral phase detection to the NIR spectral domain from the MIR spectral domain, where commercial spectrometers with higher spectral resolution are more common. This scheme notably improves the accuracy of the measurement. The performance of the conventional and the SH-SRI methods were compared by testing well-known optical windows transparent in the MIR spectral domain, and it was found that the latter method gives significantly better results in terms of RMSD and STD. The GD spectrum of the DM pair was also measured using the conventional and the SH-SRI techniques. The results obtained with the latter method showed excellent agreement between the design and the measured values. According to my measurements, GDD and TOD at the central wavelength of the DM pair were $274\ fs^2$ and $-7204\ fs^3$, respectively, while the corresponding design values are $270\ fs^2$ and $-7000\ fs^3$. My relevant thesis point to these new scientific results is the following:

> **T.1:** I developed a spectrally resolved interferometer assisted by second harmonic generation. Thanks to this innovation, I was able to overcome the limited spectral resolution of commercially available spectrometers in the mid infrared spectral domain. I achieved this by transferring the spectral phase information in the near infrared spectral domain, where commercial spectrometers with higher spectral resolution are more common. I verified the newly developed second harmonic assisted spectrally resolved interferometer with materials with well-known spectral phase. I also compared it with the conventional spectrally resolved interferometer in terms of root mean square deviation and standard deviation, and it was found to perform better in both terms. Using this technique, I was able to measure the group delay spectrum of the newly manufactured dispersive mirror pair designed for postcompression in the mid infrared spectral domain, and I found good agreement with the designed value. [36]

3.2. Postcompression of the MIR OPCPA system

This thesis point presents the postcompression of the MIR OPCPA system at ELI ALPS Research Institute. First the experimental layout of the postcompression stage is introduced, then the test of different materials for self-phase modulation is discussed. Finally, the two optical cycle pulse is characterized temporally.

3.2.1. Experimental setup

Practically, one of the major bottlenecks of the postcompression process is the subsequent spectral phase management upon the recompression of the broadband spectrum back to near FTL duration. The GDD of the spectrally broadened pulse can be easily compensated with material dispersion, however the TOD cannot be removed solely by material dispersion. Nonetheless, the combination of bulk materials and DMs is capable of compensating for both.

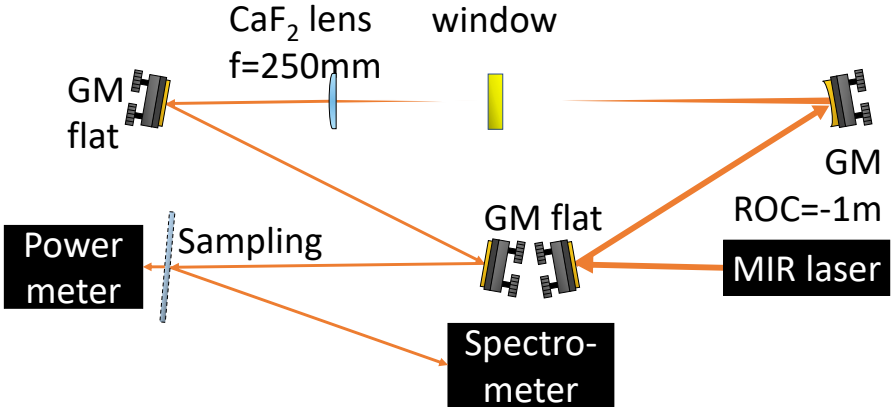

Figure 3.6: Schematic drawing of the postcompression setup. GM – gold mirror, ROC – radius of curvature

The schematic drawing of the postcompression setup driven by the MIR OPCPA beam is shown in *Figure 3.6*. A similar scheme was introduced in our previous work [35]. This former approach was further investigated and improved by using other materials for enhanced spectral broadening and aiding bulk compression with the DMs to reduce pulse duration below two optical cycles. The pulse (*130 μJ, 42 fs* in FWHM, *100 kHz*) was focused in air with a concave spherical GM, which had a *–1000 mm* radius of curvature (ROC) to guarantee a sufficiently large spot size in the focus without plasma development in air. GMs with shorter and longer ROC values were also tested; however, I achieved the best performance with this ROC value. In case of shorter ROC values, the SPM was less stable, while in case of longer ROCs, the SPM was less intense. The chosen ROC value was a good compromise between broadening and stability. Behind the focal plane of the focusing GM, thin plates were positioned at normal incidence along the beam propagation axis for SPM. The spectrally broadened beam was collimated with, CaF_2 BBAR (*2–5 μm*) plan-convex lens having a focal length of *250 mm*. After collimation, the beam was sampled with a specially coated sapphire sampler window having *7%* reflectance between *2.2 μm* and

4.2 μm, and nearly zero GDD and TOD for the reflected beam. I used the reflected beam for the spectrum and the CEP measurements.

3.2.2.Material selection

Several materials (BaF_2, CaF_2, gallium arsenide (GaAs), potassium bromide (KBr), KRS-5, magnesium fluoride (MgF_2), Si, YAG, zinc sulfide (ZnS) and zinc selenide (ZnSe)) were tested in the postcompression stage to get a sufficiently broad spectrum supporting a two optical cycle pulse duration in FTL. I investigated the average power, the FTL pulse duration, and the peak power calculated from these values in each case. The results are summarized in *Table 3.3.*

Material	d (mm)	$P_{average}$ (W)	τ_{FTL} (fs)	P_{peak} (W)
BaF_2	3	9.7	32.5	2.98
CaF_2	3	9.8	34.0	2.88
GaAs	1	5.1	28.2	1.81
KBr	2	9.6	30.0	3.20
KBr	4	9.5	22.0	4.32
KRS-5	2	7.3	20.1	3.63
KRS-5	4	7.2	22.6	3.19
MgF_2	3	9.9	36.8	2.87
Si	1	9.4	23.9	3.93
YAG	3	8.9	34.0	2.60
ZnS	3	9.3	36.1	2.58
ZnSe	1	9.5	37.4	2.54
ZnSe	2	9.3	35.8	2.60

Table 3.3: The investigated materials in the postcompression stage and their corresponding pulse parameters after the stage. d is the thickness of the window.

The largest amount of broadband spectra with high average power was achieved using BaF_2, KBr, Si and the combinations of these materials. In general, the double plate arrangements resulted in more broadband spectra than any of the single plate arrangements. The triple plate arrangements were also tested, however they did not improve any further the achievable peak power. Note that the operation of the spectral broadening unit in ambient air is limited by the absorption of carbon dioxide (CO_2) and water (H_2O) vapor [94]. The initial spectrum and the spectra with the double plate arrangements are shown in *Figure 3.7*. The spectral hole at *4.2–4.3 μm* is due to CO_2 absorption in air, while the modulation at *2.6–2.7 μm* is caused by the absorption of H_2O vapor in the air of the laboratory (*40%* relative humidity) [94]. The FTL pulse durations corresponding to the BaF_2-KBr (red), BaF_2-Si (orange) and KBr-Si (purple) double plate arrangements were *16.9 fs*, *16.7 fs* and *18.2 fs*, respectively. KBr was found to be very sensitive to laser induced damage, and since it is also hygroscopic, using the BaF_2-Si double plate combination proved to be the most advantageous choice. Further details are included in *Table 3.4*. The transmission of the BaF_2-Si

double plate combination was *83.6%* including both linear and nonlinear losses, yielding *9.15 W* right after the collimating lens (f=*250 mm*) of the broadening stage.

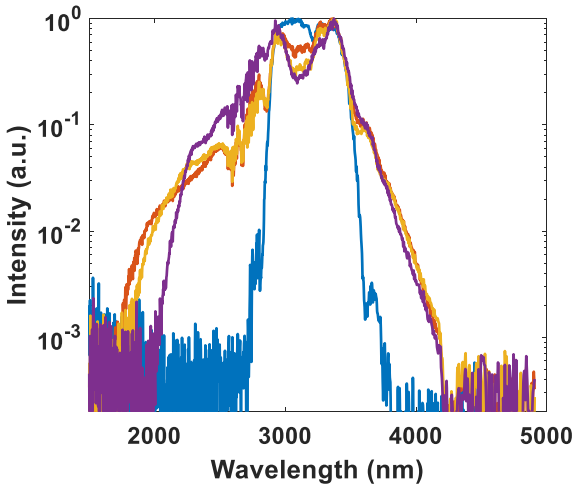

Figure 3.7: The initial spectrum (blue) before postcompression (MIR OPCPA). The broadened spectra after the BaF_2-KBr (red), the BaF_2-Si (orange) and the KBr-Si (purple) plate combinations.

Material	BaF_2	Si
d (mm)	3	1
Position[a] (mm)	530	650
Intensity[b] ($GWcm^{-2}$)	336.2	21.2
Loss (%)	8.9	8.2
FTL[c] (fs)	26.6	16.7

Table 3.4: Measured parameters of the postcompression setup. d is the thickness of the window. [a]Position between the focusing mirror and the first surface of the plates. [b] Intensity on the plates. [c] FTL of the spectrum after the plates.

3.2.3. Postcompression results

First, the pulses were recompressed without any DM, relying solely on compression with material dispersion. The best result was obtained by propagating the laser through a *2 mm* thick CaF_2 plate. This resulted in the compression of the pulses down to *25.5 fs* FWHM, which corresponds to less than two and a half optical cycles at *3170 nm* central wavelength. Next, I tested the compression with the combination of bulk materials and the DMs. With the help of three DMs aligned at *10°*, *25°* and *25°* AOIs, respectively, and a *5 mm* thick CaF_2 plate, the laser pulses were compressed down to *19.6 fs* FWHM, which is less than two optical cycles at this central wavelength. Several combinations were tested systematically by varying both the material thickness and the number of DMs, but the above arrangement provided the shortest measured pulse duration. The reflection losses of the CaF_2 window (*5.9%*) and the three DMs (*4.4%*) totaled *10.0%*. After recompression, I had an average power of *8.24 W*. The pulse duration (*19.6 fs*) was measured by a locally developed, all-reflective SHG FROG, the results of which are shown in *Figure 3.8.* The main peak contains *96.2%* of the pulse energy. The peak power of the laser pulses improved from *3.10 GW*

(MIR OPCPA output) to *4.04 GW* (postcompressed output), yielding an increment of *30.3%*. The output peak power is a significant improvement compared to an earlier work [35]. The schematic drawing of the finalized postcompression setup driven by the MIR OPCPA beam can be seen in *Figure 3.9.*

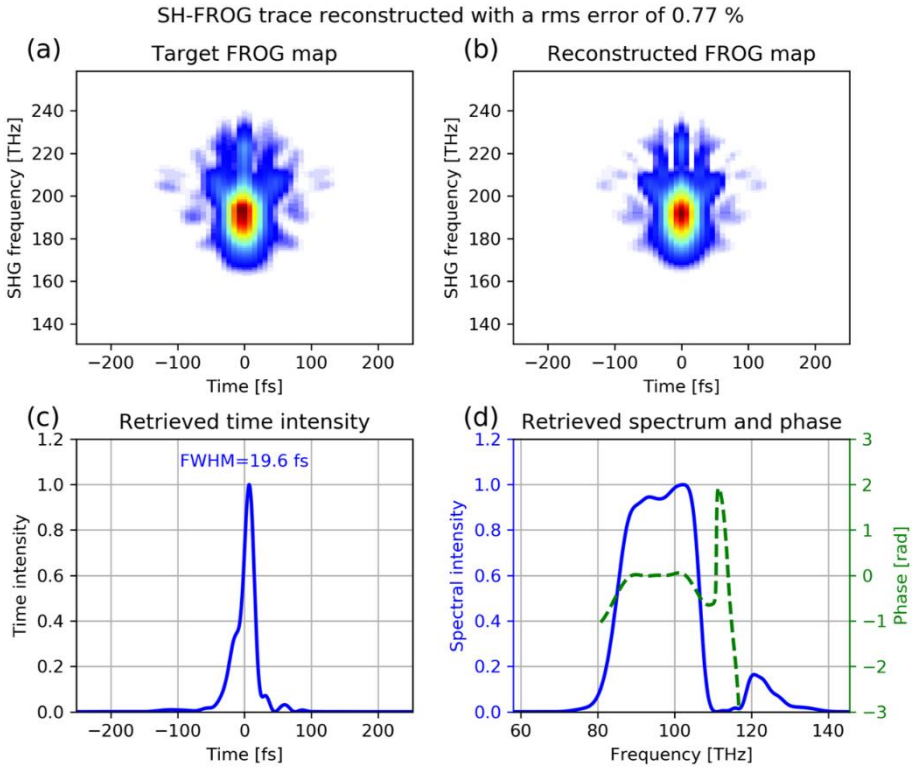

Figure 3.8: Pulse duration characterization with the SHG FROG device: (a) measured FROG trace, (b) reconstructed FROG trace, (c) reconstructed temporal profile and (d) reconstructed spectral intensity and phase.

The stability of the presented postcompression stage (see *Figure 3.9.*) was tested in a *4 h* period; the results are shown in *Figure 3.10.* During that time, the average power, the spectrum and the CEP (with active feedback loop) were monitored. The RMS of the power was *2.1%*, while the CEP was *240 mrad* for the entire measurement. The corresponding values of the OPCPA output (RMS: *0.7%* and CEP: *65 mrad*) are somewhat more stable, however it is an acceptable trade-off considering the shortened pulse duration and the increased peak power. The variation of the FTL of the spectrum was less than *1 fs* during the same period, which resulted in a stable pulse duration over hours. The above specifications make the postcompressed MIR output extremely attractive for future user experiments.

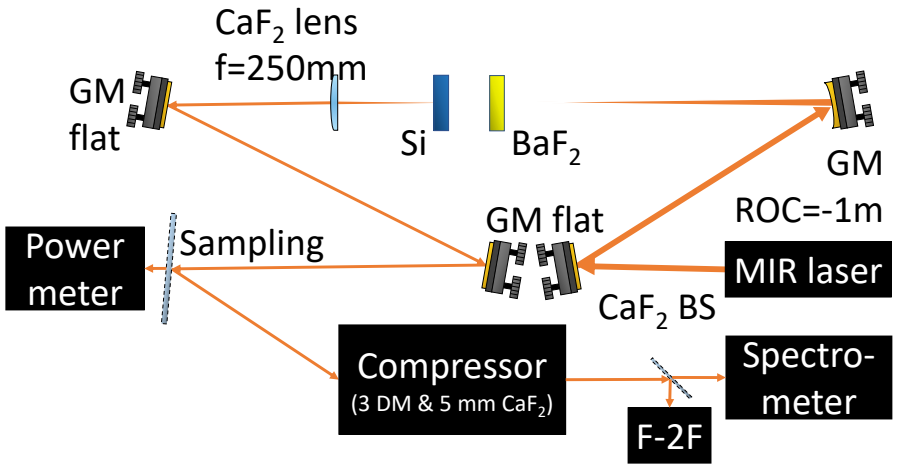

Figure 3.9: Schematic drawing of the postcompression setup. The compressor contains three DMs and a 5 mm thick CaF_2 window. GM – gold mirror, ROC – radius of curvature.

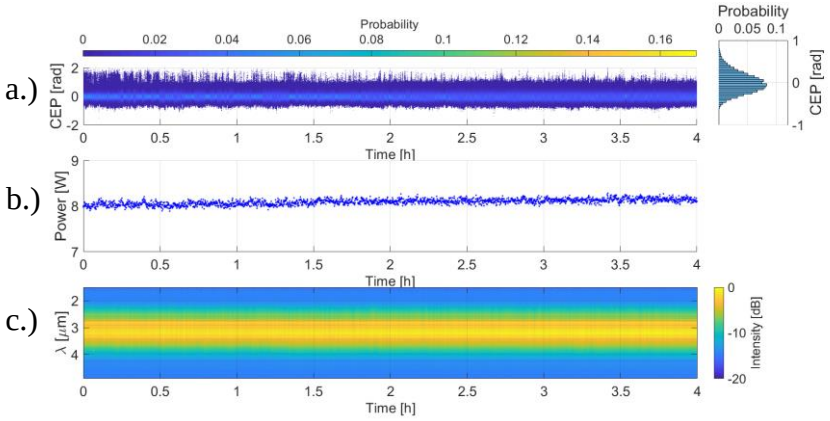

Figure 3.10: The results of the 4 h test of the postcompression stage: a.) the CEP, b.) the power and c.) the spectrum, respectively.

3.2.4. Discussion

In this thesis point the postcompression of the MIR OPCPA system at ELI ALPS Research Institute is introduced. One of the improvements compared to the earlier postcompression stage [35] was that I systemically investigated every available optical material in terms of transmitted pulse energy and spectral broadening after the postcompression stage. Thanks to this, I was able to continue working with the most suitable materials, i.e. BaF_2 and Si. The other improvement was the application the newly designed DMs (see details in *Chapter 3.1.3.*) in the postcompression stage. The combination of these improvements resulted in *19.6 fs* long, *82.4 μJ* energy pulses at a central wavelength of *3170 nm*. This pulse duration is less than two optical cycles at this central wavelength. My corresponding thesis point to these new scientific results is the following:

T.2: I used the dispersive mirror pair characterized in the first thesis point and developed the postcompression stage of the mid infrared laser system at ELI ALPS Research Institute. I tested several available materials for self-phase modulation. Barium fluoride, potassium bromide, and silicon were found to be best in terms of transmission and spectral broadening. I also tested different combinations of these materials, and the barium fluoride and silicon pair was found to have the highest potential peak power. I was able to compress the pulse almost down to the Fourier transform limit with the help a calcium fluoride window and three dispersive mirrors. I managed to shorten the pulse duration, which was originally five optical cycles (*~50 fs)* to less than two optical cycles (*~20 fs*) during postcompression. During my work, another aim was to increase the peak intensity of the system. Here I achieved a *30.3%* increment. [36]

3.3. Effect of the central wavelength on THz pulse generation

In this thesis point I present the results of my numerical simulations focusing on the effect of the central wavelength on THz pulse generation. First, I introduce the parameters of my numerical simulations, which were based on the parameters of the MIR OPCPA system at ELI ALPS Research Institute. After this, the effects of the central wavelength on SHG, tunnel ionization and THz pulse generation are discussed.

3.3.1. Parameters of the numerical simulations

In these numerical simulations, I examined the spectral range from *2.15 μm* up to *15.15 μm*. The examined spectral region was defined by Type-I SHG phase matching conditions (ooe) in a Z-cut ($\theta=0°$) GaSe nonlinear crystal [63-64]. The pulse peak power (*2.5 GW*) and the pulse duration expressed in optical cycles were kept constant in the investigated wavelength range in order to study only the wavelength dependence and minimize the other effects. The FWHM beam diameter was *27.5 μm* in the focus and *1.0 mm* at the GaSe. Both the temporal and spatial shapes of the pulse were chosen to be Gaussian. Nonlinear crystals with commercially available thicknesses (*10 μm*, *30μm* and *100 μm*) were explored. I found that the *10 μm* thickness was too thin for efficient SHG, while the *100 μm* thickness was too thick for efficient THz pulse generation. Therefore, I used the *30 μm* thick crystal in my research. The calculated intensity and the peak electric field were 1.50×10^{15} *W/m*^{2} and 7.51×10^{5} *kV/m* in the GaSe crystal, respectively.

3.3.2. The effect of the central wavelength effect on SHG

First, I investigated SHG in the nonlinear crystal. The results in the case of *3 μm* and *8 μm* central wavelengths of the fundamental pulse are shown in *Figure 3.11*. As one can see, the temporal walk-off between the fundamental pulse and its SH pulse decreases with increasing central wavelength. In case of a *3 μm* central wavelength, θ for Type-I phase matching is *15.0°*, the corresponding AOI is *45.1°* and the reflection loss is *11.1%* on each surface. The conversion efficiency at this wavelength is *35%*. In the case of an *8 μm* central wavelength, θ for Type-I phase

matching is *11.9°* and the corresponding AOI and reflection loss is *33.8°* and *15.5%* on each surface, respectively. The conversion efficiency at this wavelength is *14.0%*. θ has a minimal value of *10.5°* at *5.7 μm*. In general, the maximum conversion efficiency is *39%* at *2.5 μm*. Conversion efficiency slowly decreased as the wavelength moved away from *2.5 μm*. d_{eff} is proportional with *cos(θ)*, therefore its value decreases over *5.7 μm*.

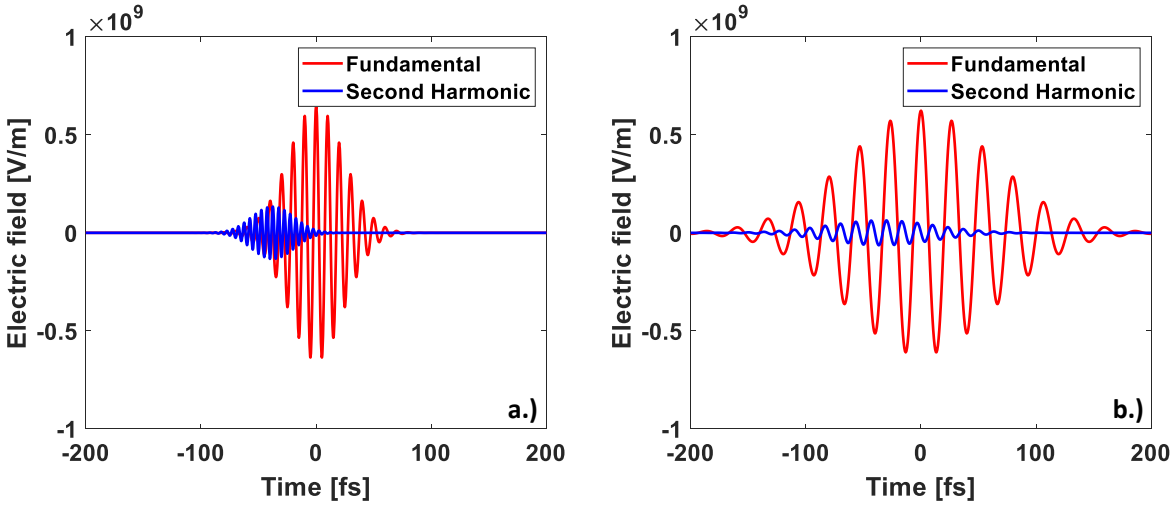

Figure 3.11: The fundamental (red) and its SH (blue) pulse electric field, when the central wavelength is a.) 3 μm and b.) 8 μm.

In the focus, the peak electric fields of the *3 μm* fundamental pulse and its SH pulse were 6.5×10^5 *kV/m* and 1.3×10^5 *kV/m*, respectively. The pulse durations were *4.0* optical cycles and *6.2* optical cycles, respectively. In the focus, the peak electric field of the *8 μm* fundamental pulse and its SH pulse were 6.2×10^5 *kV/m* and 0.6×10^5 *kV/m*, respectively. The pulse durations were *4.0* optical cycles and *5.7* optical cycles, respectively. The fundamental pulse's peak electric field and pulse duration did not change significantly. On the other hand, the SH pulse's peak electric field and pulse duration slowly decreased with the carrier wavelength.

3.3.3. The effect of the central wavelength on tunnel ionization

Next, I investigated the tunnel ionization of nitrogen, especially its electron density and velocity as a function of the central wavelength shown in *Fig. 3.12.* Tunnel ionization mainly takes place at moments when the electric field is the most intense. Therefore, the tunnel ionization process is not continuous, it occurs in a cascading fashion, representing the optical cycles in the electric field, which is clearly visible in *Figure 3.12.a.* Tunnel ionization itself is independent of the central wavelength. Despite this, there is a visible increase in electron density depending on the carrier wavelength as shown in *Figure 3.12.a.* This increase can be explained with the choice of simulation parameters. The constant peak power (*2.5 GW*) and the pulse duration (*4* optical cycles) require increasing pulse energy, which impacts tunnel ionization. Electron density reaches its maximum value (*0.06%*) at *14.1 μm* followed by a rapid decrease as a function of the central wavelength. The reason of the reduction in electron density is due to the reflection loss from the surfaces of the nonlinear crystal. For a Z-cut ($\theta=0°$) GaSe crystal, the reflection loss reaches its

minima at *2.3 μm* and *14.3 μm*, where the AOIs are close to the Brewster's angle. Outside this spectral region (*2.3–14.3 μm*), the reflection loss increases rapidly and makes the Z-cut (*θ=0°*) GaSe crystal ineffective for SHG. The reflection loss reaches its maxima at *2.15 μm* and *15.15 μm*, where the AOIs reach *90°*. Outside of this spectral region, phase matching for Type-I (ooe) SHG in Z-cut (*θ=0°*) GaSe crystals is not possible. Another very important factor in THz pulse generation is the drift velocity of the electrons. As shown in *Figure 3.12.b.*, the velocity of the electrons continuously increases as a function of the central wavelength of the fundamental pulse.

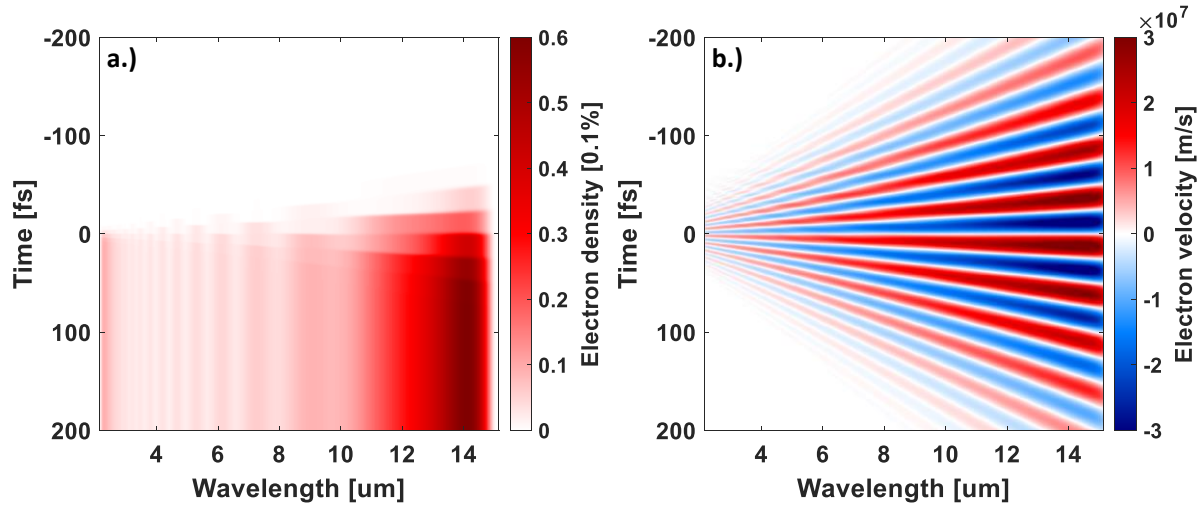

Figure 3.12: The electrons' a.) density and b.) velocity as a function of the central wavelength of the fundamental pulse.

3.3.4. The effect of the central wavelength on THz pulse generation

Based on the above results, THz pulse generation was investigated as a function of the central wavelength, as shown in *Figure 3.13.* The THz pulse electric field is shown in *Figure 3.13.a.*, and its spectrum is shown in *Figure 3.13.b.* as a function of the central wavelength. The cutoff frequency of the spectrum was chosen to be *8.8 THz*, which is a commercially available THz low pass filter. [96] Other, more broadband THz low pass filters are also available [96], but they may transmit part of the fundamental pulse, which makes it difficult to characterize the THz pulse itself. The electric field of THz pulses reaches its maximum at *12.3 μm*, but it also has several local maxima at *12.3 μm*, *9.1 μm*, *7.3 μm*, *6.2 μm* and so on because of the propagation of the two-color pulses in the nonlinear crystal. The phase velocity is strongly wavelength dependent; therefore, the fundamental pulse and its SH pulse have different phase velocities. When the two pulses have a *±π/2 rad* RP difference, a maximum can be observed in the THz electric field. Minima are observed at *0π rad* or *±1π rad* RP differences. In case of the thicker (*100 μm*) nonlinear crystals, the THz intensity is more densely modulated, while in case of the thinner (*10 μm*) nonlinear crystals, the THz intensity is less rarely modulated compared to the *30 μm* thickness. As a result of this sensitivity to the RP, one needs a simple, but robust method as presented in this thesis later (*Chapter 3.4*) to control the RP for THz pulse generation.

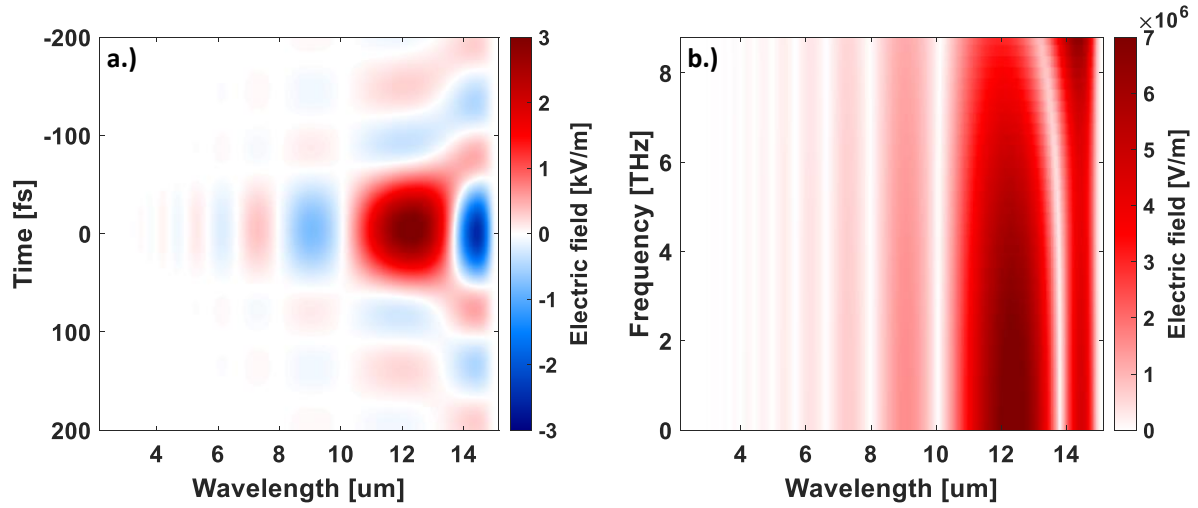

Figure 3.13: The THz pulse in the a.) temporal and b.) spectral domain as a function of the central wavelength.

When the central wavelength lies in the MIR or in the LWIR spectral domain, the separation of the fundamental and the THz pulses becomes difficult due to the fact that broadband pulses are needed for broadband THz pulses generation. Without the correct low pass filters, some part of the fundamental pulses may also pass through, causing problems with THz pulse detection (an interference pattern may appear, which can affect the measured parameters). Therefore, the correct separation of the fundamental and the THz pulses is critical for this process. The peak electric fields of THz pulses were calculated as a function of the central wavelength for various low pass filters [96] as shown in *Figure 3.14.* The strongest THz electric field was generated at *12.3 μm*, which wavelength position is roughly independent of the cutoff frequency. For *10.9 THz, 8.8 THz, 5.5 THz, 4.3 THz* and *3.2 THz* low pass filters the scaling laws were found to be $\sim\lambda^{3.41}$, $\sim\lambda^{3.47}$, $\sim\lambda^{3.54}$, $\sim\lambda^{3.56}$ and $\sim\lambda^{3.58}$, respectively, where λ is the central wavelength of the fundamental pulse. Please note that the scaling law was found to be $\sim\lambda^{9.03}$, $\sim\lambda^{9.13}$, $\sim\lambda^{9.26}$, $\sim\lambda^{9.29}$, $\sim\lambda^{9.33}$ for the *100 μm* thick nonlinear crystal, and $\sim\lambda^{2.08}$, $\sim\lambda^{2.17}$, $\sim\lambda^{2.28}$, $\sim\lambda^{2.31}$, $\sim\lambda^{2.33}$ for the *10 μm* thickness with the same low pass filters as above. From these values one can clearly see that the scaling law is very sensitive to SHG, it increases with SHG efficiency. Another noteworthy result here is the observation of a decrease in the scaling law as a function of the cutoff frequency. These results indicate that the lower frequencies are more sensitive to the carrier wavelength. The scaling laws are also being examined by other research groups [23-25, 28, 30, 69] in different spectral domains. The comparison of my results and previous results are summarized in *Table 3.5.* The lowest published value was $\sim\lambda^{1.7}$ in the spectral range from *0.8 μm* up to *2.0 μm* [24] and the highest one was $\sim\lambda^{14.5}$ in the spectral range from *2.4 μm* up to *2.6 μm* [28]. My results are in the range of previous works as these data show.

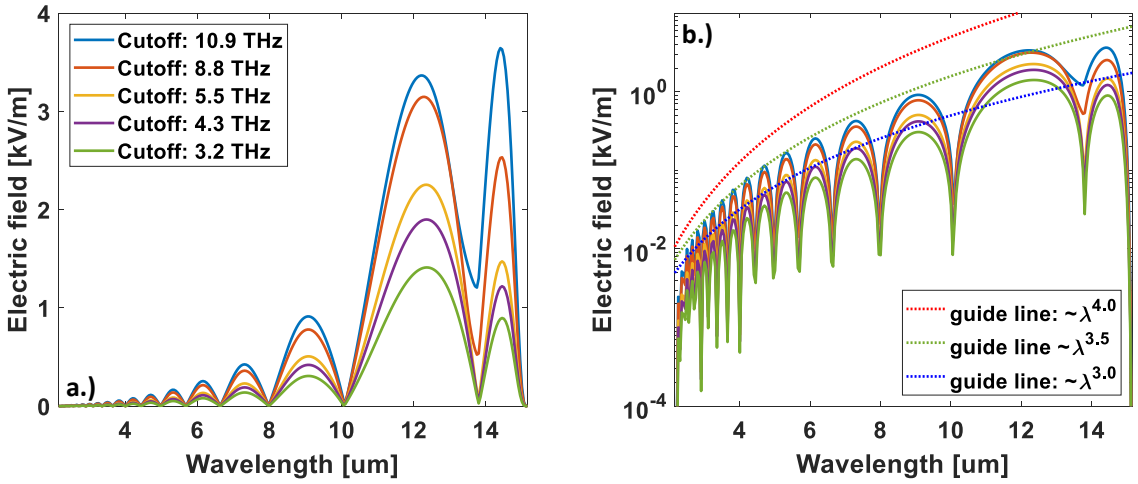

Figure 3.14: a.) The peak electric field of THz pulses as a function of the central wavelength of the fundamental pulse in the case of different THz low pass filters. b.) The same as a.) on a semilogarithmic scale. Different scaling laws are also included as a guide.

Wavelength range [µm]	Scaling law	References
0.8–4.0	$\lambda^{2.6}$	[69]
0.8–1.8	$\lambda^{4.6}$	[23]
0.8–2.0	$\lambda^{1.7\text{-}2.4}$	[24]
1.0–10.0	$\lambda^{1.8\text{-}2.1}$	[25]
1.2–1.5	$\lambda^{7.8\text{-}9.4}$	[28]
1.3–2.2	$\lambda^{4.6\text{-}8.1}$	[28]
2.4–2.6	$\lambda^{11.4\text{-}14.5}$	[28]
2.2–15.2	$\lambda^{9.0\text{-}9.3}$	100 µm GaSe
2.2–15.2	$\lambda^{3.4\text{-}3.6}$	30 µm GaSe
2.2–15.2	$\lambda^{2.1\text{-}2.3}$	10 µm GaSe

Table 3.5: The scaling laws of THz pulse generation as a function of the carrier wavelength of the fundamental pulse.

Next, I compared the efficiency of THz pulse generation from MIR and LWIR OPCPA sources and Ti:Sapphire lasers, which are still the most common sources for this type of THz pulse generation [45, 70-74, 76-78]. The central wavelength of Ti:Sapphire lasers is around *0.8 µm*, which means the GaSe nonlinear crystals cannot be used for SHG. In the NIR spectral regime, the most often used nonlinear crystal for SHG is the BBO. Its refractive index [97] and the effective nonlinear coefficient [98] are taken from literature. To provide a comparison, the same pulse parameters, i.e. four optical cycle pulse duration and *2.5 GW* peak power are used here too, but at

0.8 μm central wavelength. The thickness of the BBO was chosen to be *100 μm* and $\theta=29.2°$ and $\varphi=90°$, respectively. The cutoff frequency was also chosen to be the same as above (*8.8 THz*). The peak electric field of the generated THz pulse was 3.2×10^{-3} *kV/m*, in contrast with the MIR laser ($\lambda=3.3$ *μm*) it was 2.5×10^{-2} *kV/m* and with LWIR laser ($\lambda=7.3$ *μm*) it was 3.6×10^{-1} *kV/m*. Based on these results, I estimated that the generation of THz pulses with MIR sources is one, while with LWIR sources it is two orders of magnitude more efficient compared to the Ti:Sapphire lasers using the exact same pulse parameters.

3.3.5. Discussion

In this thesis point, I performed numerical simulations to investigate THz pulse generation with four optical cycle MIR and LWIR pulses in nitrogen plasma. I found that in the examined spectral range, from *2.15 μm* to *15.15 μm*, the generated THz pulse had several local maxima and the global maximum was at *12.3 μm*. The number of the local maxima increases with the thickness of the nonlinear crystal due to the RP difference of the two-color pulses during propagation. In addition, the optimal central wavelength was insensitive to the cutoff frequency. In contrast, the scaling law was sensitive to both the cutoff frequency and the thickness of the nonlinear crystal. The comparison of the efficiency of THz pulse generation by various sources under the same pulse parameters showed that the expected peak electric field of the THz pulses was one order of magnitude higher in case of MIR systems ($\lambda=3.3$ *μm*) and two orders of magnitude higher in case of LWIR systems ($\lambda=7.3$ *μm*) when compared to typical Ti:Sapphire laser systems ($\lambda=0.8$ *μm*). My corresponding thesis point to these new scientific results is the following:

> **T.3:** I investigated the possibility of using the mid infrared system at ELI ALPS Research Institute to generate terahertz pulses in nitrogen plasma with two-color pulses. With numerical simulation I investigated the efficiency improvement in terahertz pulse generation with mid and longwave infrared two-color pulses compared to near infrared two-color pulses with the same input pulse parameters. I investigated the spectral domain from *2.15 μm* to *15.15 μm* and tested different thicknesses of the nonlinear crystal. I found that the scaling law of the terahertz pulse generation increases with increasing nonlinear crystal thickness. From this I concluded that terahertz pulse generation is very sensitive to second harmonic generation. Furthermore, I investigated the scaling law with different cutoff frequencies and found that it slowly increases with decreasing cutoff frequency. From this I concluded that the lower frequency part of the terahertz spectrum is more sensitive to the driving wavelength. Finally, I found that terahertz radiation generated with mid infrared (*3.3 μm*) and longwave infrared (*7.3 μm*) is by one and two orders of magnitude more intense than the terahertz radiation generated with near infrared (*0.8 μm*) two-color pulses. [30]

3.4. Relative phase control for THz pulse generation

In this thesis point I present the results of my numerical simulations of the RP control of the two-color pulses for THz pulse generation. First, I introduce the importance of the RP control and then discuss material selection and testing for RP control. The fundamental pulse parameters were the

same as in *Chapter 3.3.*, however the central wavelength was constant ($\lambda = 3.2\ \mu m$) in this thesis point.

3.4.1. Importance of the relative phase

The small group and phase velocity differences between the fundamental and its SH pulse in the MIR and LWIR spectral domains require precise control of the RP during experiments [28]. After the SHG process, the RP between the fundamental and its SH pulses depends on the thickness and the refractive index of the nonlinear crystal. Please note that the THz pulse generation process is optimal when the RP is $\pm\pi/2\ rad$ [43-44]. A common way to control the RP between the two-color pulses is to collinearly propagate them in air, which is a straightforward solution in experiments with Ti:Sapphire laser systems. For MIR sources, due to the smaller dispersion of air, the two-color pulses have to copropagate several meters to change the RP by $\pm\pi/2\ rad$. In addition, the absorption of air can be significant in this spectral domain [94], and may result in unwanted intensity and phase modulations of the two-color pulses. This is another reason why copropagation in air in this case is not a practical solution. Alternatively, two-color pulses can be propagated along different beam paths, where pulses can be separated and recombined with the help of a pair of DcM, which are not widely available in the MIR spectral range with low losses. A better option is to use materials with a higher refractive index and larger dispersion [30, 69] than air. The advantage of this approach is its compactness, which reduces the optical path significantly and it simplifies the experimental configuration since it does not require any pulse separation and recombination.

3.4.2. Materials for relative phase control

Although, there are numerous potential materials which are transparent in the examined spectral region, I chose three practical criteria during the investigation. First of all, the materials must be commercially available. The most common materials that meet this criterion and are transparent in the MIR spectral region are Si, sapphire (Al_2O_3), ZnSe, BaF_2, CaF_2, LiF, and MgF_2. Birefringent materials are not considered for this purpose to avoid unwanted nonlinear effects during the control of the RP; therefore, Al_2O_3 and MgF_2 are eliminated. The materials must also exhibit negative GVD, because it can cancel out the positive GVD of the GaSe crystal [63], which would improve the temporal overlap between the two-color pulses and hence improve the efficiency of THz pulse generation; therefore, Si and ZnSe were not selected for my numerical simulations.

In this thesis, alkaline earth halides (BaF_2 and CaF_2) and alkaline halide (LiF) were closely examined. Each of these materials fulfills the three requirements mentioned above, which make them suitable candidates for controlling the RP of the two-color pulses. The first two materials investigated here are alkaline earth halides [90]. The RP control ability of these two materials is shown in *Figure 3.15.* and *Figure 3.16*, which depict the peak electric field of the THz pulse as a function of the thickness of the window and the AOI. The peak electric field of the THz pulse weakly depends on the AOI. The slow variation can be explained with the Fresnel reflection. The reflection loss decreases with the AOI up to the Brewster's angle, which results in an increase in the peak electric field of the THz pulse. The reflection loss increases with the AOI above the

Brewster's angle, which results in a decrease in the peak electric field of the THz pulse. Furthermore, the peak electric field of the THz pulse exhibits a slow and rapid variation as a function of the thickness of the plate (*Figure 3.15.b* and *Figure 3.16.b*). The slow variation is due to the temporal overlap between the two-color pulses. At the bottom of the figures, the temporal overlap increases, which also increases the THz pulse intensity. Beyond the optimal thickness, the temporal overlap deteriorates quickly and yields the observed decrease in the THz pulse's intensity. The rapid variation in the peak electric field of the THz pulse observable in the figures is due to the continuous change of the RP between the two-color pulses in the plates [43-44]. As one can see, both BaF_2 and CaF_2 are able to control the RP of the two-color pulses producing increased THz pulse intensity via compensating the temporal walk-off between the pulses. The optimal thickness of the BaF_2 plate was found to be *4.7 mm* with an AOI of *56°* for optimum THz pulse generation with the above-mentioned fundamental pulse parameters. The optimal thickness of the CaF_2 plate was found to be *1.45 mm* with an AOI of *55°* for optimum THz pulse generation with the above-mentioned fundamental pulse parameters.

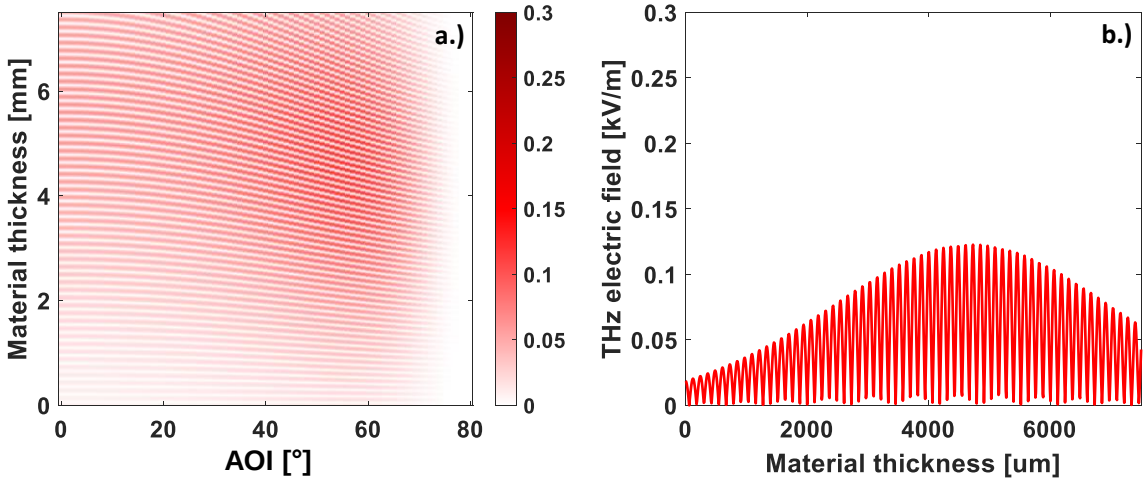

Figure 3.15: a.) The peak electric field of the THz pulse as a function of the thickness of the BaF_2 plate and the AOI. b.) The peak electric field of the THz pulse as a function of the thickness of the BaF_2 plate at the optimal AOI (56°).

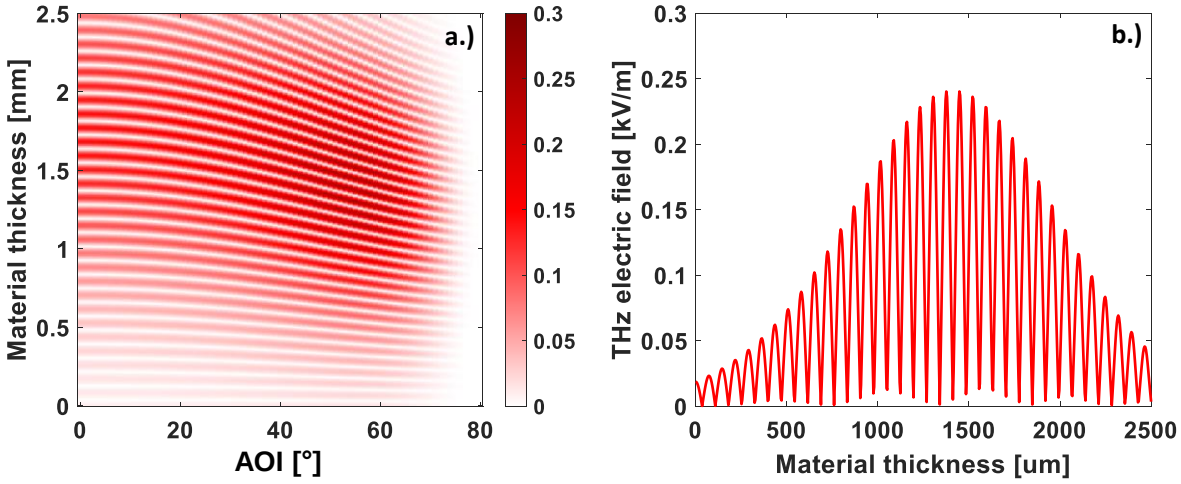

Figure 3.16: a.) The peak electric field of the THz pulse as a function of the thickness of the CaF_2 plate and the AOI. b.) The peak electric field of the THz pulse as a function of the thickness of the CaF_2 plate at the optimal AOI (55°).

The last material is LiF, which is an alkali halide [99], LiF. The RP control ability of this material is shown in *Figure 3.17*. LiF is also a reasonable choice of material to control the RP of the two-color pulse for maximizing the THz pulse intensity. The optimal thickness of the LiF plate was found to be *0.5 mm* with an AOI of *55°* for optimum THz pulse generation with the above-mentioned fundamental pulse parameters. Based on these results, all these three fluorides are able to control the RP of the two-color pulses. The thinnest commercially available BaF_2, CaF_2 and LiF windows are *0.5 mm*, *0.3 mm* and *0.5 mm* thick, respectively. Considering the currently available commercial windows and the results from my simulations, I conclude that LiF and CaF_2 are feasible choices for RP control of the two-color pulses.

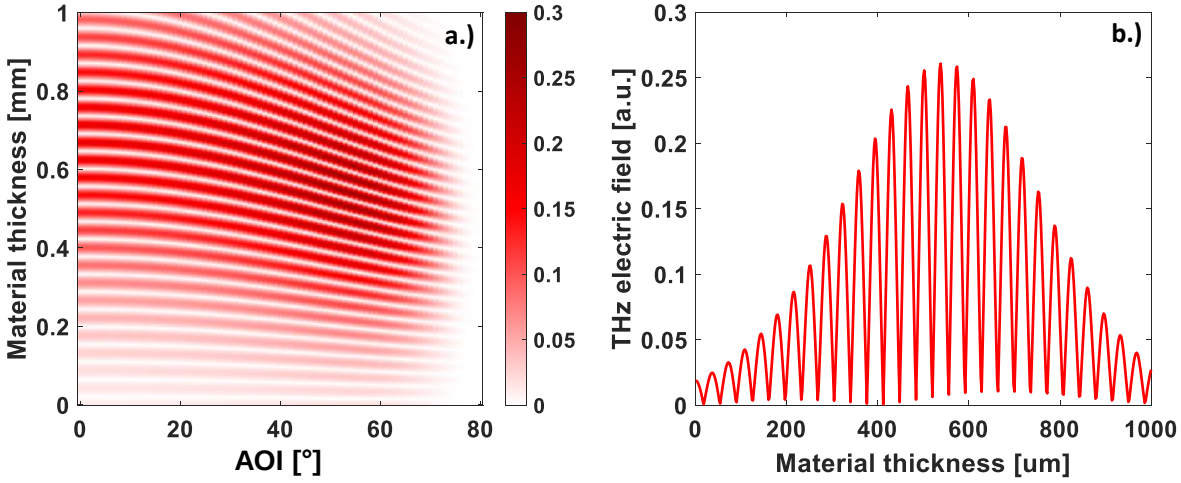

Figure 3.17: a.) The peak electric field of the THz pulse as a function of the thickness of the LiF plate and the AOI. b.) The peak electric field of the THz pulse as a function of the thickness of the LiF plate at the optimal AOI (55°).

3.4.3. Discussion

In this thesis point, I investigated the RP control of the MIR two-color pulses with co-propagation through thin fluoride plates. Materials with negative GVD are also able to compensate the positive GVD of the nonlinear crystal, thereby improving the temporal overlap between the two-color pulses, which also improves the efficiency of THz pulse generation. I numerically tested every chosen material with different thicknesses and AOIs to find the optimal condition for the most intense THz pulse generation. I found that LiF and CaF_2 are the best candidates for this purpose. My corresponding thesis point to these new scientific results is the following:

> **T.4:** I investigated the relative phase tuning ability of thin dielectric plates with mid infrared, two-color pulses during terahertz pulse generation in nitrogen plasma. My aim was to determine which material is best suited for fine-tuning the relative phase between the two-color pulses, and thus also for optimizing the peak intensity of the terahertz pulse. I investigated terahertz pulse generation with several materials, transparent in the mid infrared spectral domain. I also simulated the terahertz pulse generation with different material thicknesses and angles of incidence. I found that the best candidates are different fluorides, especially lithium and calcium fluoride. These materials have negative group velocity dispersion, and thanks to this they are not just able to control the relative phase between the two-color pulses but also improve the temporal overlap between them, which further increases the efficiency of terahertz pulse generation. [30]

3.5. The effect of pulse duration on THz pulse generation

In this thesis point I present the results of my numerical simulations modeling the effects of the duration and the polarization angle of the fundamental pulse on THz pulse generation. First, I introduce the parameters of the simulations, which were based on the MIR OPCPA system at ELI ALPS. Then I discuss in detail the effects mentioned above. Finally, the central wavelength of the fundamental pulse is also considered.

3.5.1. THz pulse generation with a *3.2 μm* fundamental pulse

I examined the effect of pulse duration and that of the polarization angle of the fundamental pulse on THz pulse generation. The pulse duration I considered covered the range from *1.2* to *5.0* optical cycles, while the polarization angle changed from *0°* to *50°*, where *0°* is the purely eo polarization and *90°* is the purely o polarization. The pulse peak power (*2.5 GW*) was kept at a constant level. The FWHM beam diameter was *20 μm* in the focus and *1.0 mm* at the GaSe crystal. Both the temporal and spatial shapes of the pulse were chosen to be Gaussian. There are commercially available GaSe nonlinear crystals with thicknesses *10 μm*, *30 μm* and *100 μm*, however I only explored the thinnest one in my thesis due to the few optical cycle pulse duration. I found that the thicker ones are not suitable for efficient SHG and THz pulse generation, because of the very broadband fundamental pulses investigated in this thesis point. The calculated intensity and peak electric field are 1.5×10^{15} W/m^2 and 7.5×10^{5} kV/m at the GaSe crystal, respectively.

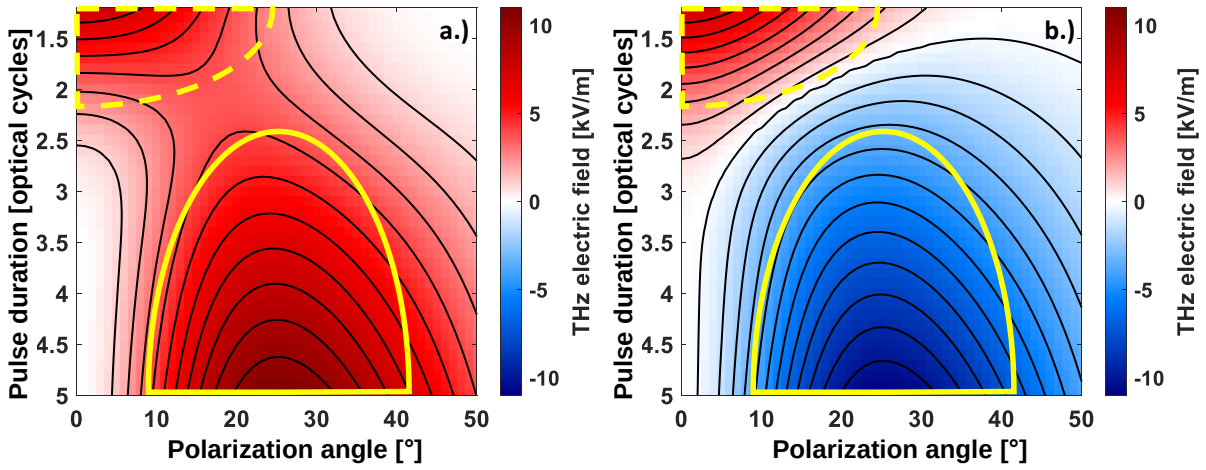

Figure 3.18: The peak power of the THz pulse as a function of pulse duration and the polarization angle in case of a.) +π/2 rad and b.) –π/2 rad RP. The central wavelength of the driving laser pulse is 3.2 μm.

I investigated THz pulse generation at *3.2 μm* (one optical cycle is equal to *10.7 fs*) central wavelength of the fundamental pulse. The results are shown in *Figure 3.18* in case of *±π/2 rad* RP between the fundamental and its SH pulses. For the *+π/2 rad* RP (see *Figure 3.18.a*), there are two regions, where efficient THz pulse generation can be realized. The first is the conventional region, where the two-color or double-color scheme is the more effective process. This can be seen in the bottom-middle of *Figure 3.18.a* (highlighted with a solid yellow line). In this case, the maximum THz electric field is *11.0 kV/m* at *5.0* optical cycles and *25°* polarization angle. Interestingly, the calculation shows that there is a second region where THz generation is just as efficient as in the double-color scheme utilizing only one color or a single color, which means that the THz pulse is generated only by the fundamental laser pulse without its SH. This can be seen in the top-left of *Figure 3.18.a* (highlighted with a dashed yellow line). In this case, the maximum THz electric field is *7.9 kV/m* at *1.2* optical cycles and *0°* polarization angle. As a reminder, the *0°* polarization angle indicates that the fundamental pulse polarization is purely eo polarized, hence no SHG occurs in the GaSe crystal. This implies that the nonlinear crystal can be abandoned in this scheme, which terminates the reflection loss and the negative effect of dispersion on THz pulse generation, which further improves the efficiency of the process. The shift between the two regions is continuous and it occurs at *1.7* optical cycles (*18.1 fs*).

For the *–π/2 rad* RP (see *Figure 3.18.b*), there are also two regions for efficient THz pulse generation. As discussed above, the conventional region can be seen in the bottom-middle of *Figure 3.18.b* (highlighted with a solid yellow line). In this case, the maximum, which is technically a minimum, THz electric field is *–11.0 kV/m* at *5.0* optical cycles and at a polarization angle of *25°*. As one can see, the sign of the maximum THz electric field is inverted, when the sign of the RP is inverted. The unconventional region can be seen in the top-left of *Figure 3.18.b* (highlighted with a dashed yellow line). In this case, the maximum THz electric field is *7.9 kV/m* at *1.2* optical cycles and at a polarization angle of *0°*. As one can see, the sign of the maximum

THz electric field is not inverted, since the single-color scheme is independent of the SH pulse, and hence it is also independent of the RP. The shift between the regions is not continuous, and it happens at *2.1* optical cycles (*22.4 fs*).

There is also a third, transitional region between the single- and double-color schemes. The first is the already discussed unconventional region, where the single-color THz pulse generation becomes dominant. This region starts below *1.7* optical cycles (*18.1 fs*). The second is the already presented conventional region, where the double-color THz pulse generation is more efficient and furthermore THz pulse generation is not sensitive to the sign of the RP. The double-color scheme with *–π/2 rad* and *+π/2 rad* RP generates THz pulses with the same absolute peak power, but the electric field has an opposite sign. This region starts above *3.2* optical cycles (*34.1 fs*). The third, transitional region is between the single- and double-color regions, where the double-color THz pulse generation is still more effective, but THz pulse generation is sensitive to the sign of the RP. The double-color scheme with *–π/2 rad* and *+π/2 rad* RP generates THz pulses with different absolute peak powers.

To better understand the transition between the single- and double-color schemes, I explored the details of the numerical simulations showing the contributions from the various steps. Here, I selected a simulation where the central wavelength was *3.2 μm* and the pulse duration corresponded to *2.0* optical cycles (*21.3 fs*). The results are shown in *Figure 3.19*. The blue color indicates the single-color scheme at a polarization angle of *0°*. The orange color indicates the double-color scheme at a polarization angle of *25°* in case of *+π/2 rad* RP, hereinafter positive double-color. The red color indicates the double-color scheme at a polarization angle of *25°* in case *–π/2 rad* RP, hereinafter negative double-color.

The external electric field, shown separately in *Figure 3.19.a.*, is a little more intense in case of the single-color scheme, than in the double-color schemes. This is due to the reduced losses (reflection and nonlinear conversion) of the fundamental pulse. The tail of the external electric fields in both double-color schemes is more asymmetric compared to the single-color scheme due to the presence of their associated SH pulse. The orientation of this asymmetry depends on the RP between the two-color pulses.

The electron density for each scenario is shown in *Figure 3.19.b*. In case of the single-color scheme, it is *0.45%*, while in the positive and negative double-color schemes the respective values are only *0.16%* and *0.15%*. These values are approximately one third of the single-color scheme, which is a consequence of the slightly less intense electric field. I would like to mention that the ionization rates are an exponential function of the external electric field (*Equation 2.25*). Hence a minor change in the external electric field triggers a major change in electron density. In every case, ionization occurs in three significant steps. In case of the single-color and the positive double-color schemes the second step is the most prominent, while in case of the negative double-color scheme, the first step is the most prominent, as it can be seen in *Figure 3.19.b*.

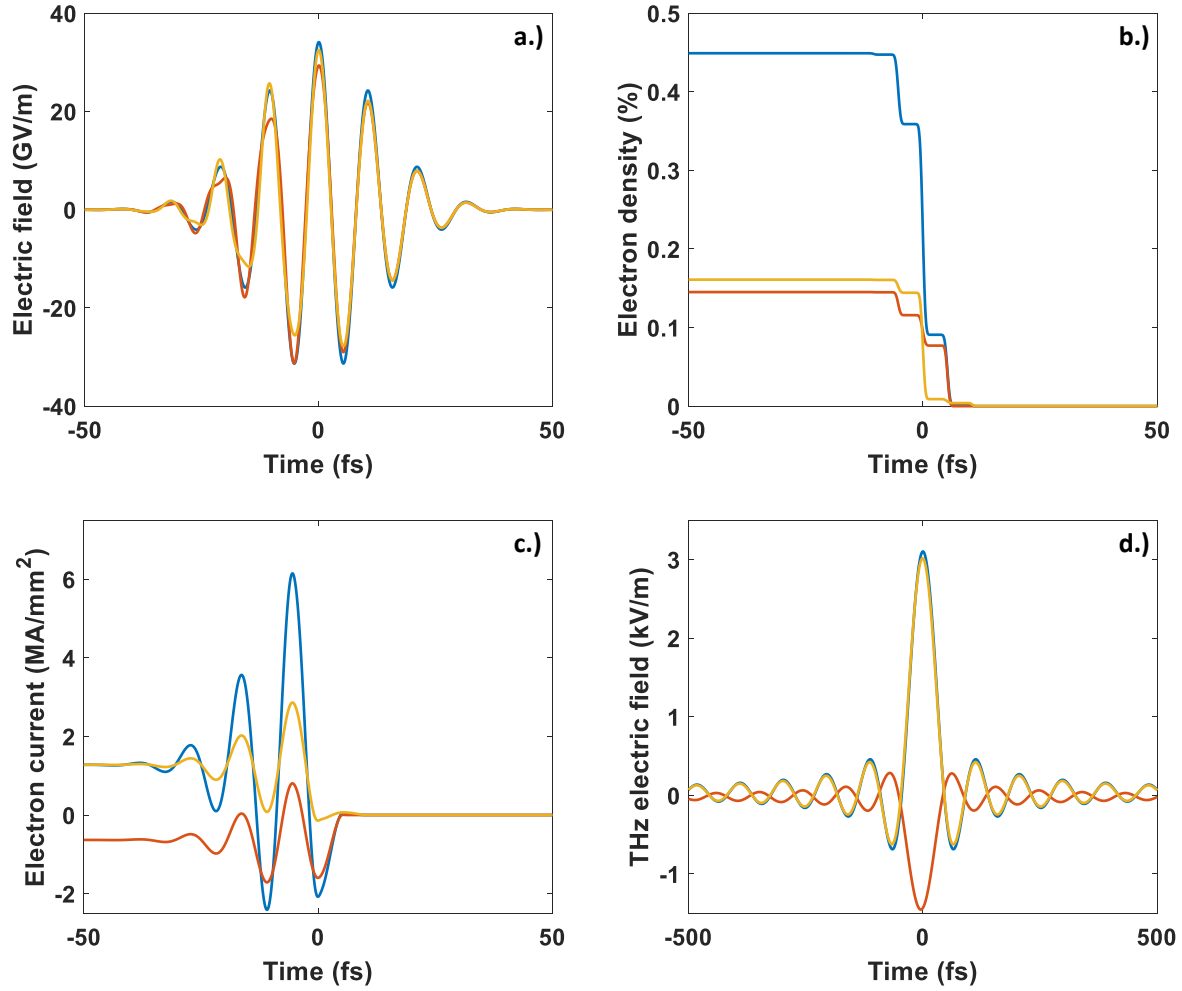

Figure 3.19: a.) The external electric field, b.) the electron density, c.) the electron current and d.) the THz electric field. The blue color indicates the single-color scheme at a polarization angle of 0°. The orange and red colors indicate the positive and negative double-color schemes at a polarization angle of 25°, respectively. The central wavelength is 3.2 μm and the pulse duration is 2.0 optical cycles (21.3 fs) in every case.

The TEC of every case is shown in *Figure 3.19.c*. In the single-color and positive double-color schemes a strong, positive current builds up, which is due to the dominant second step during ionization, which overlaps temporally with the maximum of the external electric field. Thanks to this, the first two steps of the process have different intensity and sign, and yield a strong positive TEC in the end. The levels of the two TECs are similar, despite being built up from different external electric fields. The external electric field is more intense and less asymmetric in case of the single-color scheme, while it is less intense, but more asymmetric in case of the positive double-color scheme. These results indicate that both properties play an important role in THz pulse generation. In case of the negative double-color scheme a weak, negative TEC builds up, which is due to the dominant first step during ionization. The second step during ionization is less dominant, but it overlaps temporally with the maximum of the external electric field. Thanks to

this, the first two steps of TEC formation have similar intensities, but different signs, which almost extinguish each other and develop a weak negative TEC in the end.

The THz electric fields of every case are shown in *Figure 3.19.d*. In case of the single-color and the positive double-color schemes a strong, positive THz electric field builds up from the strong, positive TEC. Since the TECs are similar, the THz electric fields that build up from them will be also similar. In case of the negative double-color scheme a weak, negative THz electric field builds up from the weak, negative TEC.

In summary of the above results, the most important parameters of the external electric field are intensity and asymmetry during the THz pulse generation. The generation of similar THz pulses is possible with different external electric fields. When intensity is concerned, the single-color scheme is preferred due to the minor losses (reflection and nonlinear conversion). In terms of asymmetry, it is more advantageous to use the double-color schemes. However, asymmetry increases with decreasing pulse duration in every scheme, and as a result, in the case of few optical cycle pulses, the single-color scheme will be more efficient as presented earlier.

3.5.2. THz pulse generation with a fundamental pulse at *2.5 μm to 4.0 μm*

In the next step, I investigated THz pulse generation from *2.5 μm* (one optical cycle is equal to *8.3 fs*) to *4.0 μm* (one optical cycle is equal to *13.3 fs*) central wavelength of the fundamental pulse. These results allow us to explore the effects of the central wavelength of the pumping laser pulse on THz pulse generation. The results are shown in *Figures 3.20-21*.

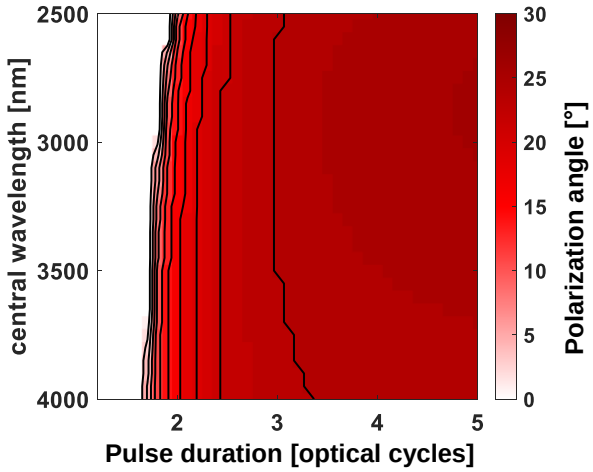

Figure 3.20: The optimal polarization angle of the fundamental pulse as a function of pulse duration and the central wavelength in case of the single-color / positive double-color scheme. The corresponding THz electric field is shown in Figure 3.21.a.

The optimal polarization angle is shown in *Figure 3.20* in case of single-color / positive double-color schemes. When the optimal polarization angle is equal to *0°*, the single-color scheme is more efficient than the positive double-color scheme. As a reminder, *0°* polarization angle means

that the polarization of the fundamental pulse is purely eo, hence no SHG occurs in the nonlinear crystal. The shift between the two schemes, which is the upper boundary of the unconventional region, is at *1.9* optical cycles (*15.9 fs*) and *1.6* optical cycles (*21.3 fs*) in case of *2.5 μm* and *4.0 μm* central wavelengths, respectively. As shown in *Figure 3.20*, the boundary of the unconventional region decreases with increasing central wavelength.

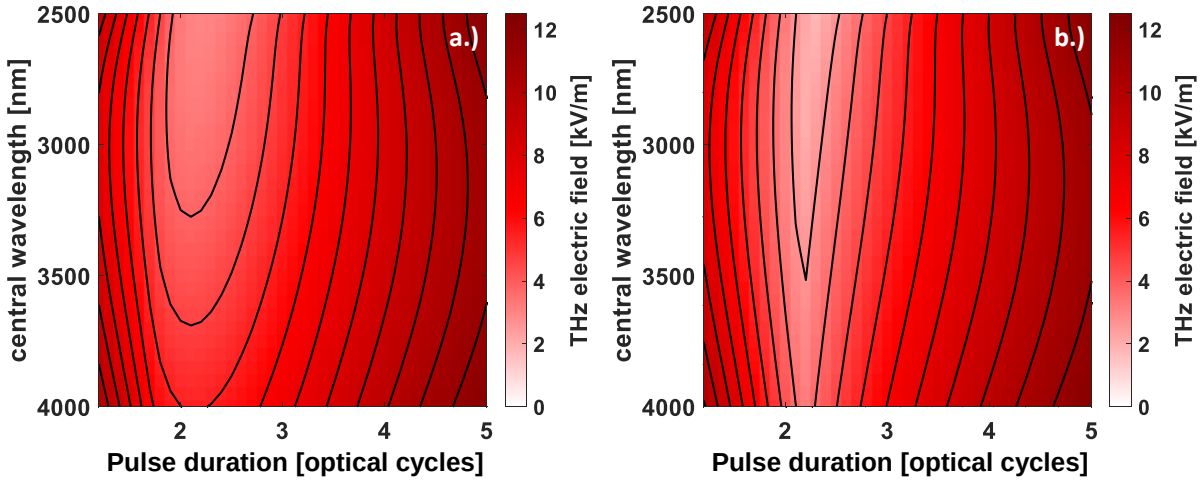

Figure 3.21: The optimal THz electric field of the fundamental pulse as a function of pulse duration and the central wavelength in case of a.) the single-color / positive double-color scheme and b.) the single-color / negative double-color scheme.

The optimal THz electric field is shown in *Figure 3.21* for the single-color / positive double-color schemes (RP is equal to $+\pi/2$ *rad*) (*Figure 3.21.a*) and for the single-color / negative double-color schemes (RP is equal to $-\pi/2$ *rad*) (*Figure 3.21.b*). The lower boundary of the conventional region was determined by comparing the positive and negative double-color schemes. When the difference between the two schemes is less than *1%*, one can speak of the conventional region. The lower boundary of the conventional region is at *3.2* optical cycles (*26.7 fs*) and *3.5* optical cycles (*46.7 fs*) in case of *2.5 μm* and *4.0 μm* central wavelengths, respectively. This boundary shifts to higher values with increasing central wavelength.

In conclusion, the most important result is that the upper limit (expressed in optical cycles) of the single-color approach increases, while the lower limit of the two-color approach decreases with increasing central wavelength. The former effect is likely to be related to the improving condition of the SHG. As the carrier wavelength increases, the efficiency of the SHG increases too, and the temporal overlap between the two-color pulses decreases. Both phenomena have a positive effect on THz pulse generation, which makes it understandable, why the increasing carrier wavelength makes it more difficult to reach and study the single-color approach. The latter effect is likely to be related to the increasing ponderomotive potential, which increases with the carrier wavelength. This explains why it is easier to reach and study the transient region.

3.5.3. Discussion

I examined the THz pulse generation as a function of the pulse duration and the polarization angle of the fundamental pulse at *3.2 μm* central wavelength. Three distinctly different regions have been identified, where the optimal pulse parameters are fundamentally different for the most efficient THz pulse generation. The first or conventional region, where the double-color scheme is dominant is above *3.2* optical cycles (*34.1 fs*). The second or unconventional region, where the single-color scheme is dominant is below *1.7* optical cycles (*18.1 fs*). The last region is the transitional region, where the double-color scheme is still dominant, but the sign of the RP is also dominant. In addition, I have found that the lower boundary of the conventional region increases with increasing central wavelength, while the upper boundary of the unconventional region decreases with increasing central wavelength. The numerical results presented in this study will provide important insights for future experiments, where the aim is to generate THz pulses with few optical cycle, MIR laser pulses. My corresponding thesis point to these new scientific results is the following:

> **T.5:** I investigated terahertz pulse generation in nitrogen plasma as a function of pulse duration and polarization angle. I identified three distinctly different regions, where the optimal pulse parameters for the most efficient terahertz pulse generation are different. The first or conventional region is where the two-color pulse scheme is dominant above *3.2* optical cycles (*34.1 fs* at *3.2 μm*). The second or unconventional region is, where the one-color pulse scheme is dominant below *1.7* optical cycles (*18.1 fs* at *3.2 μm*). The last or semi-conventional/transitional region is, where the two-color pulse scheme is still dominant, but the sign of the relative phase is also determinative. In the conventional region, two-color pulses with opposing relative phases generate terahertz pulses with the same absolute peak power, but this is not true in the transitional region. In addition, I found that the lower boundary of the conventional region increases with increasing central wavelength, while the upper boundary of the unconventional region decreases with increasing central wavelength. [79]

3.6. The effects of phases on the THz pulse generation

In this thesis point the results of my numerical simulations of the CEP and the RP effects on THz pulse generation are presented. First, the effects of these two phases on THz pulse generation are discussed as a function of pulse duration, and then they are further investigated as a function of the polarization angle.

3.6.1. The effect of phase on THz pulse generation as a function of pulse duration

In my thesis point, I continued to investigate THz pulse generation with few optical cycle MIR pulses. The carrier wavelength was *3.2 μm*, just like in my previous thesis points (*Chapters 3.3* to *3.5*). The examined pulse duration also covered the range from *1.2* to *5.0* optical cycles

(*Chapter 3.5*), while the investigated polarization angles were *10°*, *15°*, *20°*, *25°*, and *30°*. As a reminder, *0°* is when the pulse is completely eo polarized and *90°* is when the pulse is completely o polarized. The peak power of the pulse (*2.5 GW*) was kept at a constant level; the other pulse parameters were also the same as in my previous thesis point (*Chapter 3.5*). In this current thesis point, I focused on the effects of the CEP and the RP on THz pulse generation as a function of pulse duration.

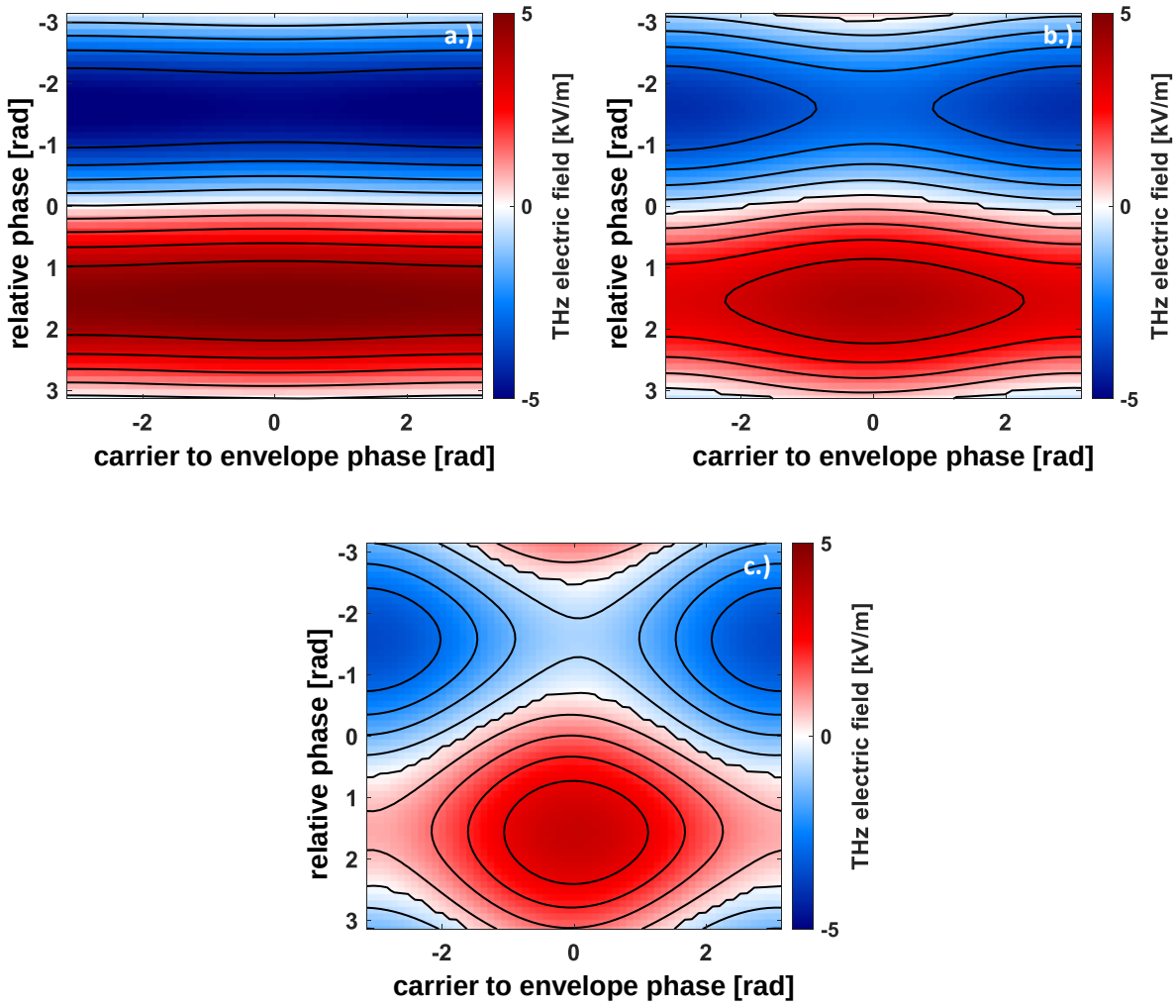

Figure 3.22: The peak electric field of the THz pulse as a function of the CEP (X-axis) and RP (Y-axis) in case of the following pulse durations: a.) 3.0 optical cycles (32.1 fs), b.) 2.5 optical cycles (26.8 fs) and c.) 2.0 optical cycles (21.4 fs). The central wavelength of the driving laser pulse is 3.2 μm and the polarization angle is 20°.

THz pulse generation as a function of the two phases is shown in *Figure 3.22.* for different pulse durations at a fixed polarization angle (*20°*). In case of *3.0* optical cycles (*32.1 fs*) (*Figure 3.22.a*), the CEP (X-axis) does not have any significant effect on THz pulse generation, however the RP (Y-axis) has a clearly visible effect on it. In case of *2.5* optical cycles (*26.8 fs*) (*Figure 3.22.b*), the importance of the CEP increases, while the importance of the RP

decreases. In case of *2.0* optical cycles (*21.4 fs*) (*Figure 3.22.c*), the former changes are more significant, as the pulse duration further decreases. These changes can be easily understood in the light of the previous thesis point (*Chapter 3.5*). As the pulse duration decreases, THz pulse generations moves away from the two-color to the one-color scheme (*Chapter 3.5*). This change is important in two aspects. First, as the pulse duration decreases, the need for SHG also decreases, which reduces the effect of the RP on THz pulse generation. Second, as pulse duration increases, the difference between the individual optical cycles decreases, which reduces the effect of the CEP on THz pulse generation.

For easier understanding, I only depicted the effects of the CEP and of pulse duration on THz pulse generation, while the RP was constant, as shown in *Figure 3.23.a*. As pulse duration decreases, the significance of the CEP increases. At this point, I need to define the sensitivity of THz pulse generation:

$$S = \frac{THz_{max} - THz_{min}}{THz_{max}}, \tag{3.1}$$

where THz_{max} and THz_{min} are the maximum and minimum of the electric field of the THz pulse, respectively. The sensitivity value changes between *0* and *2*. The *0* value indicates that THz pulse generation is not sensitive to the investigated parameter. In this case, THz_{max} and THz_{min} have the same sign and value. On the other hand, the two values indicate that THz generation is absolutely sensitive to the investigated parameter. In this case, THz_{max} and THz_{min} have the opposite sign and the same absolute value. The sensitivity of THz pulse generation to the CEP is 7.13×10^{-6}, 4.52×10^{-4}, 2.01×10^{-2} and 7.68×10^{-1} at *5*, *4*, *3*, and *2* optical cycles, respectively. As one can see, it increases with decreasing pulse duration.

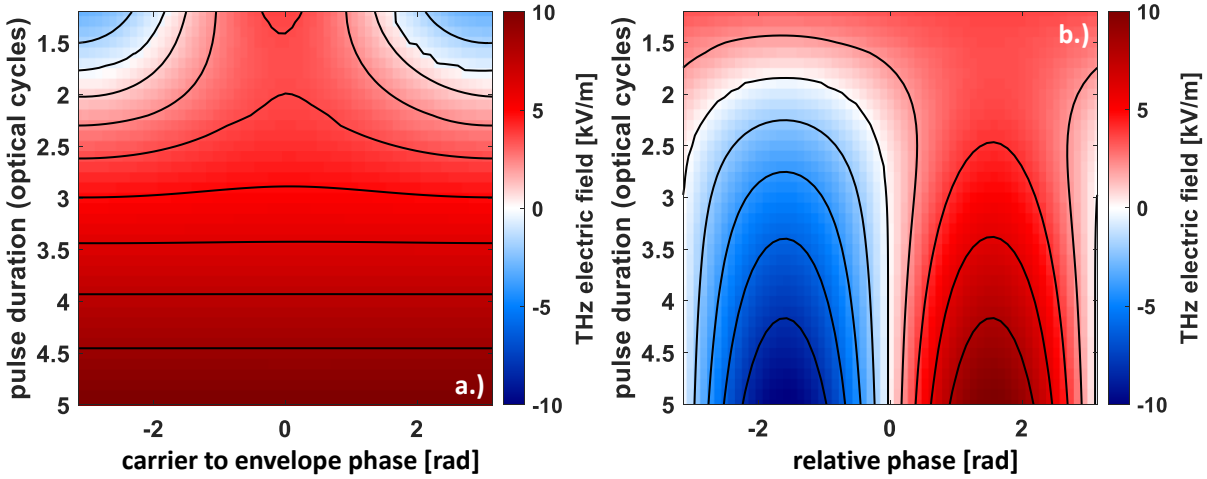

Figure 3.23: The peak electric field of the THz pulse as a function of pulse duration and a.) the CEP and b.) the RP. The central wavelength of the driving laser pulse is 3.2 μm and the polarization angle is 20°.

I also depicted only the effect of the RP and of pulse duration on THz pulse generation, while the CEP was constant, as shown in *Figure 3.23.b*. As one can see, as pulse duration decreases,

the significance of the RP decreases. The sensitivity of THz pulse generation to the RP is *2.00*, *2.00*, *1.95*, and *1.23* at *5*, *4*, *3*, and *2* optical cycles, respectively.

3.6.2. The effect of phase on THz pulse generation as a function of the polarization angle

Subsequently, I repeated the simulations with different polarization angles (*10°, 15°*, *20°*, *25°*, and *30°*). The results were similar in all cases, as shown in *Figure 3.23.* I determined the THz_{min} and THz_{max} values as a function of pulse duration and polarization angle. The results for the first case, when the CEP changed and the RP was constant, are shown in *Figure 3.24.a*. The THz_{min} values are depicted with dashed lines, while the THz_{max} values are depicted with straight lines. The different colors correspond to different polarization angles. As one can see, while the pulse duration is long (*>4.0* optical cycles), there is no noticeable difference between the THz_{min} and THz_{max} values. While the pulse duration is moderate (*~3.0* optical cycles), there is a noticeable, but not significant difference between the THz_{min} and THz_{max} values. While the pulse duration is short (*<2.0* optical cycles), there is a significant difference between them. It is clearly visible from these results, that the importance of the CEP in relation to THz pulse generation increases, while pulse duration decreases.

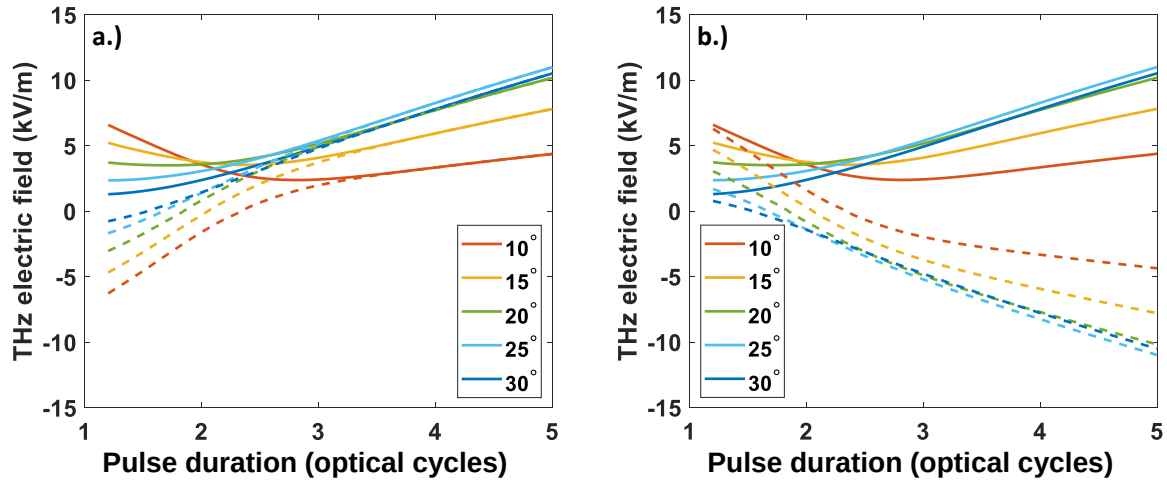

Figure 3.24: The THz_{min} (dashed lines) and the THz_{max} (straight lines) values as a function of pulse duration in case of different polarization angles. a.) The CEP changed, while the RP was constant. b.) The RP changed, while the CEP was constant. The different colors correspond to different polarization angles. The carrier wavelength of the driving laser pulse is 3.2 μm.

The results for the second case, when the RP changed and the CEP was constant, are shown in *Figure 3.24.b*. Here, the THz_{min} values are also depicted with dashed lines, while the THz_{max} values are depicted with straight lines. The different colors correspond to the same polarization angles as before. As one can see, while the pulse duration is long (*>4.0* optical cycles), there is a significant difference between the THz_{min} and THz_{max} values. They have the same absolute values, but they have the opposite signs. As long as pulse duration is moderate (*~3.0* optical cycles),

there is a visible difference between the THz_{min} and THz_{max} values. They do not have the same absolute values, but they still have the opposite signs. While pulse duration is short (*<2.0* optical cycles), there is a noticeable, but insignificant difference between them. They do not have the same absolute values and they do not have opposite signs any more. It is clearly visible from these results, that the importance of the RP decreases, while pulse duration decreases.

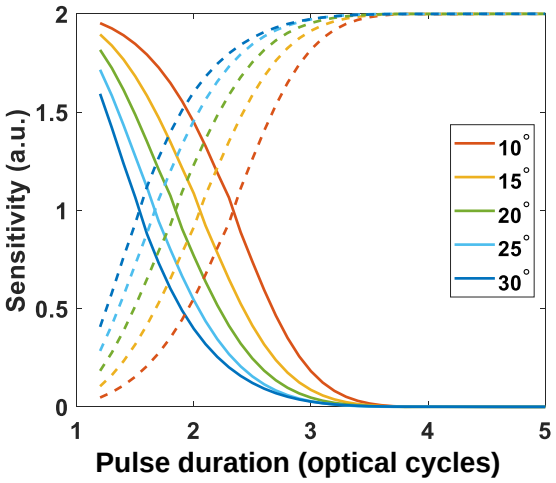

Figure 3.25: The sensitivity of the CEP (straight lines) and the RP (dashed lines) as a function of pulse duration in case of different polarization angles. The central wavelength of the driving laser pulse is 3.2 μm.

I calculated the sensitivity (*Equation 3.1.*) of THz pulse generation to the CEP and RP based on the previous results. The sensitivity of THz pulse generation to the CEP (straight lines) and to the RP (dashed lines) as a function of pulse duration in case of different polarization angles is shown in *Figure 3.25*. The different colors correspond to the same polarization angles as before. As one can see, sensitivity to the RP decreases, while pulse duration decreases. On the other hand, sensitivity to the CEP acts the opposite way: it increases while pulse duration decreases. It is important to note that the shape of the curves slightly depends on the polarization angle. I must also define the switching point, which is the pulse duration where the two sensitivities are equal. As one can see, it clearly depends on the polarization angle. The switching point is around *2.3*, *2.1*, *1.9*, *1.7*, and *1.6* optical cycles at *10°*, *15°*, *20°*, *25°*, and *30°* polarization angles, respectively. I think the reason behind this phenomenon lies in SHG itself. As the polarization angle decreases, the efficiency of SHG also decreases with it, which reduces the importance of the RP. This, in turn, shifts the position of the switching point to longer pulse durations. Based on these results, a CEP measurement technique can be developed using THz pulse generation with few optical cycle MIR pulses, where the measurement and the control of the CEP is of paramount interest.

3.6.3.Discussion

I investigated the CEP and the RP effect on THz pulse generation as a function of pulse duration (*1.2-5.0* optical cycles) and as a function of the polarization angle (*10°*, *15°*, *20°*, *25°*, and *30°*).

The central wavelength was at *3.2 μm*. I found that the sensitivity of THz pulse generation to CEP increases, while the sensitivity to the RP decreases with decreasing pulse duration. The same tendency could be observed in case of different polarization angles. As the pulse duration gets shorter, THz pulse generation moves away from the conventional scheme to the unconventional scheme (see *Chapter 3.5.*). This increases the sensitivity of THz pulse generation on the CEP, while its sensitivity to the RP decreases with decreasing pulse duration. As the pulse duration decreases, the necessity of SHG also decreases, which also reduces the effect of the RP. As pulse duration increases, the number of individual optical cycles grows. This reduces the difference between them, which also reduces the impact of the CEP. The switching point, where the sensitivity of THz pulse generation to the CEP and RP are equal, slightly depends on the polarization angle. More specifically, when the polarization angle decreases, the switching point shifts to longer pulse durations. I think the reason behind this phenomenon lies in SHG itself. As the polarization angle decreases, the efficiency of SHG generation also decreases, which reduces the importance of the RP. Consequently, the position of the switching point switches to longer pulse durations. Based on these results, it becomes possible to develop a CEP measurement technique based on THz pulse generation with few optical cycle MIR pulses. My corresponding thesis point to these new scientific results is the following:

T.6: I investigated the carrier to envelope and the relative phases effect on terahertz pulse generation as a function of pulse duration and polarization angle. As the pulse duration gets shorter, terahertz pulse generations moves away from the conventional to the unconventional scheme. That is why the sensitivity of the terahertz pulse generation to the carrier to envelope phase increases, while sensitivity to the relative phase decreases with decreasing pulse duration. As the pulse duration decreases, the need for the second harmonic pulse also decreases, which also reduces the effect of the relative phase. As the pulse duration increases, the number of individual optical cycles increases, which reduces the difference between them, and consequently diminishes the impact of the carrier to envelope phase. Furthermore, I also investigated the effect of the polarization angle of the fundamental pulse on these sensitivities. I found that the switching point, the point where the two sensitivities are equal, increases with a decreasing polarization angle. As the polarization angle decreases, the efficiency of second harmonic generation also decreases, which reduces the importance of the relative phase. This, in turn, increases the position of the switching point. [79]

“So long and thanks for all the fish”

Douglas Adams

4. Summary

My thesis presents a series of studies in the topic of few optical cycle pulse generation in the MIR and THz spectral domains. One of the current trends in ultrashort pulse development is to move towards the MIR spectral domain. The advantage of a longer carrier wavelength is the ponderomotive potential, which scales quadratically with the carrier wavelength. Consequently, secondary light sources pumped with longer carrier wavelengths result in higher cut-off photon energies for HHG and produce higher intensities for THz pulse generation.

The peak power of the pulses can be augmented by increasing their energy or/and by decreasing their duration. Both techniques have advantages and disadvantages. During the preparation of my dissertation, I focused on the latter method. Pulse duration can be reduced to the few optical cycle regime, where CEP is significant, so we need to carefully measure and control this parameter during experiments. This requires the accumulation of a large amount of data, e.g. during HHG and THz generation. A few optical cycle pulse duration can be achieved, for instance, by SPM in bulk solid-state media followed by recompression. To reach the shortest possible pulse duration, the derivatives of the spectral phase must be compensated. In the few optical cycle regime, not only the GDD, but also the TOD and higher order derivatives must be minimized. A possible solution to this challenge is to use DMs with an arbitrary spectral phase, for example a negative TOD. These mirrors can be characterized with the help of the SH-SRI, which measures the spectral phase information in the MIR spectral domain and converts it to the NIR spectral domain, where spectrometers with higher spectral resolution are more commonly available. During my research activities, I developed the SH-SRI method and characterized the DMs which were specifically developed for the postcompression of the MIR laser system at ELI ALPS Research Institute. I also further developed the postcompression stage of the same system using the formerly characterized DMs, and reduced pulse duration to less than two optical cycles.

Terahertz radiation belongs to the LWIR and FIR spectral domains. The THz pulse generation scheme, which is the subject of my research activities, is two-color ionization in gas. This method results in broadband THz pulse generation, which is a useful tool for THz-TDS. The physical source of THz radiation is the TEC developed inside plasma. The important requirement for this method is the application of an asymmetric driving electric field. The two most straightforward ways to achieve this are either with the use of few optical cycle or two-color pulses. Several scientific studies have already shown that the efficiency of this scheme increases with the carrier wavelength of the fundamental pulse due to the ponderomotive potential. In my dissertation, I numerically investigated THz pulse generation as a function of the carrier wavelength of the driving laser pulse. I also examined several windows to control the RP between the two-color pulses during THz pulse generation. Continuing my previous research, I numerically examined the effects of pulse duration, the polarization angle, the CEP and the RP of the fundamental pulse on

THz pulse generation. I performed the experimental work and the numerical simulations for my dissertation at ELI ALPS Research Institute and at the University of Szeged, Department of Optics and Quantum Electronics. I summarize my scientific results in the following six thesis points:

T.1: I developed a spectrally resolved interferometer assisted by second harmonic generation. Thanks to this innovation, I was able to overcome the limited spectral resolution of commercially available spectrometers in the mid infrared spectral domain. I achieved this by transferring the spectral phase information in the near infrared spectral domain, where commercial spectrometers with higher spectral resolution are more common. I verified the newly developed second harmonic assisted spectrally resolved interferometer with materials with well-known spectral phase. I also compared it with the conventional spectrally resolved interferometer in terms of root mean square deviation and standard deviation, and it was found to perform better in both terms. Using this technique, I was able to measure the group delay spectrum of the newly manufactured dispersive mirror pair designed for postcompression in the mid infrared spectral domain, and I found good agreement with the designed value. [36]

T.2: I used the dispersive mirror pair characterized in the first thesis point and developed the postcompression stage of the mid infrared laser system at ELI ALPS Research Institute. I tested several available materials for self-phase modulation. Barium fluoride, potassium bromide, and silicon were found to be best in terms of transmission and spectral broadening. I also tested different combinations of these materials, and the barium fluoride and silicon pair was found to have the highest potential peak power. I was able to compress the pulse almost down to the Fourier transform limit with the help a calcium fluoride window and three dispersive mirrors. I managed to shorten the pulse duration, which was originally five optical cycles (*~50 fs)* to less than two optical cycles (*~20 fs*) during postcompression. During my work, another aim was to increase the peak intensity of the system. Here I achieved a *30.3%* increment. [36]

T.3: I investigated the possibility of using the mid infrared system at ELI ALPS Research Institute to generate terahertz pulses in nitrogen plasma with two-color pulses. With numerical simulation I investigated the efficiency improvement in terahertz pulse generation with mid and longwave infrared two-color pulses compared to near infrared two-color pulses with the same input pulse parameters. I investigated the spectral domain from *2.15 μm* to *15.15 μm* and tested different thicknesses of the nonlinear crystal. I found that the scaling law of the terahertz pulse generation increases with increasing nonlinear crystal thickness. From this I concluded that terahertz pulse generation is very sensitive to second harmonic generation. Furthermore, I investigated the scaling law with different cutoff frequencies and found that it slowly increases with decreasing cutoff frequency. From this I concluded that the lower frequency part of the terahertz spectrum is more sensitive to the driving wavelength. Finally, I found that terahertz radiation generated with mid infrared (*3.3 μm*) and longwave infrared (*7.3 μm*) is by one and two orders of magnitude more intense than the terahertz radiation generated with near infrared (*0.8 μm*) two-color pulses. [30]

T.4: I investigated the relative phase tuning ability of thin dielectric plates with mid infrared, two-color pulses during terahertz pulse generation in nitrogen plasma. My aim was to

determine which material is best suited for fine-tuning the relative phase between the two-color pulses, and thus also for optimizing the peak intensity of the terahertz pulse. I investigated terahertz pulse generation with several materials, transparent in the mid infrared spectral domain. I also simulated the terahertz pulse generation with different material thicknesses and angles of incidence. I found that the best candidates are different fluorides, especially lithium and calcium fluoride. These materials have negative group velocity dispersion, and thanks to this they are not just able to control the relative phase between the two-color pulses but also improve the temporal overlap between them, which further increases the efficiency of terahertz pulse generation. [30]

T.5: I investigated terahertz pulse generation in nitrogen plasma as a function of pulse duration and polarization angle. I identified three distinctly different regions, where the optimal pulse parameters for the most efficient terahertz pulse generation are different. The first or conventional region is where the two-color pulse scheme is dominant above *3.2* optical cycles (*34.1 fs* at *3.2* μm). The second or unconventional region is, where the one-color pulse scheme is dominant below *1.7* optical cycles (*18.1 fs* at *3.2* μm). The last or semi-conventional/transitional region is, where the two-color pulse scheme is still dominant, but the sign of the relative phase is also determinative. In the conventional region, two-color pulses with opposing relative phases generate terahertz pulses with the same absolute peak power, but this is not true in the transitional region. In addition, I found that the lower boundary of the conventional region increases with increasing central wavelength, while the upper boundary of the unconventional region decreases with increasing central wavelength. [79]

T.6: I investigated the carrier to envelope and the relative phases effect on terahertz pulse generation as a function of pulse duration and polarization angle. As the pulse duration gets shorter, terahertz pulse generations moves away from the conventional to the unconventional scheme. That is why the sensitivity of the terahertz pulse generation to the carrier to envelope phase increases, while sensitivity to the relative phase decreases with decreasing pulse duration. As the pulse duration decreases, the need for the second harmonic pulse also decreases, which also reduces the effect of the relative phase. As the pulse duration increases, the number of individual optical cycles increases, which reduces the difference between them, and consequently diminishes the impact of the carrier to envelope phase. Furthermore, I also investigated the effect of the polarization angle of the fundamental pulse on these sensitivities. I found that the switching point, the point where the two sensitivities are equal, increases with a decreasing polarization angle. As the polarization angle decreases, the efficiency of second harmonic generation also decreases, which reduces the importance of the relative phase. This, in turn, increases the position of the switching point. [79]

„Viszlát, és kösz a halakat!”

Douglas Adams

5. Magyar nyelvű összefoglaló

5.1. Bevezetés

A nemlineáris optika története 1931-ben indult el, amikor doktori értékezésében Maria Goeppert Mayer elsőként írta le a kétfotonos abszorpció elméletét. A tudományos közösségnek mégis további harminc évig kellett várnia az első kísérleti eredményekig, amelyekhez egy tudományos áttörésre volt szükség. T. H. Maiman 1960-ban építette meg az első működő lézert (light amplification by stimulated emission of radiation – LASER), ami a kísérleti nemlineáris optika nélkülözhetetlen előfeltétele volt. Ezután felgyorsultak az események, 1961-ben a nemlineáris optikában rögtön két kísérleti eredmény is született: W. Kaiser a kétfotonos abszorpció, P. A. Franken pedig a frekvenciakétszerezés jelenségét igazolta kísérletileg.

A néhány optikai ciklusos impulzusok fejlesztésének egyik jelenlegi iránya a közép infravörös (mid infrared – MIR) spektrális tartományban működő rendszerek fejlesztése. A hosszabb központi hullámhossz egyik előnye a ponderomotoros erő, ami a hullámhossz négyzetével arányos. Ennek hatásaként, a hosszabb központi hullámhosszon működő rendszerekkel gerjesztett másodlagos források például nagyobb levágási fotonenergiát biztosítanak a magasharmonikus-keltés során vagy nagyobb intenzitást eredményeznek terahertzes (THz) impulzus generálásakor. Egy további törekvés a magasabb csúcsintenzitás elérése, amihez vagy az impulzus energiáját kell növelni és/vagy az impulzus hosszát kell csökkenteni. A doktori dolgozatomban az utóbbi lehetőséggel foglalkoztam behatóbban.

A THz-es sugárzás a távoli infravörös (far infrared – FIR) spektrális tartomány része. Amellett, hogy a THz-es sugárzás természetes háttérsugárzásként körülvesz minket a mindennapokban, számos módszer létezik az előállítására is. A disszertációm tárgyát képező módszer a gázok kétszínű impulzussal történő ionizációján alapul. E módszerrel spektrálisan széles sávú THz-es impulzusok állíthatók elő, amelyek többek között a THz-es időtartományú spektroszkópiában használhatók fel. E módszernél a sugárzás forrása a plazmában létrehozott transzverzális elektronáram. Fontos előfeltétel, hogy a módszer során aszimmetrikus elektromos mezőt kell alkalmazni, ami a szabad elektronokot hatékonyabban gyorsítja az egyik irányban, mint a másikban, és ezzel transzverzális elektronáramot hoz létre a plazmán belül. A szükséges aszimmetria néhány ciklusos és/vagy kétszínű impulzusokkal hozható létre. Doktori dolgozatomban mindkét lehetőséget tanulmányoztam. Továbbá megvizsgáltam a központi hullámhossz, az impulzushossz, a polarizációs szög, a vivő-burkoló fázis (carrier to envelope phase – CEP) és a relatív fázis (relative phase – RP) THz-es impulzuskeltésre gyakorolt hatásait.

A disszertációm kísérleti és szimulációs eredményeit az ELI ALPS Kutatóintézetben és a Szegedi Tudományegyetem Optika és Kvantumelektronika Tanszékén végeztem.

5.2. Tudományos előzmények

Az elektromágneses spektrumban különböző spektrális tartományokat különböztethetünk meg a fotonok fizikai, kémiai és biológiai hatásai alapján. A dolgozatomban az infravörös (infrared – IR) sugárzással foglalkozom részletesebben, ami a 0,7 µm és 1000 µm közötti hullámhossztartományban található. Ezt további öt tartományra szokás bontani, a közeli IR (near infrared – NIR), a rövidhullámú IR (shortwave infrared – SWIR), a MIR, a hosszúhullámú IR (longwave infrared – LWIR) és a FIR. A számos alkalmazási terület közül az egyik az IR spektroszkópia. Ez egy nemionizáló anyagvizsgálati módszer, amellyel mennyiségi és minőségi vizsgálatok végezhetők roncsolásmentesen, például a NIR fotonok a különböző vibrációs állapotok közötti átmenetek tanulmányozásához alkalmazhatók. THz-es fotonokkal molekuláris ujjlenyomatokat lehet vizsgálni, amelyekkel azonosíthatók a különböző gyógyszerek, kábítószerek és robbanószerek. Emellett a legtöbb csomagolóanyag, például a papír is, átlátszó ezen a spektrális tartományon, ezért a THz-es sugárzásnak biztonsági szempontból is kiemelten fontos szerepe van.

Akkor beszélhetünk lineáris optikáról, amikor a polarizáció (P) és az elektromos térerősség (E) között lineáris kapcsolat van. Amikor azonban az E értéke megközelíti vagy meghaladja az 5.14×10^{11} V/m-et, akkor már nem elhanyagolható a P másodrendű tagja, ami az E^2-vel lesz arányos. Hasonlóan, amikor az E értéke megközelíti vagy meghaladja a $2{,}64 \times 10^{23}$ V/m-ot, akkor a P harmadrendű tagját is figyelembe kell már venni, ami az E^3-vel lesz arányos. A másodrendű folyamatok közé tartozik, a frekvenciakétszerezés (second harmonic generation – SHG), az összegfrekvencia-keltés (sum frequency generation – SFG), a különbségifrekvencia-keltés (difference frequency generation – DFG) és az optikai egyenirányítás (optical rectification – OR). Az SHG során két azonos frekvenciájú fotonból ($\omega_1 = \omega_2$) keletkezik egy harmadik foton ($\omega_3 = 2 \times \omega_1$), aminek a frekvenciája kétszer akkora, mint az eredeti fotonoké. Az SFG során két különböző frekvenciájú fotonból ($\omega_1 > \omega_2$) keletkezik egy harmadik foton ($\omega_3 = \omega_1 + \omega_2$), aminek a frekvenciája megegyezik az eredeti fotonok frekvenciáinak összegével. Az SHG az SFG elfajult eseteként is kezelhető, ahol a kezdeti fotonok frekvenciája azonos. A DFG során két különböző frekvenciájú fotonból ($\omega_1 > \omega_2$) keletkezik három további foton (ω_2, ω_2 és ω_3), ahol az egyik foton frekvenciája az eredeti fotonok frekvenciáinak a különbségével egyenlő ($\omega_3 = \omega_1 - \omega_2$). Az OR során két azonos frekvenciájú fotonból ($\omega_1 = \omega_2$) keletkezik egy statikus elektromos mező ($\omega_3 = \omega_1 - \omega_1 = 0$). Az OR a DFG elfajult eseteként is kezelhető, ahol a kezdeti fotonok frekvenciája azonos. E folyamatokból általában csak az egyik eléggé intenzív ahhoz, hogy számottevő mennyiségű fotont generáljon. Azt, hogy melyik lesz ez a folyamat, az energia- ($\hbar\omega_3 = \hbar\omega_2 + \hbar\omega_1$) és az impulzusmegmaradás ($\hbar/k_3 = \hbar/k_2 + \hbar/k_1$) törvényei határozzák meg. A harmadrendű folyamatok közé tartozik a frekvencia háromszorozás (third harmonic generation – THG) és a négyhullámkeverés (four wave mixing – FWM). A THG során három azonos frekvenciájú fotonból ($\omega_1 = \omega_2 = \omega_3$) keletkezik egy negyedik foton ($\omega_4 = 3 \times \omega_1$), amelynek a frekvenciája háromszor akkora, mint az eredeti fotonok frekvenciájáé. Itt érdemes még megemlíteni a nemlineáris törésmutatót is, ami a harmadrendű folyamatok eredménye. A törésmutató általánosan felírható egy lineáris (n_0) és egy nemlineáris (n_2) tag összegeként, ahol az előbbi tag konstans, míg az utóbbi tag lineárisan függ az intenzitástól. A nemlineáris törésmutató

felel az önfókuszálás és az önfázis moduláció (self-phase modulation – SPM) jelenségeiért. Az FWM során három fotonból ($\omega_1 \geq \omega_2 \geq \omega_3$) keletkezik egy negyedik foton, ami a három foton keverésének az eredménye ($\omega_4 = \pm \omega_1 \pm \omega_2 \pm \omega_3$). Ezt szintén az energia- és impulzusmegmaradás törvényei határozzák meg.

A kísérletekhez az ELI ALPS Kutatóintézetben található MIR optikai parametrikus csörpölt impulzusú erősítő (optical parametric chirped pulse amplification – OPCPA) rendszert használtam. (A THz-es impulzuskeltés numerikus szimulációja során ugyanezen rendszer paramétereit vettem alapul.) A rendszer alapja egy Yb-YAG (itterbium – ittrium alumínium gránát) alapú regeneratív, korongerősítő lézer, ami a rendszer OPCPA részét hajtja meg. Az Yb-YAG impulzus központi hullámhossza *1030 nm*, aminek egy részével filamentációt keltenek egy YAG kristályban, ami által az spektrálisan kiszélesedik. A következő fokozatban az Yb-YAG impulzus egy újabb része és a korábban már spektrálisan kiszélesedett impulzus (*1300 – 1900 nm*) között DFG-t keltenek, aminek a központi hullámhossza *3200 nm* lesz. A következő három fokozatban ezt a hullámhossz komponenst erősítik tovább az YAG pumpa lézerrel. A MIR OPCPA rendszer végén az impulzus energiája *145 μJ*, az impulzusidő *35,5 fs*, ami kevesebb, mint négy optikai ciklus ezen a hullámhosszon.

A THz-es sugárzás az IR és a mikrohullámú spektrális tartományok között található és *„THz-es hézag”* néven is ismert. A kifejezés onnan származik, hogy a múltban nehézkes volt előállítani ezt a fajta sugárzást. Az elektronikai és az optikai módszereknek már túlságosan rövid (magas), illetve túlságosan hosszú (alacsony) volt ez a hullámhossz- (frekvencia-) tartomány, ezért sokáig egy hézag volt az optikai és elektronikai hullámok között. A kétszínű impulzussal történő gázionizáció a THz-es impulzusok előállításának egyik aktívan kutatott módszere napjainkban. E módszernél a sugárzás forrása a plazmában kialakult transzverzális elektronáram. Ennek egyik fontos előfeltétele, hogy az alkalmazott elektromos mező aszimmetrikus legyen, vagyis az egyik irányba hatékonyabban gyorsítsa a szabad elektronokat, mint a másikba. Ennek hatására a plazmában kialakul egy transzverzális elektronáram. Az aszimmetrikus elektromos mező előállítható néhány ciklusos és/vagy kétszínű impulzusok alkalmazásával. Az előbbi esetben a CEP, míg az utóbbi esetben az RP hangolásával lehet az aszimmetriát hangolni. A kétszínű impulzusokat általában úgy állítják elő, hogy SHG-t alkalmaznak, ami után a két impulzust nem választják szét, hanem együttesen alkalmazzák. A közelmúltban publikált tanulmányok bizonyították, hogy a THz-es impulzuskeltés hatékonysága növelhető a központi hullámhossz növelésével. Ennek egyik oka a ponderomotoros erő, ami a központi hullámhossz négyzetével arányos. A másik oka a kisebb csoportsebesség különbség a kétszínű impulzuson belül, ami növeli az impulzusok időbeli átfedését, ez pedig javítja a THz-es impulzusok keltésének hatékonyságát.

Az optikai elemek spektrális fázistolása többféleképpen is mérhető. Az egyik legelterjedtebb technika a spektrálisan bontott interferometria (spectrally resolved interferometry – SRI), ami egy egyszerű, lineáris és nagy pontosságú módszer. A mérések során egy kétkarú interferométert használnak, ami lehet Mach-Zehnder vagy Michelson típusú elrendezés is. Az interferométert egy spektrálisan szélessávú fényforrással világítják meg, amit egy nyalábosztó segítségével szétosztanak a két kar között oly módon, hogy az egyesítés után a spektrális interferencia láthatósága maximális legyen. Az egyik karban található a minta, a másik kart referenciaként

használják. A két karban a spektrális fázis nem azonos ($\phi_m \neq \phi_r$), emiatt az egyesítés után spektrális interferencia tapasztalható a spektrumban, amiből meghatározható a két kar közötti fáziskülönbség ($\Delta\phi = \phi_m - \phi_r$). A referencia ismert spektrális fázisából és a mért fáziskülönbségből meghatározható a minta spektrális fázisa. Az egyik legelterjedtebb kiértékelési módszer a Fourier-transzformáción (FT) alapul. A módszer során először nullára kell normálni a felvett spektrális interferenciát, majd gyököt kell belőle vonni, mivel a FT az elektromos tereken alkalmazható, de a kísérletek során az intenzitás az, amit mérni tudunk. Utána következhet az inverz FT, ami után általában három csúcsot kapunk az időtartományban abban az esetben, ha két nyaláb közötti interferenciáról van szó. Az egyik csúcs a $t = 0$ időpontnál lesz található, a másik két csúcs a $t = \pm\tau$ időpontoknál, ahol τ a minta és a referenciakarok közötti optikai úthossz különbségnek felel meg. A $+\tau$ időpontnál található csúcsot kivágjuk, majd következhet a FT, amiből már gyorsan és egyszerűen meghatározható a spektrális fáziskülönbség a karok között.

5.3. Tudományos eredmények

5.3.1. Frekvenciakétszerezéssel segített spektrálisan bontott interferometria

Az első tézispontomban az SHG-vel segített SRI-t (SH-SRI) mutatom be. A kísérleti elrendezés fényforrása az ELI ALPS Kutatóintézetben található MIR-OPCPA rendszer volt. Az elrendezés alapja egy Mach-Zehnder interferométer. A nyalábosztást és kombinálást egy-egy kalcium-fluorid nyalábosztóval végeztem el, amelyeket úgy helyeztem el, hogy a minta és a referenciakar közötti spektrális fáziskülönbség minimális legyen. A hagyományos SRI mérések során egy MIR spektrométert használtam, amelyet a kísérleti elrendezés végén helyeztem el. AZ SH-SRI mérések során először az egyesített nyalábbal kellett SHG-t kelteni, amit egy ezüst-gallium-diszulfid kristály segítségével végeztem el, majd a SHG nyaláb spektrumát egy NIR optikai spektrum analizátorral mértem meg.

A módszer hitelesítése során megmértem több, jól ismert anyag (bárium-fluorid, kalcium-fluorid, tallium bróm-jódid, szilícium és YAG) csoportkésés (group delay – GD) spektrumát a hagyományos SRI és az SH-SRI módszerekkel is. A kapott eredményeket összehasonlítottam egymással és az irodalmi értékekkel is, amelyeket az anyagok törésmutatója alapján határoztam meg. Összehasonlítási alapul azért választottam a GD spektrumot, mert ilyenkor az eredmények között csak egy konstans különbség lehetséges, ami egyszerűsítette az összehasonlítás menetét. Az SH-SRI mérések mindegyik esetben pontosabban illeszkedtek az irodalmi értékekhez és a mérések szórása is kisebb volt. További érdekesség, hogy az SH-SRI mérések esetén látható volt egy csúcs a GD spektrumban *3250 nm*-nél, ami a hagyományos SRI mérésekkel nem volt kimutatható. A csúcs nagysága arányos volt az interferométer karjai közötti úthosszkülönbséggel, amiből arra a következtetésre jutottam, hogy a levegő egyik összetevője okozza. A HITRAN (high-resolution transmission molecular absorption database – nagyfelbontású transzmissziós molekuláris abszorpció adatbázis) alapján megállapítottam, hogy a jelenséget a levegőben található metán okozhatja, ami további bizonyíték a módszer érzékenységére.

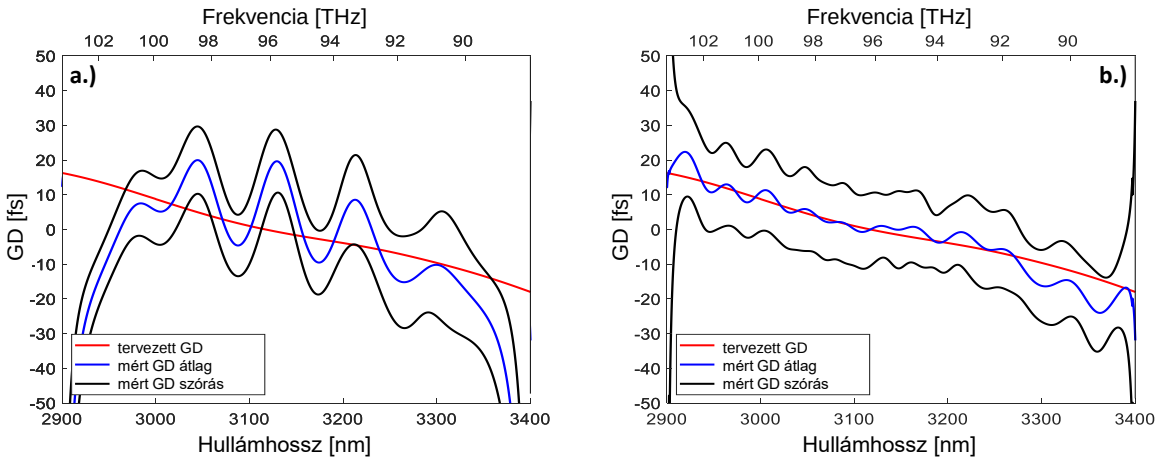

5.1 ábra: A DM pár (10° és 20°-os beesési szög) GD spektruma a.) a hagyományos SRI-vel és b.) az SH-SRI-val mérve.

Az SH-SRI módszer sikeres hitelesítése után megmértem az egyedi gyártású diszperziós tükrök (dispersive mirror – DM) GD spektrumát is. Ezeket a DM-eket a MIR spektrális tartományban működő rendszerek posztkompressziójához tervezte és gyártotta az OPTOMAN, azonban a gyártás utáni minőségellenőrzésre nem volt lehetőségük. A hagyományos SRI-vel és az SH-SRI-vel mért GD spektrum az 5.1 ábrán látható. A tervezett és a mért GD spektrum piros, illetve kék színnel látható. Az SH-SRI módszerrel mért GD spektrum alapján a DM csoportkésés diszperziója (group delay dispersion – GDD) *274 fs*^{2}, míg harmadrendű diszperziója (third order dispersion – TOD) *–7204 fs*^{3} volt. A DM tervezett GDD-je *270 fs*^{2}, TOD-ja *–7000 fs*^{3}, amit az SH-SRI mérési módszerrel sikerült hitelesíteni. A kapcsolódó tézispontom a következő:

> **T.1:** Kifejlesztettem egy frekvenciakétszerezéssel segített, spektrálisan bontott interferométert. Ennek az új innovációnak köszönhetően képes voltam felülemelkedni a középinfravörös spektrális tartományban elérhető spektrométerek limitált spektrális felbontásán. Ezt úgy értem el, hogy a spektrális fázisinformációt átvittem a közeli infravörös spektrális tartományba, ahol a kereskedelemben kapható spektrométerek spektrális felbontása jobb. A módszert olyan anyagokkal hitelesítettem, amelyek spektrális fázisa jól ismert a középinfravörös tartományon. Összehasonlítottam a hagyományos és a frekvenciakétszerezéssel segített spektrálisan bontott interferometriát. Az utóbbi esetben az átlagos négyzetes eltérés és a standard deviáció is jobb volt. Az új módszer segítségével meg tudtam mérni a középinfravörös spektrális tartományon történő posztkompresszióhoz újonnan kifejlesztett diszperziós tükrök csoportkésés spektrumát. A tervezett és a mért értékek jól egyezést mutattak. [36]

5.3.2. A MIR-OPCPA rendszer posztkompressziója

Ebben a tézispontomban az ELI ALPS Kutatóintézetben található MIR OPCPA rendszer posztkompresszióját mutatom be. Az impulzusukat egy *–1000 mm* görbületi sugarú arany tükör segítségével fókuszáltam levegőben. A vizsgált ablakokat a fókusz után helyeztem el normál

beesésben. A nyalábot egy *250 mm* effektív fókusztávolságú kalcium-fluorid lencsével kollimáltam, ami után megmértem az impulzusok energiáját, spektrumát és a CEP stabilitást.

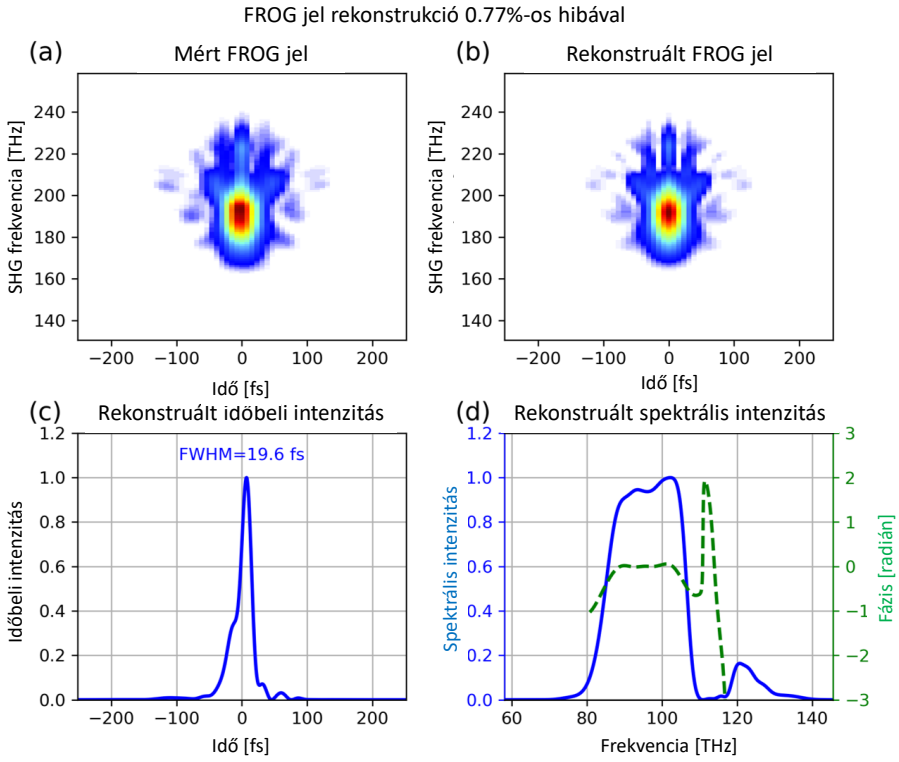

5.2 ábra: Az impulzusidő mérése a FROG mérőeszközzel. a.) a mért FROG jel, b.) a rekonstruált FROG jel, c.) a rekonstruált időbeli alak és d.) a rekonstruált spektrális intenzitás és fázis.

Minden rendelkezésemre álló anyagot (bárium-fluorid, kalcium-fluorid, gallium-arzénid, kálium-bromid, tallium bróm-jodid, magnézium-fluorid, szilícium, YAG, cink-szulfid és cink-szelenid) megvizsgáltam. Mindegyik esetben megmértem az átlagteljesítményt és a spektrális kiszélesedést, amiből meghatároztam a várható csúcsintenzitás értékét. A legígéretesebb a bárium-fluorid, a kálium-bromid, a szilícium és ezek kombinációja volt. Általánosan elmondható, hogy a kétablakos elrendezéssel nagyobb spektrális szélesedést tudtam elérni, de a háromablakos elrendezés már nem javította jelentősen tovább az eredményt. Egy spektrális tartományon túl már a levegő abszorpciója is korlátoz, a víznek *2,6–2,7 μm*-nél, a széndioxidnak *4,2–4,3 μm*-nél találhatóak abszorpciós vonalai. A bárium-fluorid – kálium-bromid ablak pár esetén *16.9 fs*, a bárium-fluorid – szilícium ablak pár esetén *16,7 fs* és a kálium-bromid – szilícium ablak pár esetén *18,2 fs* a spektrum Fourier transzformációs korlátja. A kálium-bromid amellett, hogy higroszkopikus még a lézer okozta roncsolódásra is érzékenyebb volt, mint a másik két anyag, ezért a bárium-fluorid – szilícium ablak párral dolgoztam tovább.

Először a DM-ek nélkül, pusztán anyagi diszperziót felhasználva próbáltam kompresszálni az impulzust. A legjobb eredményt egy *2 mm* vastag kalcium-fluorid ablakkal értem el: ekkor az impulzus időbeli félértékszélessége (full width at half maximum – FWHM) *25.5 fs* volt, ami két és fél optikai ciklusnak feleltethető meg. Ezután az anyagi diszperzió mellett felhasználtam az

előző tézispontomban megvizsgált DM-eket is. Három DM és egy *5 mm* vastag kalcium-fluorid ablak segítségével az impulzus FWHM értékét *19,6 fs*-nak mértem, ami kevesebb, mint két optikai ciklusnak felel meg. Az impulzusidő mérést egy egyedileg fejlesztett, frekvenciabontott optikai kapuzáson (frequency resolved optical gating – FROG) alapuló mérőeszközzel végeztem el. Az utóbbi mérés az 5.2 ábrán látható. A posztkompresszió után az átlagteljesítmény *8,24 W* volt, ami *4,04 GW* csúcsteljesítménynek felel meg. A MIR-OPCPA rendszer kiindulási csúcsteljesítménye *3,10 GW* volt, amit több mint *30%*-kal sikerült javítani.

A rendszerstabilitást négy órán keresztül mértem. Az átlagteljesítmény stabilitása *2,1%*, a CEP érték szórása pedig *240 milliradián* volt. Összehasonlításképpen, a MIR-OPCPA rendszer átlagteljesítmény stabilitása *0,7%*, a CEP érték szórása *65 milliradián*. Ezek az értékek elfogadható kompromisszumok, ha figyelembe vesszük a megrövidült impulzusidőt és a megnövekedett csúcsteljesítményt. A spektrum Fourier-transzformációs korlátja kevesebb, mint *1 fs*-ot változott a mérés időtartama alatt. Ez a fejlesztés a rendszert rendkívül vonzóvá teszi jövőbeli felhasználói kísérletekhez. A kapcsolódó tézispontom a következő:

> **T.2:** Az előző tézispontban megvizsgált diszperziós tükröket felhasználva megépítettem az ELI ALPS Kutatóintézet középinfravörös rendszerének posztkompressziós fokozatát. Több elérhető anyag önfázis-modulációját megvizsgálva a transzmisszió és a spektrális szélesedés tekintetében a bárium-fluoridot, a kálium-bromidot és a szilíciumot találtam a legígéretesebbnek. Ezen anyagok különböző kombinációinak vizsgálata alapján megállapítottam, hogy a bárium-fluorid és szilícium pár nyújtja a legjobb potenciális csúcsteljesítményt. Három diszperziós tükör és egy kalcium-fluorid ablak segítségével közel a Fourier-transzformációs korlátig tudtam kompresszálni az impulzust. Az eredetileg öt optikai ciklusnyi (*~50 fs*) impulzust sikerült két optikai ciklus (*~20 fs*) hosszúságúra rövidíteni a posztkompresszió során. Munkám során egy másik cél a csúcsintenzitás növelése volt, ahol *30,3%-os* növekedést értem el. [36]

5.3.3. A központi hullámhossz hatása a THz-es impulzuskeltésre

Ebben a tézispontomban numerikus szimuláció segítségével megvizsgáltam a központi hullámhossz hatását a THz-es impulzuskeltésre. A modellezés során használt impulzus paramétereinek alapjául az ELI ALPS Kutatóintézetben található MIR OPCPA rendszert választottam. A vizsgált spektrális tartomány *2,15 μm* és *15,15 μm* között volt, amit a SHG-hoz használt nemlineáris gallium-szelenid kristály határozott meg. Az impulzusok csúcsteljesítménye (*2,5 GW*) és az impulzushossz (négy optikai ciklus) állandó volt a szimulációim során. Több kristályvastagságot (*10 μm, 30 μm* és *100 μm*) is megvizsgáltam.

Először az SHG folyamatát tanulmányoztam a központi hullámhossz függvényében. Azt kaptam, hogy a kétszínű impulzus időbeli átfedése javul a központi hullámhossz növelésével. A gallium-szelenid kristály reflexiós veszteségének minimuma *2,3 μm*-nél és *14,3 μm*-nél van, ahol a fázisillesztés által meghatározott beesési szög megegyezik a Brewster szöggel. E spektrális tartományon túl a reflexiós veszteség gyorsan növekszik egészen *2,15 μm*-ig és *15,15 μm*-ig, ahol a fázisillesztés szöge már eléri a teljes visszaverődés szögét és a kristály további SHG keltésre nem használható. A következő lépésben az alagúteffektuson alapuló ionizációt vizsgáltam meg.

Az alagúteffektus jellemzően azokban az időpillanatokban megy végbe, amikor az elektromos tér a legintenzívebb. Ezért az ionizáció nem folytonos, hanem lépcsőzetes, ahol a lépcsők az elektromos téren belüli optikai ciklusokat reprezentálják. Az elektronsűrűség maximuma *14,1 μm*-nél található.

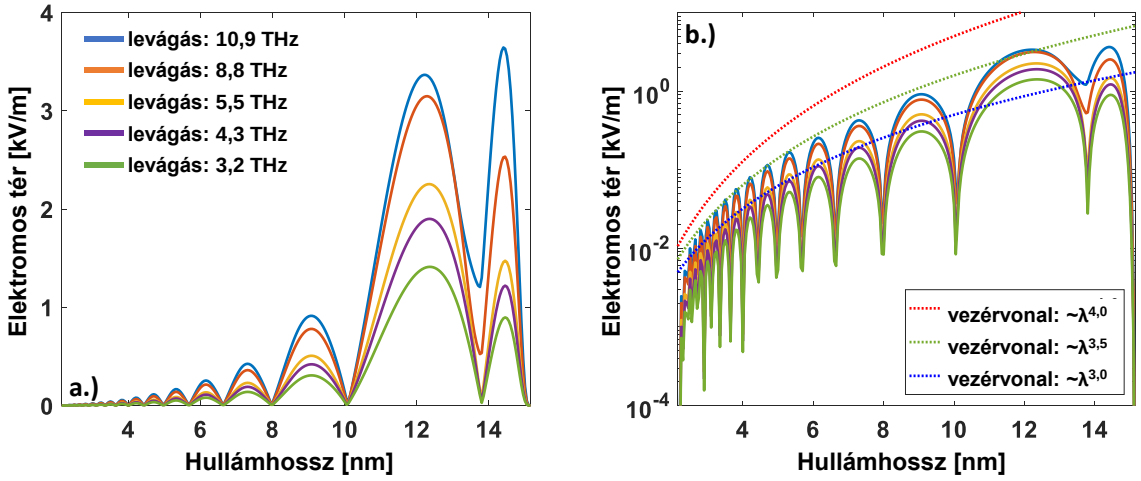

5.3 ábra: a.) A THz-es impulzus elektromos terének csúcsértéke a központi hullámhossz függvényében különböző aluláteresztő szűrők esetén. b.) Ugyanaz, mint a.), de féllogaritmikus skálán. Szemléltetés különböző skálázási törvényekkel.

Ezek után a THz-es impulzuskeltés folyamatát vizsgáltam meg. A *30 μm* vastag nemlineáris kristály esetén a globális maximum *12,3 μm*-nél van, de több lokális maximum is található például *9,1 μm*-nél, *7,3 μm*-nél, *6,2 μm*-nél és így tovább. Ennek oka, hogy a folyamat érzékeny az RP értékére, ami függ a kristályvastagságtól és a fázissebességtől, ami pedig a hullámhossz függvénye. Amikor az RP *±π/2 radián*, akkor maximumot kapunk, amikor *0 radián* vagy *±π radián*, akkor minimumot. Vastagabb kristály esetén sűrűbben jelentkeznek a lokális maximumok, mert gyorsabban változik az RP értéke, míg vékonyabb kristály esetén ritkábban jelentkeznek a lokális maximumok, mert lassabban változik az RP értéke.

Amikor a központi hullámhossz a MIR vagy a LWIR spektrális tartományban van, akkor a spektrális szűrés különösen fontos. Nem megfelelően megválasztott aluláteresztő szűrő esetén a keltő impulzus egy része is áthatolhat a szűrőn, ami interferenciát okozhat a detektálás során. A skálázási törvényt különböző aluláteresztő szűrőkre is megvizsgáltam; az eredmények az 5.3 ábrán láthatók. A levágási frekvencia csökkentésével nő a skálázási törvény, ami arra utal, hogy a rövidebb hullámhosszok érzékenyebbek a központi hullámhosszra. Vastagabb kristály esetén nagyobb, míg vékonyabb kristály esetén kisebb értékeket kaptam a skálázási törvényre. Ezek alapján megállapítható, hogy a skálázási törvény érzékeny az SHG keltés folyamatára, amit a kristály vastagsága befolyásol.

Végezetül összehasonlítottam a Ti: zafír, a MIR és a LWIR OPCPA rendszereket a THz-es impulzuskeltés szempontjából. A Ti: zafír rendszerek központi hullámhossza jellemzően *0,8 μm*. Ezen a hullámhosszon béta-bárium-borát (beta barium borate – BBO) kristályt használnak SHG

keltésre. Az impulzus csúcsteljesítménye és időbeli hossza azonos volt a korábbi értékekkel. A kapott eredmények fényében a MIR rendszerekkel keltett THz-es impulzus egy, míg az LWIR rendszerekkel keltett THz-es impulzus két nagyságrenddel intenzívebb, mint a Ti: zafír rendszerek esetén. A kapcsolódó tézispontom a következő:

> **T.3:** Megvizsgáltam az ELI ALPS Kutatóintézetben található középinfravörös rendszer felhasználását terahertzes impulzusok keltésére, kétszínű impulzussal ionizált nitrogén plazmában. Numerikus szimuláción keresztül megvizsgáltam, hogy mennyivel hatékonyabb a folyamat közép- és hosszúhullámú infravörös-impulzusokkal a közeli infravöröshöz képest. A vizsgált spektrális tartomány *2,15 μm* és *15,15 μm* között volt, továbbá megvizsgáltam a különböző nemlineáris kristályvastagságokat is. Azt tapasztaltam, hogy a skálázási törvény a kristály vastagságával növekszik. Ebből arra a következtetésére jutottam, hogy a terahertzes impulzuskeltés nagyon érzékeny a frekvenciakétszerezés folyamatára. A skálázási törvényt különböző aluláteresztő szűrők esetén is tanulmányoztam, és azt tapasztaltam, hogy az a levágási frekvencia függvényében csökken. Ebből arra következtettem, hogy az alacsonyabb frekvenciakomponensek érzékenyebbek a központi hullámhosszra. Végezetül, a középinfravörössel (*3,3 μm*) egy, míg a hosszúhullámú infravörössel (*7,3 μm*) két nagyságrenddel intenzívebb a keltett THz-es impulzus, mint a közeli infravörös (*0,8 μm*) esetén. [30]

5.3.4. Relatív fázisszabályozás a THz-es impulzuskeltéshez

Ebben a tézispontomban numerikus szimuláció segítségével megvizsgáltam az RP szabályozásának lehetőségét a THz-es impulzuskeltéshez használt kétszínű impulzuson belül. A MIR és az LWIR spektrális tartományban a csoport- és a fázissebesség közötti különbség a kétszínű impulzusok esetén csekély, ezért szükséges a precíz és pontos RP szabályozás. Az SHG keltés után az RP értékét a nemlineáris kristály vastagsága és törésmutatója fogja meghatározni. Egy általános megoldás, hogy a kétszínű impulzust hagyják a levegőben terjedni, aminek a diszperziója lassan hangolja az RP-t. A NIR spektrális tartományon ez mindössze néhány centiméteres, azonban a MIR és az LWIR spektrális tartományon akár több méteres terjedést is jelenthet. Ez a megoldás azért sem praktikus, mert e spektrális tartományokban a levegőnek több jelentős abszorpciós vonala is van. Egy másik módszernél a kétszínű nyalábot egy dikroikus tükör segítségével szétválasztják majd a megfelelő úthossz-különbség után egyesítik. Egy harmadik lehetőség, hogy levegő helyett egy üvegablakot vagy egy ékpárt helyezünk a kétszínű impulzus fényútjába és ennek segítségével szabályozzuk az RP-t.

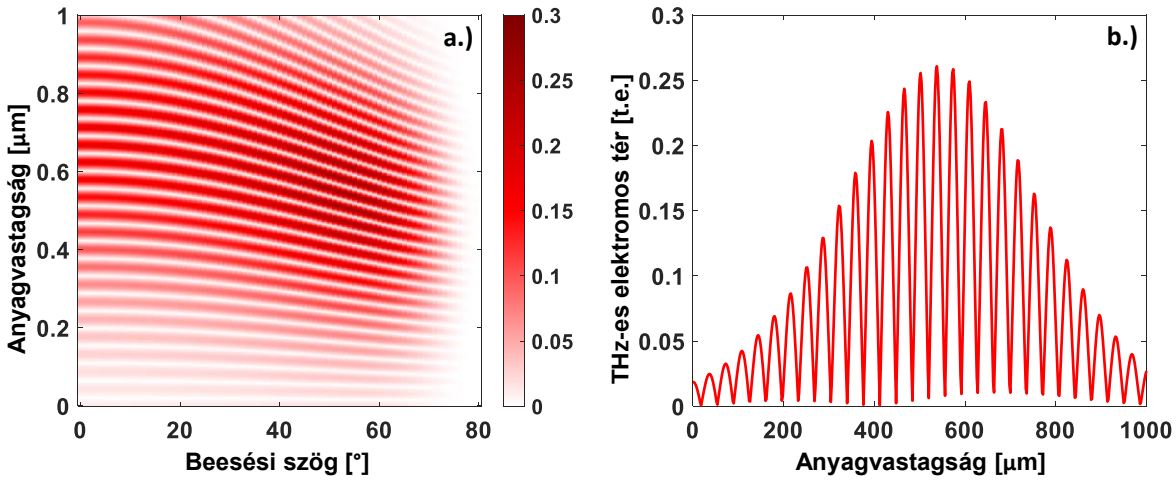

5.4 ábra: a.) A THz-es impulzus maximális elektromos tere a lítium-fluorid ablak vastagsága és a beesési szög függvényében. b.) A THz-es impulzus maximális elektromos tere a lítium-fluorid ablak vastagságának függvényében az optimális beesési szögnél (55°).

Több olyan anyag is rendelkezésünkre áll, amely átlátszó a MIR és az LWIR spektrális tartományokban. A munkám során három fontos kritériumot fektettem le: A kiválasztott anyagok 1.) legyenek kereskedelmi forgalomban kaphatók, 2.) ne legyenek kettősen törők, 3.) csoportsebesség diszperziójuk (group velocity dispersion – GVD) negatív legyen. Ez utóbbi azért fontos, mert kompenzálni tudja a használt gallium-szelenid kristály pozitív előjelű GVD-jét, és ezáltal tovább javítható a THz-es impulzuskeltés hatékonysága. A három vizsgált anyag a bárium-fluorid, a kalcium-fluorid és a lítium-fluorid volt; amelyek mind teljesítik a fenti három kritériumot. Az RP szabályozás a lítium-fluorid ablak vastagságának és a beesési szög függvényében az 5.4 ábrán látható. A beesési szög függvényében először egy lassú növekedés tapasztalható a THz-es impulzus maximális elektromos terében a Brewster szögig, majd egy gyors csökkenés következik. Az ablakvastagság függvényében egyszerre figyelhető meg egy gyors és egy lassú változás. A lassú változás annak tudható be, hogy az ablak GVD-jének negatív előjele miatt eleinte javul az időbeli átfedés a kétszínű impulzuson belül, ami miatt a THz-es impulzuskeltés is javul. A gyors változás pedig annak, hogy az RP értéke folyamatosan változik: ahol maximumot látunk, ott az RP értéke $\pm\pi/2$ *radián*, ahol minimumot látunk, ott az RP értéke *0 radián* vagy $\pm\pi$ *radián*. Az optimális ablakvastagság *0,5 mm* az optimális beesési szög pedig *55°* lítium-fluorid esetén. Bárium-fluorid esetén ezek az értékek *4,7 mm* és *56°*, kalcium-fluorid esetén pedig *1,45 mm* és *55°*. Mindhárom anyag képes az RP szabályozására, de a kalcium- és a lítium-fluorid esetén kaptam a legintenzívebb THz-es impulzusokat. A kapcsolódó tézispontom a következő:

T.4: Megvizsgáltam a relatív fázisszabályozás lehetőségét vékony dielektrikum ablakok használatával terahertzes impulzuskeltés közben. A célom az volt, hogy meghatározzam mely anyagok a legalkalmasabbak a relatív fázis finomhangolására és ezáltal a terahertzes impulzus intenzitásának optimalizálásra. Több, a közép infravörös tartományban átlátszó anyagot is megvizsgáltam numerikus szimuláció segítségével. Különböző ablakvastagságok és beesési

szögek mellett szimuláltam a terahertzes impulzuskeltést. Az eredményeim alapján a legjobb jelöltek a különböző fluoridok, például a lítium- és a kalcium-fluorid. Ezeknek az anyagoknak a csoportsebesség diszperziója negatív előjelű, amelynek köszönhetően a relatív fázis finomhangolása mellett az időbeli átfedés is javul a kétszínű impulzuson belül, amivel tovább nő a terahertzes impulzuskeltés hatékonysága is. [30]

5.3.5. Az impulzushossz hatása a THz-es impulzuskeltésre

Ebben a tézispontomban numerikus szimuláció segítségével megvizsgáltam, hogy az impulzushossz és a polarizációs szög milyen hatással van a THz-es impulzuskeltésre. A vizsgált impulzushossz tartomány *1,2* és *5,0* optikai ciklus között volt. A vizsgált polarizációs szögtartomány *0°* és *50°* között volt, ahol *0°* a tisztán extraordinárius polarizáció és *90°* a tisztán ordinárius polarizáció. Az impulzus csúcsintenzitása (*2,5 GW*) állandó volt a szimuláció során. A nemlineáris kristály egy *10 μm* vastag gallium-szelenid volt.

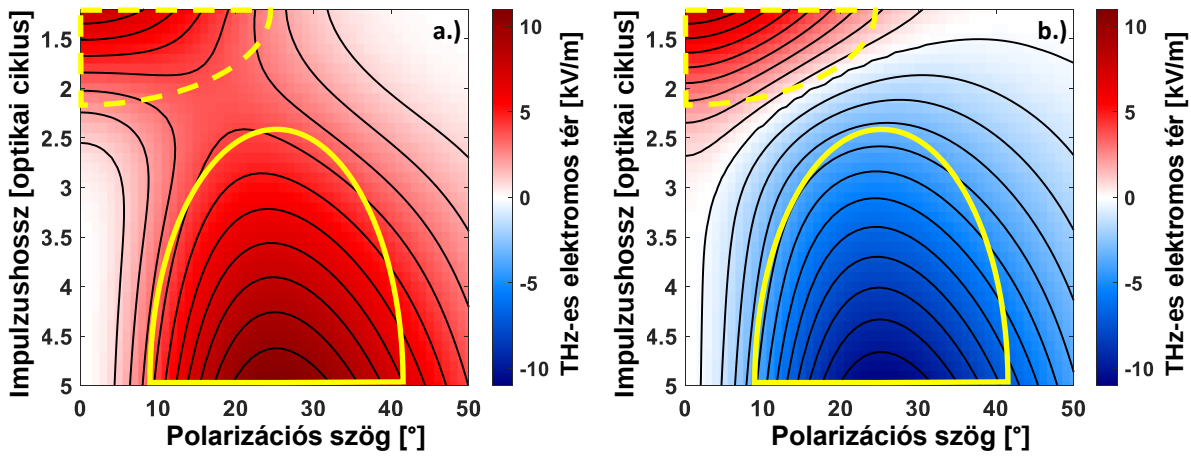

5.5 ábra: A THz-es impulzus elektromos terének maximuma az is impulzushossz és a polarizációs szög függvényében, amikor az RP a.) +π/2 radián és b.) –π/2 radián. A keltő impulzus központi hullámhossza 3,2 μm.

A keltő impulzus központi hullámhossza *3,2 μm* volt, ezen a hullámhosszon egy optikai ciklus *10,7 fs* hosszú. A numerikus szimuláció eredménye az 5.5 ábrán látható, amikor az RP *+π/2 radián* (5.5.a.)) és *–2/π radián* (5.5.b.)). A *+π/2 radián* RP esetén két olyan tartomány figyelhető meg, ahol intenzív a THz-es impulzuskeltés. Az első a hagyományos tartomány, ahol a kétszínű impulzuskeltés a domináns, ez az ábra alsó-középső részén figyelhető meg (folytonos sárga vonallal kiemelve). Az optimális impulzushossz és polarizációs szög ebben az esetben *5,0* optikai ciklus és *25°*. A másik a rendhagyó tartomány, ahol az egyszínű impulzuskeltés a domináns, ez az ábra bal felső részén figyelhető meg (szaggatott sárga vonallal kiemelve). Az optimális impulzushossz és polarizációs szög ebben az esetben *1,2* optikai ciklus és *0°*. Emlékeztetésül, amikor a polarizációs szög *0°*, akkor a keltő impulzus tisztán extraordinárius és ilyenkor nem történik SHG keltés a nemlineáris kristályban. Ez azt jelenti, hogy ebben az esetben a nemlineáris kristály elhagyható az elrendezésből. A *–π/2 radián* RP esetén is ugyanaz a két tartomány

figyelhető meg, ahol intenzív a THz-es impulzuskeltés. Ebben az esetben a hagyományos tartományon a THz-es impulzus elektromos tere előjelet vált, a rendhagyó tartományon azonban nem. Ennek az az oka, hogy a kétszínű impulzussal keltett THz-es impulzus érzékeny az RP-re, míg az egyszínű impulzussal keltett nem, hiszen ott nem is értelmezhető ez a mennyiség. A két tartomány között megfigyelhető egy átmeneti tartomány is, ahol továbbra is a kétszínű impulzuskeltés a domináns, de a folyamat már érzékeny az RP előjelére is. A hagyományos tartományon az ellentétes előjelű RP-vel keltett THz-es impulzusok szintén előjelet váltanak, de az abszolút értékük azonos marad, viszont az átmeneti tartományban ez már nem igaz.

A következő lépésben egy hasonló vizsgálatot végeztem el, miközben a keltő impulzus központi hullámhosszát *2,5 μm* és *4,0 μm* között változtattam. Az előbbi esetben egy optikai ciklus *8,3 fs*, míg az utóbbi esetben *13,3 fs* hosszú. Azt tapasztaltam, hogy a rendhagyó tartomány felső korlátja *1,9* optikai ciklus (*15,9 fs*), amikor a központi hullámhossz *2,5 μm* és *1,6* optikai ciklus (*21,3 fs*), amikor a központi hullámhossz *4,0 μm*. Továbbá a hagyományos tartomány alsó korlátja *3,2* optikai ciklus (*26,7 fs*), amikor a központi hullámhossz *2,5 μm* és *3,5* optikai ciklus (*46,7 fs*), amikor a központi hullámhossz *4,0 μm*. Amint az látható, a rendhagyó tartomány felső korlátja csökken, a hagyományos tartomány alsó korlátja pedig nő a növekvő központi hullámhossznál. Az előbbi eset valószínűleg annak köszönhető, hogy a központi hullámhossz növelésével javul az SHG keltés hatékonysága, illetve a kétszínű impulzus időbeli átfedése is. Mindkettő pozitív hatással van a THz-es impulzuskeltésre és ezért érthető, miért csökken a rendhagyó tartomány felső korlátja. Az utóbbi eset valószínűleg annak köszönhető, hogy a központi hullámhossz növelésével nő a ponderomotoros erő is. A kapcsolódó tézispontom a következő:

> **T.5:** Megvizsgáltam a terahertzes impulzuskeltést a keltő impulzus hosszának és polarizációjának függvényében. Három tartományt definiáltam, ahol a terahertzes impulzuskeltés optimális impulzusparaméterei eltérőek. Az első tartomány a hagyományos tartomány, ahol a kétszínű impulzuskeltés domináns *3,2* optikai ciklus felett (*34,1 fs 3,2 μm*-nél). A második tartomány a rendhagyó tartomány, ahol az egyszínű impulzuskeltés domináns *1,7* optikai ciklus alatt (*18,1 fs 3,2 μm*-nál). Az utolsó tartomány az átmeneti tartomány, ahol továbbra is a kétszínű impulzuskeltés a domináns, de a relatív fázis előjele is meghatározó már. A hagyományos tartományban a kétszínű impulzusok ellentétes előjelű relatív fázissal ellentétes előjelű, de azonos abszolút értékű terahertzes impulzust keltenek, de ez az átmeneti tartományban már nem igaz. Azt is megfigyeltem, hogy a hagyományos tartomány alsó korlátja csökken, a rendhagyó tartomány felső korlátja pedig nő a növekvő központi hullámhossznál. [79]

5.3.6. A fázisok hatása a THz-es impulzuskeltésre

Ebben a tézispontban numerikus szimuláció segítségével vizsgáltam meg a CEP és az RP értékének hatását a THz-es impulzuskeltésre. A központi hullámhossz ebben az esetben is *3,2 μm* volt. A vizsgált impulzushossz tartomány *1,2* és *5,0* optikai ciklus közé esett, a vizsgált polarizációs tartomány *10°*, *15°*, *20°*, *25°* és *30°* volt. Emlékeztetőként, a *0°* a tisztán extraordinárius polarizáció és a 90° a tisztán ordinárius polarizáció. Az impulzus csúcsintenzitása (*2,5 GW*) állandó volt a szimuláció során.

Megvizsgáltam a THz-es impulzuskeltést a CEP és az RP függvényében, állandó polarizációs szög (*20°*) mellett, miközben változtattam az impulzus hosszát. Azt tapasztaltam, hogy az impulzushossz rövidülésével nő a CEP hatása és ezzel párhuzamosan csökken az RP hatása. Az előbbi jelenség oka, hogy az egymást követő optikai ciklusok között egyre látványosabb lesz a különbség, ami miatt növekszik a CEP hatása. Az utóbbi jelenség hátterében az áll, hogy a THz-es impulzuskeltés a hagyományos, kétszínű tartományból átvált a rendhagyó, egyszínű tartományba, ami miatt csökken a RP hatása.

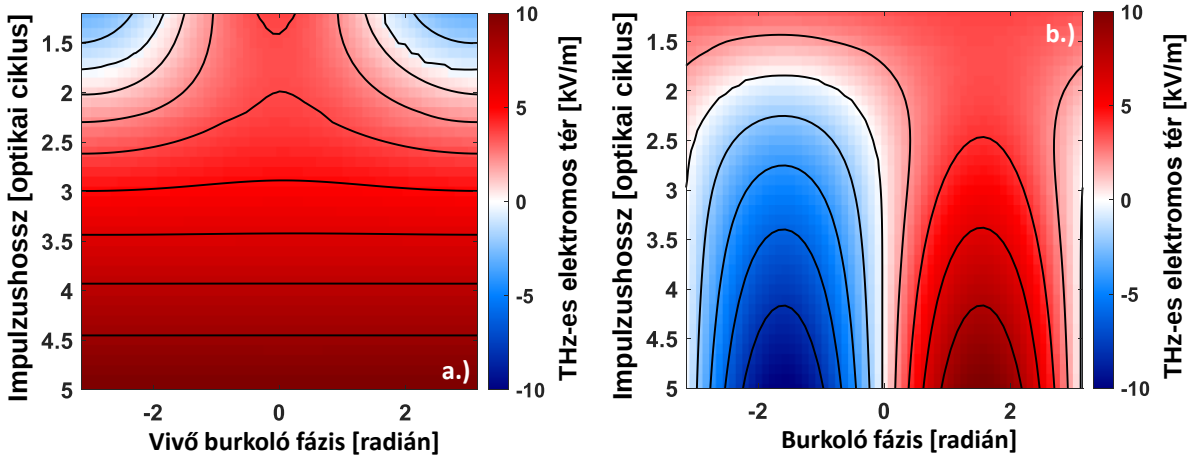

5.6 ábra: A THz-es impulzus elektromos terének maximális értéke az impulzushossz és a.) a CEP és b.) az RP függvényében. A központi hullámhossz 3,2 μm és a polarizációs szög 20°.

Az átláthatóbb szemléltetés érdekében a következőben az egyik fázis értékekét állandó értéken tartottam, miközben változtattam a másik fázis értékét és az impulzus hosszát; ez látható az 5.6 ábrán. Egyértelműen látható, hogy amikor a CEP változik és az RP állandó (5.6.a), akkor a hatás az impulzushossz csökkenésével növekszik. Amikor az RP változik és a CEP állandó (5.6.b), akkor egyértelműen látható, hogy az impulzus rövidülésével csökken a hatás. A következőkben azt vizsgáltam, hogyan változik a THz-es impulzuskeltés, ha más a polarizációs szög. A vizsgált polarizációs szögek a következők voltak: *10°*, *15°*, *20°*, *25°* és *30°*. Először a CEP értékének hatását vizsgáltam meg, miközben az RP értéke állandó volt. Amikor az impulzus hosszú (*~4,0* optikai ciklus), akkor a maximum és a minimum értékek között nincs észrevehető különbség. Amikor az impulzus közepes (*~3,0* optikai ciklus), akkor a maximum és a minimum értékek között van észrevehető különbség. Amikor az impulzus rövid (*~2,0* optikai ciklus), akkor a maximum és a minimum értékek között jelentős különbség van. Ezek alapján egyértelműen látható, hogy a CEP hatása az impulzushossz csökkenésével nő. Másodszor az RP értékének a hatását vizsgáltam meg, miközben a CEP értéke állandó volt. Amikor az impulzus hosszú (*~4,0* optikai ciklus), akkor a maximum és a minimum értékek között jelentős különbség van, az abszolút értékek nagysága azonos és az előjelek ellentétesek. Amikor az impulzus közepes (*~3,0* optikai ciklus), akkor a maximum és a minimum értékek között észrevehető a különbség, az abszolút értékek nagysága már nem azonos, de az előjelek továbbra is ellentétesek. Amikor az impulzus rövid (*~2,0* optikai ciklus), akkor a maximum és a minimum értékek között a különbség tovább csökken, az abszolút értékek nagysága nem azonos és az előjelek sem

ellentétesek már. Ezek alapján egyértelműen látható, hogy az RP hatása az impulzushossz csökkenésével gyengül.

Az előbbi eredmények alapján megvizsgáltam a THz-es impulzuskeltés érzékenységét a két fázis függvényében. Definiáltam a váltási pontot, ami az az impulzushossz, ahol a két fázis érzékenysége azonos, és azt tapasztaltam, hogy ez a pont érzékeny a polarizációs szögre. A váltási pont *2,3, 2,1, 1,9, 1,7* és *1,6* optikai ciklusnál volt *10°, 15°, 20°, 25°* és *30°* polarizációs szög esetén. Úgy gondolom, hogy a jelenség hatterében az SHG áll. A polarizációs szög csökkenésével romlik a nemlineáris folyamat hatékonysága és ezzel párhuzamosan az RP hatása is, ami miatt a nagyobb impulzushosszok felé tolódik el a váltási pont. Ezen eredményeim alapján a néhány optikai ciklusból álló impulzusokkal keltett THz-es impulzus alkalmas lehet a CEP fázis mérésére.

T.6: Megvizsgáltam a vivő-burkoló fázis és a relatív fázis hatását a terahertzes impulzuskeltésre. Az impulzushossz csökkenésével a terahertzes impulzuskeltés a hagyományos tartományból átvált a rendhagyó tartományba. Ezért a vivő-burkoló fázis hatása a terahertzes impulzuskeltésre nő, míg a relatív fázisé csökken. Az impulzus rövidülésével csökken a frekvenciakétszerezés szükségessége, és ezáltal gyengül a relatív fázis hatása is. Az impulzushossz növekedésével az egymást követő optikai ciklusok közötti különbség csökken, ami miatt a vivő-burkoló fázis hatása is csökken. Megvizsgáltam a polarizációs szög hatását is. Azt tapasztaltam, hogy a váltási pont, azaz a pont, ahol a két fázis érzékenysége egyenlő, a csökkenő impulzus hosszával növekszik. A polarizációs szög csökkenésével romlik a frekvenciakétszerezés hatékonysága, ami csökkenti a relatív fázis hatását, ez pedig felfelé tolja a váltási pont helyzetét. [79]

6. Acknowledgement

At most importantly, I would like to thank my family for their support in the past years, they have always encouraged me whenever I felt lost.

Also, I want to thank my supervisors, Ádám Börzsönyi PhD and Viktor Chikán PhD for the opportunity and all their help. It was a long and exhaustng journey and they were by my side the whole time. I am indescribably grateful to all my former and current colleagues. Thank you for the time we spent together and the endless amount of coffee we drank together. However, I would like to thank some people in particular.

First of all, I owe special thanks to Bálint Kiss PhD, who helped me already during my MSc years. He later became my group leader and helped me even more. I learned a lot from him about MIR OPCPA systems and he honored me by appointing me as his deputy.

I am very grateful to Máté András Kurucz PhD, with whom we struggled all the way to the PhD. We complemented each other very well in the course of our work and that teamwork made our drems come true.

Without a doubt, I am very thankful to Tímea Tímár-Grósz PhD, from whom I learned a lot about SRI. Also, with her sharp eyes, she always found the spelling and grammar mistakes I made.

I owe special thanks to Szabolcs Tóth PhD, with whom we struggled all the way to the PhD. I learned a lot from him about MIR OPCPA systems and nonlinear optics. He was always open to professional coffee breaks.

I am also grateful to Roland Sándor Nagymihály PhD, from whom I learned a lot about the Ti:Sapphire systems. I could always confidently turn to him if I had questions, problems or ideas.

I would especially like to thank Máté Kovács. I learned a lot from him during my years as a student, and we share a lot of nice memories from those years.

My special thanks go to János Csontos PhD, Barnabás Gilicze PhD, Viktor Zuba, Bence Máté Kovács, Mercédesz Horváth and Zsolt Bengery, they always made time when I needed their company.

Last but not least, I would like to say thank you to my friends too.

The ELI ALPS project (GINOP-2.3.6-15-2015-00001) is supported by the European Union and co-financed by the European Regional Development Fund.

7. Own publications

7.1. Publications related to the thesis

[T1] R. Flender, A. Borzsonyi, V. Chikan, "Phase-controlled, second-harmonic-optimized terahertz pulse generation in nitrogen by infrared two-color laser pulses", Journal of the Optical Society of America B 37(6) 1838-1846 (2020)
DOI: https://doi.org/10.1364/JOSAB.391123

[T2] R. Flender, M. Kurucz, T. Grosz, A. Borzsonyi, U. Gimzevskis, A. Samalius, D. Hoff, B. Kiss, "Dispersive mirror characterization and application for mid-infrared postcompression", Journal of Optics 23(6), 065501 (2021)
DOI: https://doi.org/10.1088/2040-8986/abf88e

[T3] R. Flender, A. Borzsonyi, V. Chikan, "The role of asymmetry in few-cycle, mid-IR pulses during THz pulse generation", Journal of Optics 24(4), 045502 (2022)
DOI: https://doi.org/10.1088/2040-8986/ac5289

7.2. Further scientific publications

[F1] B. Kiss, R. Flender, Cs. Vass, "Fabrication of micro- and submicrometer period metal reflection gratings by melt-imprint technique", Journal of Laser Micro/Nanoengineering 8(3), 287-291 (2013)
DOI: https://doi.org/10.2961/jlmn.2013.03.0016

[F2] C. Vass, B. Kiss, R. Flender, Z. Felhazi, P. Lorenz, M. Erhardt, K. Zimmer, "Comparative study on grating fabrication in transparent materials by TWIN-LIBWE and ultrashort pulsed ablation techniques", Journal of Laser Micro/Nanoengineering 10(1), 38-42 (2015)
DOI: https://doi.org/10.2961/jlmn.2015.01.0008

[F3] B. Kiss, R. Flender, J. Kopniczky, F. Ujhelyi, Cs. Vass, "Fabrication of polarizer by metal evaporation of fused silica surface relief gratings", Journal of Laser Micro/Nanoengineering 10(1) 53-58 (2015)
DOI: https://doi.org/10.2961/jlmn.2015.01.0011

[F4] R. Flender, K. Sarosi, A. Borzsonyi, V. Chikan, "The impact of dispersion of ultrashort light pulses on the THz radiation formation from asymmetric air plasmas", Proceedings of SPIE 10228, 102281B (2017)
DOI: https://doi.org/10.1117/12.2265663

[F5] R. S. Nagymihaly, H. Cao, P. Jojart, M. Kalashnikov, A. Borzsonyi, V. Chvykov, R. Flender, M. Kovacs, K. Osvay, "Carrier-envelope phase stability of a polarization-encoded chirped pulse Ti:Sapphire amplifier", Journal of the Optical Society of America B 35(1), A1-A5 (2018)
DOI: https://doi.org/10.1364/JOSAB.35.0000A1

[F6] R. Flender, K. Sarosi, E. Petracs, A. Borzsonyi, V. Chikan, “Controlling terahertz spectrum in asymmetric air plasmas: The role of GDD and phase”, Proceedings of SPIE 10684, 1068428 (2018)
DOI: https://doi.org/10.1117/12.2307411

[F7] R. S. Nagymihaly, H. Cao, P. Jojart, V. Zuba, R. Flender, O. Antipov, I. Seres, A. Borzsonyi, V. Chvykov, K. Osvay, M. Kalashnikov “Broadband spectral characterization of the phase shift induced by population inversion in Ti:Sapphire”, Optics Express 27(2), 1226-1235 (2019)
DOI: https://doi.org/10.1364/OE.27.001226

[F8] R. Flender, K. Sarosi, E. Petracs, A. Borzsonyi, V. Chikan, “Control of THz field waveform emitted from air plasma by chirping two-color laser pulses”, Optics Communications 436, 222-226 (2019)
DOI: https://doi.org/10.1016/j.optcom.2018.12.020

[F9] M. Kurucz, Sz. Toth, R. Flender, L. Haizer, B. Kiss, B. Persielle, E. Cormier, “Single-shot CEP drift measurement at arbitrary repetition rate based on dispersive Fourier transform”, Optics Express 27(9), 13387-13399 (2019)
DOI: https://doi.org/10.1364/OE.27.013387

[F10] A. Andrasik, R. Flender, J. Budai, T. Szorenyi, B. Hopp, “Single-shot surface ablation and transient reflectivity changes of optical glasses induced by 34 fs laser pulses”, Proceedings of SPIE 11034, 110340T (2019)
DOI: https://doi.org/10.1117/12.2523006

[F11] R. Flender, A. Borzsonyi, V. Chikan, “Theoretical investigation of terahertz generation from two-color laser pulse ionized gases: the role of the thickness of the nonlinear crystal”, Proceedings of SPIE 11026, 110260I (2019)
DOI: https://doi.org/10.1117/12.2520406

[F11] R. Flender, B. Kiss, A. Borzsonyi, V. Chikan, “THz generation from mid-infrared two-color laser pulses in air and a simple method for controlling the THz intensity”, Proceedings of SPIE 11026, 1102611 (2019)
DOI: https://doi.org/10.1117/12.2520408

[F13] Sz. Toth, R. Flender, B. Kiss, M. Kurucz, A. Andrianov, L. Haizer, E. Cormier, K. Osvay, “Comparative study of an ultrafast, CEP-stable dual-channel mid-IR OPCPA system”, Journal of the Optical Society of America B 36(12) 3538-3546 (2019)
DOI: https://doi.org/10.1364/JOSAB.36.003538

[F14] A. Andrasik, R. Flender, J. Budai, T. Szorenyi, B. Hopp, “Time integrated transient reflectivity vs. ablation characteristics of Borofloat, BK7 and B270 optical glasses ablated by 34 fs pulses”, Optical Material Express 10(2) 549-560 (2020)
DOI: https://doi.org/10.1364/OME.380294

[F15] R. Hollinger, D. Hoff, P. Wustelt, S. Skruszewicz, Y. Zhang, H. Kang, D. Würzler, T. Jungnickel, M. Dumergue, A. Nayak, R. Flender, L. Haizer, M. Kurucz, B. Kiss, S. Kühn,

E. Cormier, C. Spielmann, G. G. Paulus, P. Tzallas, M. Kübel, “Carrier-envelope-phase measurement of few-cycle mid-infrared laser pulses using High Harmonic Generation in ZnO”, Optics Express 28(5) 7314-7322 (2020)
DOI: https://doi.org/10.1364/OE.383484

[F16] M. Kurucz, R. Flender, L. Haizer, R. S. Nagymihaly, W. Cho, K. T. Kim, S. Toth, E. Cormier, B. Kiss, “2.3-cycle mid-infrared pulses from hybrid thin-plate postcompression at 7 W average power”, Optics Communication 472 126035 (2020)
DOI: https://doi.org/10.1016/j.optcom.2020.126035

[F17] Y. Deng, Z. Zeng, P. Komm, Y. Zheng, W. Helml, X. Xie, Z. Filus, M. Dumergue, R. Flender, M. Kurucz, L. Haizer, B. Kiss, S. Kahaly, R. Li, G. Marcus, “Laser-induced inner-shell excitations through direct electron re-collision versus indirect collision”, Optics Express 28(16) 23251-23265 (2020)
DOI: https://doi.org/10.1364/OE.395927

[F18] A. Andrasik, R. Flender, J, Budai, T. Szorenyi, B. Hopp, “Processing of optical glasses by single, 34 fs pulses in the strong field ionization domain: ablation characteristics and crater morphology”, Applied Physics A 126 (12) 936 (2020)
DOI: https://doi.org/10.1007/s00339-020-04122-z

[F19] M. Kubel, P. Wustelt, Y. Zhang, S. Skruszewicz, D. Hoff, D. Wurzler, H. Kang, D. Zille, D. Adolph, A. M. Sayler, G. G. Paulus, M. Dumergue, A. Nayak, R. Flender, L. Haizer, M. Kurucz, B. Kiss, S. Kuhn, B. Fetic, D. B. Milosevic, “High-order phase-dependent asymmetry in the above-threshold ionization plateau”, Physical Review Letters 126, 113201 (2021)
DOI: https://doi.org/10.1103/PhysRevLett.126.113201

[F20] C. Medina, D. Schomas, N. Rendler, M. Debatin, L. Ben Ltaief, M. Dumergue, Z. Filus, B. Farkas, R. Flender, L. Haizer, B. Kiss, M. Kurucz, B. Major, S. Toth, F. Stienkemeier, R. Moshammer, T. Pfeifer, S. R. Krishnan, A. Heidenreich, M. Mudrich, “Single-shot electron imaging of dopant-induced nanoplasmas”, New Journal of Physics 23(5), 053011 (2021)
DOI: https://doi.org/10.1088/1367-2630/abf7f9

[F21] F. E. Haniel, H. Schroeder, S. Kahaly, A. Nayak, M. Dumergue, S. Mondal, Z. Filus, R. Flender, M. Kurucz, L. Haizer, B. Kiss, D. Charalambidis, M. F. Kling, P. Tzallas, B. Bergues, “Saturating Multiple Ionization in Intense Mid-Infrared Laser Fields”, New Journal of Physics 23(05), 053026 (2021)
DOI: https://doi.org/10.1088/1367-2630/abf583

[F22] T. Grosz, M. Kurucz, R. Flender, A. Borzsonyi, U. Gimzevskis, A. Samalius, D. Hoff, B. Kiss, "High-resolution MIR-spectrally resolved interferometry", Proceedings of SPIE 11770, 1177019 (2021)
DOI: https://doi.org/10.1117/12.2591756

[F23] M. Kurucz, R. Flender, T. Grosz, A. Borzsonyi, B. Kiss, "Simultaneous spectral phase shift characterization in two frequency bands", Optics Communications 500, 127332 (2021)
DOI: https://doi.org/10.1016/j.optcom.2021.127332

7.3. Conference oral presentations

[O1] Cs. Vass, R. Flender, B. Kiss, K. Osvay, "Time-resolved study on grating fabrication in transparent dielectrics", LPM 2014, Vilnius, Lithuania, 17-20. June 2014

[O2] Cs. Vass, B. Kiss, R. Flender, P. Lorenz, M. Erhardt, K. Zimmer, "Micro-structuring of fused silica nanosecond UV laser in TWIN-LIBWE arrangement versus ultrashort pulse ablation", LPM 2014, Vilnius, Lithuania, 17-20. June 2014

[O3] Cs. Vass, R. Flender, B. Kiss, K. Osvay, "Time-resolved study on periodic microstructure fabrication in polymers", COLA 2015, Cairns, Australia, 31 August - 4 September 2015

[O4] Flender R., Sarosi K., Petracs E. Borzsonyi A., Chikan V., "A másodharmonikus keltéshez használt nemlineáris kristály vastagságának hatása a kétszínű lézerrel levegőplazmában keltett THz-es impulzus intenzitására", Tavaszi Szél 2018, Győr, Hungary, 4-6. May 2018

[O5] Kurti V., Polanek R., Flender R., Borzsonyi A., "Lézeres filamentáció ionizáló hatásának onkoterápiás szempontból történő vizsgálata", Tavaszi Szél 2018, Győr, Hungary, 4-6 May

[O6] Zuba V., Nagymihaly R. S., Cao H., Jojart P., Flender R., Borzsonyi A., Chykov V., Osvay K., Kalashnikov M., "Populáció inverzió által indukált törésmutató változás titán-zafír kristályban", Tavaszi Szél 2018, Győr, Hungary, 4-6 May

[O7] R. S. Nagymihaly, H. Cao, V. Chvykov, P. Jojart, V. Zuba, R. Flender, O. Antipov, I. Seres, A. Borzsonyi, N. Khodakovskiy, K. Osvay, M. Kalashnikov, "Energetic few-cycle pulses by polarization-encoding in Ti:Sapphire: on the compression, carrier-envelope phase stability and decoding efficiency", SPIE Optics + Optoelectronics 2019, Prague, Czech Republic, 1-4 April 2019

[O8] M. Kurucz, Sz. Toth, R. Flender, L. Haizer, B. Kiss, B. Perseille, E. Cormier, "Dispersive Fourier transform based single-shot CEP drift measurement at arbitrary repetition rate", CLEO/Europe 2019, Munich, Germany, 23-27 June 2019

[O9] Sz. Toth, R. S. Nagymihály, A. Andrianov, B. Kiss, R. Flender, M. Kurucz, L. Haizer, E. Cormier, K. Osvay, "Conceptual study of a 1 kHz 10 mJ-class mid-IR OPCPA system with thermal aspects", UFO, Bol, Croatia, 6-11 October 2019

[O10] K. Osvay, A. Borzsonyi, H. Cao, V. Chvykov, E. Cormier, R. Flender, P. Jojart, M. Kalashnikov, B. Kiss, M. Kurucz, N. Khodakovskiy, R. Lopez-Martens, R. S. Nagymihaly, V. Pajer, S. Toth, "Few cycle, phase controlled laser developments for ELI-ALPS", CLEO 2020, San Jose, California, USA, 11-15 May 2020

[O11] A. Borzsonyi, E. Cormier, R. Lopez-Martens, M. Kalashnikov, B. Kiss, P. Jojart, J. Csontos, S. Toth, N. Khodakovskiy, R. Nagymihaly, R. Flender, M. Kurucz, I. Seres, Z. Varallyay, K. Varju, G. Szabo, "Operation experiences and further developments of the few-cycle, high average power lasers of ELI-ALPS", ASSL, OSA Virtual Event, 13-16 October 2020

[O12] M. Kurucz, R. Flender, L. Haizer, R. S. Nagymihaly, E. Cormier, B. Kiss, "Sub-two-cycle pulses in the mid-IR based on thin plate compression at high average power", HILAS, OSA Virtual Event, 16-20 November 2020

[O13] B. Kiss, R. Flender, M. Kurucz, T. Somoskoi, E. Cormier, "Nonlinear materials for efficient mid-IR few cycle pulse compression", SPIE Laser Damage, Rochester, New York, USA, 17-20 October 2021

7.4. Conference poster presentations

[P1] B. Kiss, R. Flender, Cs. Vass, "Fabrication of micron and submicron period metal reflection gratings by imprinting technique", LPM 2013, Niigata, Japan, 23-26 July 2013

[P2] Cs. Vass, B. Kiss, R. Flender, J. Kopniczky, F. Ujhelyi, "Polarizer fabrication by metal evaporated fused silica surface relief gratings", COLA 2013, Ischia, Italy, 6-11 October 2013

[P3] B. Kiss, R. Flender, Cs. Vass, K. Osvay, "Time-resolved study on grating formation in polycarbonate", DOC 2014 / Laserlab III. Training School, Riga, Latvia, 9-12 April 2014

[P4] B. Kiss, R. Flender, J. Kopniczky, F. Ujhelyi, Cs. Vass, "Fabrication of polarizer by metal evaporation of fused silica relief gratings", LPM 2014, Vilnius, Lithuania, 17-20 June 2014

[P5] R. Flender, Cs. Vass, B. Kiss, K. Osvay, "Polimerekbe készített optikai rácsok kialakulásának időbontott vizsgálata", Kvantumelektronika 2014, Budapest, Hungary, 28 November 2014

[P6] Cs. Vass, B. Kiss, R. Flender, Z. Felhazi, F. Ujhelyi, K. Osvay, "Optikai rácsok készítése lézeres eljárásokkal" Kvantumelektronika 2014, Budapest, Hungary, 28 November 2014

[P7] Sz. Toth, R. Flender, R. S. Nagymihaly, P. Jojart, A. Andrasik, A. Borzsonyi, K. Osvay, "Modelling and development of an 80 MHz repetition rate tunable OPCPA system for in-vivo deep brain imaging", The 7th EPS-QEOD Europhoton Conference: Solid State, Fiber and Waveguide Coherent Light Sources, Vienna, Austria, 21-26 August 2016

[P8] Sarosi K., Flender R., Borzsonyi A., Chikan V., "Aszimmetrikus levegőplazmában keltett terahertzes rövidimpulzusok vizsgálata", Magyar Fizikus Vándorgyűlés 2016, Szeged, Hungary, 24-27 August 2016

[P9] Sz. Toth, R. S. Nagymihaly, P. Jojart, R. Flender, A. Andrasik, A. Borzsonyi, K. Osvay, "80 MHz ismétlési frekvencián működő optikai parametrikus erősítő fejlesztése", Magyar Fizikus Vándorgyűlés 2016, Szeged, Hungary, 24-27 August 2016

[P10] Borzsonyi A., Farkas B., Kiss B., Kovacs M., Flender R., Jojart P., Vass Cs., Kovacs A. P., Varju K., Osvay K., "TeWaTi felhasználói lézerlaboratórium: út az ELI-ALPS lehetőségeihez", Magyar Fizikus Vándorgyűlés 2016, Szeged, Hungary, 24-27 August 2016

[P11] Sz. Toth, R. S. Nagymihaly, P. Jojart, A. Andrasik, R. Flender, A. Borzsonyi, K. Osvay, "Development of a 10 W 80 MHz repetition rate amplifier for few cycle pulses", ICUIL 2016, Montebello, Canada, 11-16 September 2016

[P12] R. Flender, K. Sarosi, A. Borzsonyi, V. Chikan, "The impact of dispersion of the ultrashort light pulses on the THz radiation from asymmetric air plasmas", ELI-ALPS User Workshop 2016, Szeged, Hungary, 10-11 November 2016

[P13] A. Andrasik, Sz. Toth, R. S. Nagymihaly, P. Jojart, R. Flender, A. Borzsonyi, K. Osvay, "Development of few cycle Ti:Sapphire and NOPA amplifiers at 80 1m1hz repetition rate", SPIE Optics + Optoelectronics 2017, Prague, Czech Republic, 24-27 April 2017

[P14] R. Polanek, E. R. Szabo, T. Tokes, Z. I. Szabo, Sz. Brunner, M. Kovacs, R. Flender, B. Kiss, A. Borzsonyi, V. Kurti, E. Huszar, K. Hideghety, K. Osvay, "Study of biological effects of femtosecond IR laser beam filamentation for cancer therapy", SPIE Optics + Optoelectronics 2017, Prague, Czech Republic, 24-27 April 2017

[P15] R. Flender, K. Sarosi, A. Borzsonyi, V. Chikan, "The impact of GDD and phase difference of ultrashort light pulses in the THz radiation generation from two-color symmetric air plasma", ICEL 2017, Szeged, Hungary, 6-9 November 2017

[P16] V. Kurti, R. Polanek, R. Flender, E. R. Szabo, T. Tokes, Sz. Brunner, Z. I. Szabo, M. Kovacs, A. Borzsonyi, K. Hideghety, K. Osvay, "Study of biological effects of femtosecond IR laser beam filamentation for cancer therapy", EUCALL Workshop: Biology at Advanced Laser Light Sources, Hamburg, Germany, 30 November – 1 December 2017

[P17] Flender R., Sarosi K., Petracs E., Borzsonyi A., Chikan V., "A másod- és magasabb rendű diszperzió hatása a kétszínű lézerrel levegőplazmában keltett THz-es impulzusra", Kvantumelektronika 2018, Budapest, Hungary, 15 June 2018

[P18] R. Flender, K. Sarosi, E. Petracs, A. Borzsonyi, V. Chikan, "The impact of dispersion and phase difference of ultrashort light pulses on the THz intensity generated from two-color asymmetric air plasma", LAMELIS Workshop 2018, Szeged, Hungary, 20 July 2018

[P19] V. Kurti, R. Polanek, R. Flender, A. Borzsonyi, E. R. Szabo, T. Tokes, Z. I. Szabo, K. Hideghety, K. Osvay, "Study of ionization effects of femtosecond infrared laser beam filamentation for cancer therapy", LAMELIS Workshop 2018, Szeged, Hungary, 20 July 2018

[P20] R. Flender, K. Sarosi, E. Petracs, A. Borzsonyi, V. Chikan, "The impact of dispersion and phase difference of ultrashort light pulses on the THz intensity generated from two-color asymmetric air plasma", ELISS 2018, Szeged, Hungary, 27-31 August 2018

[P21] V. Kurti, R. Polanek, R. Flender, A. Borzsonyi, E. R. Szabo, T. Tokes, Z. I. Szabo, K. Hideghety, K. Osvay, "Study of ionization effects of femtosecond infrared laser beam filamentation for cancer therapy", ELISS 2018, Szeged, Hungary, 27-31 August 2018

[P22] B. Kiss, Sz. Toth, M. Kurucz, L. Haizer, R. Flender, E. Cormier, K. Osvay, "Few-cycle mid-infrared optical parametric chirped pulse amplifier at ELI-ALPS" ELISS 2018, Szeged, Hungary, 27-31 August 2018

[P23] R. S. Nagymihaly, H. Cao, P. Jojart, V. Zuba, R. Flender, O. Antipov, I. Seres, A. Borzsonyi, V. Chvykov, K. Osvay, M. Kalashnikov, "Gain induced phase changes in Ti:Sapphire: key to phase stability of ultra-broadband laser amplification", ICUIL 2018, Lindau, Germany, 9-14 September 2018

[P24] R. Flender, B. Kiss, A. Borzsonyi, V. Chikan, "Numerical simulations of THz generation with two-color mid-infrared laser pulse and relative phase control", CLEO/Europe 2019, Munich, Germany, 23-27 June 2019

[P25] R. Flender, A. Borzsonyi, V. Chikan, "Theoretical investigation of the optimal nonlinear crystal thickness for THz generation from two-color laser pulse ionized gas under different laser pulse parameters", CLEO/Europe 2019, Munich, Germany, 23-27 June 2019

[P26] Sz. Toth, R. S. Nagymihaly, R. Flender, B. Kiss, M. Kurucz, L. Haizer, E. Cormier, K. Osvay, "Design of a 10 kHz mJ-level mid-IR OPCPA system", CLEO/Europe 2019, Munich, Germany, 23-27 June 2019

[P27] R. Flender, M. Kurucz, L. Haizer, R. S. Nagymihaly, Sz. Toth, A. Borzsonyi, E. Cormier, B. Kiss, "Two-cycle pulses in the mid-IR based on hybrid thin plate compression at high average power", UFO, Bol, Croatia, 6-11 October 2019

[P28] M. Kurucz, Sz. Toth, R. Flender, L. Haizer, B. Kiss, B. Perseille, E. Cormier, "High-accuracy single-shot CEP noise measurement at arbitrary repetition rate", UFO, Bol, Croatia, 6-11 October 2019

[P29] R. Flender, B. Kiss, A. Borzsonyi, V. Chikan, "Numerical simulations of terahertz pulse generation with two-color laser pulses in the 2.15–15.15 μm spectral range", ICEL, Prague, Czech Republic, 21-25 October 2019

[P30] M. Kurucz, R. Flender, L. Haizer, B. Kiss, R. S. Nagymihaly, Sz. Toth, E. Cormier, "Two-cycle pulses in the mid-IR based on hybrid thin plate compression at high average power", ICEL, Prague, Czech Republic, 21-25 October 2019

[P31] M. Kurucz, Sz. Toth, R. Flender, L. Haizer, B. Kiss, B. Perseille, E. Cormier, "High-accuracy single-shot CEP noise measurement at arbitrary repetition rate", ICEL, Prague, Czech Republic, 21-25 October 2019

[P32] R. Flender, A. Borzsonyi, B. Kiss, V. Chikan, "Numerical simulations of terahertz pulse generation with two-color laser pulse in the 2.15-15.15 μm spectral range", HILAS, OSA Virtual Event, 16-20 November 2020

[P33] R. Flender, A. Borzsonyi, B. Kiss, V. Chikan, “Comparative study of terahertz pulse generation from one- and two-color laser pulses in the mid-infrared spectral range”, HILAS, OSA Virtual Event, 16-20 November 2020

[P34] A. Andrasik, R. Flender, J. Budai, T. Szorenyi, B. Hopp, “Characterization of plasma reflectivity response of optical glasses processed by 34 fs pulses: analysis in the context of ablation parameters”, Kvantumelektronika, Szeged, Hungary, 28 January 2021

[P35] A. Andrasik, R. Flender, J. Budai, T. Szorenyi, B. Hopp, “Surface processing of optical glasses with 34 fs pulses: ablation thresholds and crater shape”, Kvantumelektronika, Szeged, Hungary, 28 January 2021

[P36] R. Flender, A. Borzsonyi, V. Chikan, ”Numerical simulation of THz pulse generation with two-color laser pulses in the 2.15–15.15 μm spectral range”, Kvantumelektronika, Szeged, Hungary, 28 January 2021

[P37] R. Flender, A. Borzsonyi, V. Chikan, ”Numerical study of terahertz pulse generation from few-cycle laser pulses in the mid-IR spectral range”, Kvantumelektronika, Szeged, Hungary, 28 January 2021

[P38] M. Kurucz, R. Flender, T. Grosz, A. Borzsonyi, U. Gimzevskis, A. Samalius, D. Hoff, B. Kiss, “High resolution spectrally resolved interferometry in the mid-IR”, CLEO Europe, Munich, Germany, 21-25 June 2021

[P39] R. Flender, A. Borzsonyi, V. Chikan, “The role of asymmetry in mid-infrared, few-cycle pulses during terahertz pulse generation”, OTST 2022, Budapest, Hungary, 19-24 June 2022

8. References

[1] T. H. Maiman, ”Stimulated Optical Radiation in Ruby”, Nature 187, 493-494 (1960)
DOI: https://doi.org/10.1038/187493a0

[2] W. Kaiser, and C. G. B. Garrett, “Two-Photon Excitation in CaF_2: Eu^{2+}”, Physical Review Letters 7(6), 229-231 (1961)
DOI: https://doi.org/10.1103/PhysRevLett.7.229

[3] P. A. Franken, A. E. Hill, C. W. Peters, and G. Weinreich, “Generation of Optical Harmonics”, Physical Review Letters 7(4), 118-119 (1961)
DOI: https://doi.org/10.1103/PhysRevLett.7.118

[4] https://www.nobelprize.org/prizes/physics/1971/summary/

[5] https://www.nobelprize.org/prizes/physics/2017/summary/

[6] https://www.nobelprize.org/prizes/physics/2018/summary/

[7] M. Bass, P. A. Franken, A. E. Hill, C. W. Peters, and G. Weinreich, “Optical Mixing”, Physical Review Letters 8(1), 18-18 (1962)
DOI: https://doi.org/10.1103/PhysRevLett.8.18

[8] R. C. Miller, and A. Savage, “Harmonic Generation and Mixing of $CaWO_4$: Nd^{3+} and Ruby Pulsed Laser Beams in Piezoelectric Crystals”, Physical Review Journals Archive 128(5), 2175-2179 (1962)
DOI: https://doi.org/10.1103/PhysRev.128.2175

[9] A. W. Smith, and N. Braslau, “Observation of an Optical Difference Frequency”, Journal of Applied Physics 34(7), 2105-2106 (1963)
DOI: https://doi.org/10.1063/1.1729748

[10] S. A. Akhmanov, A. I. Kovrigin, A. S. Piskarskas, V. V. Fadeev, and R. V. Khokhlov, “Observation of Parametric Amplification in the Optical Range”, Journal of Experimental and Theoretical Physics 2(7), 191-193 (1965)

[11] J. A. Giordmaine, and Robert C. Miller, “Tunable Coherent Parametric Oscillation in $LiNbO_3$ at Optical Frequencies”, Physical Review Letters 14(24), 973-976 (1965)
DOI: https://doi.org/10.1103/PhysRevLett.14.973

[12] D. Strickland, and G. Mourou, “Compression of amplified chirped optical pulses”, Optics Communications 55(6), 447-449 (1985)
DOI: https://doi.org/10.1016/0030-4018(85)90151-8

[13] H. Fattahi, H. G. Barros, M. Gorjan, T. Nubbemeyer, B. Alsaif, C. Y. Teisset, M. Schultze, S. Prinz, M. Haefner, M. Ueffing, A. Alismail, L. Vamos, A. Schwarz, O. Pronin, J. Brons, X. T. Geng, G. Arisholm, M. Ciappina, V. S. Yakovlev, D.-E. Kim, A. M. Azzeer, N. Karpowicz, D. Sutter, Zs. Major, T. Metzger, and F. Krausz, “hird-generation femtosecond technology”, Optica 1(1), 45-63 (2014)
DOI: https://doi.org/10.1364/OPTICA.1.000045

[14] A.Dubietis, G. Jonusauskas, and A. Piskarskas, “Powerful femtosecond pulse generation by chirped and stretched pulse parametric amplification in BBO crystal”, Optics Communications 88(4-6), 437-440 (1992)
DOI: https://doi.org/10.1016/0030-4018(92)90070-8

[15] M. Baudisch, B. Wolter, M. Pullen, M. Hemmer, and J. Biegert, “High power multi-color OPCPA source with simultaneous femtosecond deep-UV to mid-IR outputs”, Optics Letters 41(15), 3583-3586 (2016)
DOI: https://doi.org/10.1364/OL.41.003583

[16] Zs. Heiner, V. Petrov, and M. Mero, “Compact, high-repetition-rate source for broadband sum-frequency generation spectroscopy”, APL Photonics 2(6), 066102 (2017)
DOI: https://doi.org/10.1063/1.4983691

[17] M. Mero, Zs. Heiner, V. Petrov, H. Rottke, F. Branchi, G. M. Thomas, and M. J. J. Vrakking, “43 W, 1.55 μm and 12.5 W, 3.1 μm dual-beam, sub-10 cycle, 100 kHz optical parametric chirped pulse amplifier”, Optics Letters 43(21), 5246-5249 (2018)
DOI: https://doi.org/10.1364/OL.43.005246

[18] A. Baltuska, T. Fuji, and T. Kobayashi, “Controlling the Carrier-Envelope Phase of Ultrashort Light Pulses with Optical Parametric Amplifiers”, Physics Review Letters 88(13), 133901 (2002)
DOI: https://doi.org/10.1103/PhysRevLett.88.133901

[19] B. W. Mayer, C. R. Phillips, L. Gallmann, and U. Keller, “Mid-infrared pulse generation via achromatic quasi-phase-matched OPCPA”, Optics Express 22(17), 20798-20808 (2014),
DOI: https://doi.org/10.1364/OE.22.020798

[20] U. Elu, M. Baudisch, H. Pires, F. Tani, M. H. Frosz, F. Köttig, A. Ermolov, P. St.J. Russell, and J. Biegert, “High average power and single-cycle pulses from a mid-IR optical parametric chirped pulse amplifier”, Optica 4(9), 1024-1029 (2019)
DOI: https://doi.org/10.1364/OPTICA.4.001024

[21] N. Thiré, R. Maksimenka, B. Kiss, C. Ferchaud, G. Gitzinger, T. Pinoteau, H. Jousselin, S. Jarosch, P. Bizouard, V. Di Pietro, E. Cormier, K. Osvay, and N. Forget, “Highly stable, 15 W, few-cycle, 65 mrad CEP-noise mid-IR OPCPA for statistical physics”, Optics Express 26(21), 26907-26915 (2018)
DOI: https://doi.org/10.1364/OE.26.026907

[22] T. Popmintchev, M.-C. Chen, D. Popmintchev, P. Arpin, S. Brown, S. Alisauskas, G. Andriukaitis, T. Balciunas, O. D. Mucke, A. Pugzlys, A. Baltuska, B. Shim, S. E. Schrauth, A. Gaeta, C. Hernandez-Gercia, L. Plaja, A. Becker, A. Jaron-Becker, M. M. Murnane, and H. C. Kapteyn, “Bright Coherent Ultrahigh Harmonics in the keV X-ray Regime from Mid-Infrared Femtosecond Lasers”, Science 336 (6068), 1287-1291 (2012)
DOI: https://doi.org/10.1126/science.1218497

[23] M. Clerici, M. Peccianti, B. E. Schmidt, L. Caspani, M. Shalaby, M. Giguère, A. Lotti, A. Couairon, F. Legare, T. Ozaki, D. Faccio, and R. Morandotti, "Wavelength Scaling of Terahertz Generation by Gas Ionization", Physical Review Letters 110(25), 253901 (2013)
DOI: https://doi.org/10.1103/PhysRevLett.110.253901

[24] A. Nguyen, P. Gonzalez de Alaiza Martínez, J. Dechard, I. Thiele, I. Babushkin, S. Skupin, and L. Berge, "Spectral dynamics of THz pulses generated by two-color laser filaments in air: the role of Kerr nonlinearities and pump wavelength", Optics Express 25(5), 4720-4740 (2017),
DOI: https://doi.org/10.1364/OE.25.004720

[25] A. Nguyen, P. G. de Alaiza Martínez, I. Thiele, S. Skupin, and L. Berge, "Broadband terahertz radiation from two-color mid- and far-infrared laser filaments in air", Physical Review A 97(6), 063839 (2018)
DOI: https://doi.org/10.1103/PhysRevA.97.063839

[26] V. Y. Fedorov, and S. Tzortzakis, "Extreme THz fields from two-color filamentation of midinfrared laser pulses", Physical Review A 97(6), 063842 (2018)
DOI: https://doi.org/10.1103/PhysRevA.97.063842

[27] V. Y. Fedorov, and S. Tzortzakis, "Optimal wavelength for two-color filamentation-induced terahertz sources", Optics Express 26(24), 31150-31159 (2018)
DOI: https://doi.org/10.1364/OE.26.031150

[28] A. Nguyen, K. J. Kaltenecker, J.-C. Delagnes, B. Zhou, E. Cormier, N. Fedorov, R. Bouillaud, D. Descamps, I. Thiele, S. Skupin, P. U. Jepsen, and L. Berge, "Wavelength scaling of terahertz pulse energies delivered by two-color air plasmas", Optics Letters 44(6), 1488-1491 (2019)
DOI: https://doi.org/10.1364/OL.44.001488

[29] A. D. Koulouklidis, C. Gollner, V. Shumakova, V. Y. Fedorov, A. Pugzlys, A. Baltuska, and S. Tzortzakis, "Observation of extremely efficient terahertz generation from mid-infrared two-color laser filaments", Nature Communications 11, 292 (2020)
DOI: https://doi.org/10.1038/s41467-019-14206-x

[30] R. Flender, A. Borzsonyi, and V. Chikan, "Phase-controlled, second-harmonic-optimized terahertz pulse generation in nitrogen by infrared two-color laser pulses" Journal of the Optical Society of America B 37(6), 1838-1846 (2020)
DOI: https://doi.org/10.1364/JOSAB.391123

[31] M. Hemmer, M. Baudisch, A. Thai, A. Couairon, and J. Biegert, "Self-compression to sub-3-cycle duration of mid-infrared optical pulses in dielectrics", Optics Express 21(23), 28095-28102 (2013)
DOI: https://doi.org/10.1364/OE.21.028095

[32] V. Shumakova, P. Malevich, S. Alisauskas, A. Voronin, A. M. Zheltikov, D. Faccio, D. Kartashov, A. Baltuska, and A. Pugzlys, "Multi-millijoule few-cycle mid-infrared pulses through nonlinear self-compression in bulk", Nature Communications 7, 12877 (2016)
DOI: https://doi.org/10.1038/ncomms12877

[33] A. Marcinkeviciute, N. Garejev, R. Suminas, G. Tamosauskas, and A. Dubietis, "A compact, self-compression-based sub-3 optical cycle source in the 3-4 μm spectral range", Journal of Optics 19(10), 105505 (2017)
DOI: https://doi.org/10.1088/2040-8986/aa873b

[34] F. Lu, P. Xia, Y. Matsumoto, T. Kanai, N. Ishii, and J. Itatani, "Generation of sub-two-cycle CEP-stable optical pulses at 3.5 μm from a KTA-based optical parametric amplifier with multiple-plate compression", Optics Letters 43(11), 2720-2723 (2018)
DOI: https://doi.org/10.1364/OL.43.002720

[35] M. Kurucz, R. Flender, L. Haizer, R. S. Nagymihaly, W. Cho, K. T. Kim, Sz. Toth, E. Cormier, and B. Kiss, "2.3-cycle mid-infrared pulses from hybrid thin-plate postcompression at 7 W average power", Optics Communications 472, 126035 (2020)
DOI: https://doi.org/10.1016/j.optcom.2020.126035

[36] R. Flender, M. Kurucz, T. Grosz, A. Borzsonyi, U. Gimzevskis, A. Samalius, D. Hoff, and B. Kiss, "Dispersive mirror characterization and application for mid-infrared postcompression", Journal of Optics 23(6), 065501 (2021)
DOI: https://doi.org/10.1088/2040-8986/abf88e

[37] R. Szipöcs, K. Ferencz, C. Spielmann, and F. Krausz, "Chirped multilayer coatings for broadband dispersion control in femtosecond lasers", Optics Letters 19(3), 201-203 (1994)
DOI: https://doi.org/10.1364/OL.19.000201

[38] R. Szipőcs, and A. Kőházi-Kis, "Theory and design of chirped dielectric laser mirrors", Applied Physics B 65(2), 115-135 (1997)
DOI: https://doi.org/10.1007/s003400050258

[39] E. J. Mayer, J. Möbius, A. Euteneuer, W. W. Rühle, and R. Szipőcs, "Ultrabroadband chirped mirrors for femtosecond lasers", Optics Letters 22(8), 528-530 (1997)
DOI: https://doi.org/10.1364/OL.22.000528

[40] V. Pervak, F. Krausz, and A. Apolonski, "Dispersion control over the ultraviolet–visible–near-infrared spectral range with HfO_2/SiO_2 -chirped dielectric multilayers", Optics Letters 32(19), 1183-1185 (2007)
DOI: https://doi.org/10.1364/OL.32.001183

[41] V. Pervak, C. Teisset, A. Sugita, S. Naumov, F. Krausz, and A. Apolonski, "High-dispersive mirrors for femtosecond lasers", Optics Express 16(14), 10220-10233 (2008)
DOI: https://doi.org/10.1364/OE.16.010220

[42] D. Grischkowsky, S. Keiding, M. van Exter, and Ch. Fattinger, "Far-infrared time-domain spectroscopy with terahertz beams of dielectrics and semiconductors", Journal of the Optical Society of America B 7(10), 2006-2015 (1990)
DOI: https://doi.org/10.1364/JOSAB.7.002006

[43] K. Y. Kim, J. H. Glownia, A. J. Taylor, and G. Rodriguez, "Terahertz emission from ultrafast ionizing air in symmetry-broken laser fields", Optics Express 15(8), 4577-4584 (2007)
DOI: https://doi.org/10.1364/OE.15.004577

[44] K.-Y. Kim, J. H. Glownia, A. J. Taylor, and G., "High-Power Broadband Terahertz Generation via Two-Color Photoionization in Gases", IEEE Journal of Quantum Electronics 48(6), 797-805 (2012)
DOI: https://doi.org/10.1109/JQE.2012.2190586

[45] D. J. Cook, and R. M. Hochstrasser, "Intense terahertz pulses by four-wave rectification in air", Optics Letters 25(16), 1210-1212 (2000)
DOI: https://doi.org/10.1364/OL.25.001210

[46] W. Herschel, "Experiments on the refrangibility of the invisible rays of the sun", Philosophical Transactions of the Royal Society of London 90, 284-292 (1800)
DOI: https://doi.org/10.1098/rstl.1800.0015

[47] P. R. Griffiths, and J. A. De Haseth, "Fourier Transform Infrared Spectrometry (2nd Edition)", Published by John Wiley & Sons, Hoboken, New Jersey, USA (2007)
ISBN: 9780470106297

[48] V. P. Gupta, an Y. Ozaki, "Molecular and Laser Spectroscopy, Advances and Applications: Volume 2 (1st Edition)", Published by Elsevier, Amsterdam, Netherlands (2020)
ISBN: 9780128188712

[49] M. Baudelet, "Laser Spectroscopy for Sensing Fundamentals, Techniques and Applications", Published by Woodhead Publishing, Cambridge, UK, (2014)
ISBN: 9780857098733

[50] R. Boyd, "Nonlinear Optics (3rd Edition)", Published by Academic Press, Cambridge, Massachusetts, USA (2008)
ISBN: 9780080485966

[51] R. Y. Chiao, E. Garmire, and C. H. Townes, "Self-Trapping of Optical Beams", Physical Review Letters 13(15), 479-482 (1964)
DOI: https://doi.org/10.1103/PhysRevLett.13.479

[52] P. L. Kelley, "Self-Focusing of Optical Beams", Physical Review Letters 15(26), 1005-1008 (1965)
DOI: https://doi.org/10.1103/PhysRevLett.15.1005

[53] P. Lallemand, and N. Bloembergen, "Self-Focusing of Laser Beams and Stimulated Raman Gain in Liquids", Physical Review Letters 15(26), 1010-1012 (1965)
DOI: https://doi.org/10.1103/PhysRevLett.15.1010

[54] E. Garmire, R. Y. Chiao, and C. H. Townes, "Dynamics and Characteristics of the Self-Trapping of Intense Light Beams", Physical Review Letters 16(9), 347-349 (1966)
DOI: https://doi.org/10.1103/PhysRevLett.16.347

[55] G. Fibich, and A. L. Gaeta, "Critical power for self-focusing in bulk media and in hollow waveguides", Optics Letters 25(5), 335-337 (2000)
DOI: https://doi.org/10.1364/OL.25.000335

[56] F. Shimizu, “Frequency Broadening in Liquids by a Short Light Pulse”, Physical Review Letters 19(19), 1097-1100 (1967)
DOI: https://doi.org/10.1103/PhysRevLett.19.1097

[57] N. Thiré, R. Maksimenka, B. Kiss, C. Ferchaud, P. Bizouard, E. Cormier, K. Osvay, and N. Forget, “4-W, 100-kHz, few-cycle mid-infrared source with sub-100-mrad carrier-envelope phase noise”, Optics Express 25(2), 1505-1514 (2017)
DOI: https://doi.org/10.1364/OE.25.001505

[58] D. J. Kane, and R. Trebino, “Characterization of arbitrary femtosecond pulses using frequency-resolved optical gating”, IEEE Journal of Quantum Electronics 29(2), 571-579 (1993)
DOI: https://doi.org/10.1109/3.199311

[59] K. W. DeLong, Rick Trebino, J. Hunter, and W. E. White, “Frequency-resolved optical gating with the use of second-harmonic generation”, Journal of the Optical Society of America B 11(11), 2206-2215 (1994)
DOI: https://doi.org/10.1364/JOSAB.11.002206

[60] R. Trebino, K. W. DeLong, D. N. Fittinghoff, J. N. Sweetser, M. A. Krumbügel, B. A. Richman, and D. J. Kane, “Measuring ultrashort laser pulses in the time-frequency domain using frequency-resolved optical gating”, Review of Scientific Instruments 68(9), 3277-3295 (1998)
DOI: https://doi.org/10.1063/1.1148286

[61] V. A. Andreeva, O. G. Kosareva, N. A. Panov, D. E. Shipilo, P. M. Solyankin, M. N. Esaulkov, P. González de Alaiza Martínez, A. P. Shkurinov, V. A. Makarov, L. Bergé, and S. L. Chin, “Ultrabroad Terahertz spectrum generation from an air-based filament plasma”, Physics Review Letters 116(6), 063902 (2016)
DOI: https://doi.org/10.1103/PhysRevLett.116.063902

[62] H. Wang, Y. Bai, E. Wu, Z. Wang, P. Liu, and C. Liu, “Terahertz necklace beams generated from two-color vortex-laser-induced air plasma”, Physics Review A 98(10), 013857 (2018)
DOI: https://doi.org/10.1103/PhysRevA.98.013857

[63] K. Kato, F. Tanno, and N. Umemura, “Sellmeier and thermo-optic dispersion formulas for GaSe”, Applied Optics 52(11), 2325-2328 (2013)
DOI: https://doi.org/10.1364/AO.52.002325

[64] K. R. Allakhverdiev, M. Ö. Yetis, S. Özbek, T. K. Baykara and E. Yu. Salaev, “Effective nonlinear GaSe crystal. Optical properties and applications”, Laser Physics 19(5), 1092-1104 (2009)
DOI: https://doi.org/10.1134/S1054660X09050375

[65] H. Kogelnik and T. Li, “Laser beams and resonators”, Applied Optics 5(10), 1550-1569 (1966)
DOI: https://doi.org/10.1364/AO.5.001550

[66] A. A. Voronin and A. M. Zheltikov, “The generalized Sellmeier equation for air”, Scientific Reports 7, 46111 (2017)
DOI: https://doi.org/10.1038/srep46111

[67] M. V. Ammosov, N. B. Delone, and V. P. Krainov, “Tunnel ionization of complex atoms and of atomic ions in an altering electromagnetic field”, Journal of Experimental and Theoretical Physics 64(6), 2008-2019 (1986)

[68] G. Rodriguez, C.W. Siders, Chunlei Guo, and A.J. Taylor, “Coherent ultrafast MI-FROG spectroscopy of optical field ionization in molecular H_2, N_2, and O_2”, IEEE Journal of Selected Topics in Quantum Electronics, 7(4), 579-591 (2001)
DOI: https://doi.org/10.1109/2944.974229

[69] D. Jang, R. M. Schwartz, D. Woodbury, J. Griff-McMahon, A. H. Younis, H. M. Milchberg, and Ki-Yong Kim, “Efficient terahertz and Brunel harmonic generation from air plasma via mid-infrared coherent control”, Optica 6(10), 1338-1341 (2019)
DOI: https://doi.org/10.1364/OPTICA.6.001338

[70] A. A. Ushakov, P. A. Chizhov, V. A. Andreeva, N. A. Panov, D. E. Shipilo, M. Matoba, N. Nemoto, N. Kanda, K. Konishi, V. V. Bukin, M. Kuwata-Gonokami, O. G. Kosareva, S. V. Garnov, and A. B. Savel’ev, “Ring and unimodal angular-frequency distribution of THz emission from two-color femtosecond plasma spark”, Optics Express 26(14), 18202-18213 (2018)
DOI: https://doi.org/10.1364/OE.26.018202

[71] K. Y. Kim, A. J. Taylor, J. H. Glownia, and G. Rodriguez, “Coherent control of terahertz supercontinuum generation in ultrafast laser–gas interactions”, Nature Photonics 2, 605-609 (2008)
DOI: https://doi.org/10.1038/nphoton.2008.153

[72] M. Kress, T. Löffler, S. Eden, M. Thomson, and H. G. Roskos, “Terahertz-pulse generation by photoionization of air with laser pulses composed of both fundamental and second-harmonic waves”, Optics Letters 29(10), 1120-1122 (2004)
DOI: https://doi.org/10.1364/OL.29.001120

[73] T. I. Oh, Y. S. You, N. Jhajj, E. W. Rosenthal, H. M. Milchberg, and K. Y. Kim, “Scaling and saturation of high-power terahertz radiation generation in two-color laser filamentation”, Applied Physics Letters 102(20), 201113 (2013)
DOI: https://doi.org/10.1063/1.4807790

[74] T. I. Oh, Y. J. Yoo, Y. S. You, and K. Y. Kim, “Generation of strong terahertz fields exceeding 8 MV/cm at 1 kHz and real-time beam profiling”, Applied Physics Letters 105(4), 041103 (2014)
DOI: https://doi.org/10.1063/1.4891678

[75] Y.-J. Yoo, D. Jang, and K.-Y. Kim, “Highly enhanced terahertz conversion by two-color laser filamentation at low gas pressures”, Optics Express 27(16), 22663-22673 (2019)
DOI: https://doi.org/10.1364/OE.27.022663

[76] Z. Zhang, Y. Chen, L. Yang, X. Yuan, F. Liu, M. Chen, J. Xu, Z. Sheng, and J. Zhang, “Dual-frequency terahertz emission from splitting filaments induced by lens tilting in air”, Applied Physics Letters 105(10), 101110 (2014)
DOI: https://doi.org/10.1063/1.4895720

[77] Z. Zhang, N. Panov, V. Andreeva, Zhelin Zhang, A. Slepkov, D. Shipilo, M. D. Thomson, T.-J. Wang, I. Babushkin, A. Demircan, U. Morgner, Y. Chen, O. Kosareva, and A. Savel'ev, "Optimum chirp for efficient terahertz generation from two-color femtosecond pulses in air", Applied Physics Letter 113(24), 241103 (2018)
DOI: https://doi.org/10.1063/1.5053893

[78] R. Flender, K. Sarosi, E. Petracs, A. Borzsonyi, and V. Chikan, "Control of THz field waveform emitted from air plasma by chirping two-color laser pulses", Optics Communications 436, 222-226 (2019)
DOI: https://doi.org/10.1016/j.optcom.2018.12.020

[79] R. Flender, A. Borzsonyi, and V. Chikan, "The role of asymmetry in few-cycle, mid-IR pulses during THz pulse generation", Journal of Optics 24(4), 045502 (2022)
DOI: https://doi.org/10.1088/2040-8986/ac5289

[80] Y,-S. Lee, "Principles of Terahertz Science and Technology (1st Edition)", Published by Springer, New York City, New York, USA (2009)
ISBN: 9780387095400

[81] C. Sáinz, P. Jourdian, R. Escalona, and J. Calatroni, "Real time interferometric measurements of dispersion curves", Optics Communications 110(3-4), 381-390 (1994)
DOI: https://doi.org/10.1016/0030-4018(94)90442-1

[82] M. A. Galle, W. Mohammed, L. Qian, and P. W. E. Smith, "Single-arm three-wave interferometer for measuring dispersion of short lengths of fiber", Optics Express 15(25), 16896-16908 (2007)
DOI: https://doi.org/10.1364/OE.15.016896

[83] L. Lepetit, G. Chériaux, and M. Joffre, "Linear techniques of phase measurement by femtosecond spectral interferometry for applications in spectroscopy", Journal of the Optical Society of America B 12(12), 2467-2474 (1995)
DOI: https://doi.org/10.1364/JOSAB.12.002467

[84] Ch. Dorrer, "Influence of the calibration of the detector on spectral interferometry", Journal of the Optical Society of America B 16(7), 1160-1168 (1999)
DOI: https://doi.org/10.1364/JOSAB.16.001160

[85] Ch. Dorrer, N. Belabas, J.-P. Likforman, and M. Joffre, "Spectral resolution and sampling issues in Fourier-transform spectral interferometry", Journal of the Optical Society of America B 17(10), 1795-1802 (2000)
DOI: https://doi.org/10.1364/JOSAB.17.001795

[86] S. K. Debnath, M. P.Kothiyal, and S.-W. Kim, "Evaluation of spectral phase in spectrally resolved white-light interferometry: Comparative study of single-frame techniques", Optics and Lasers in Engineering 47(11), 1125-1130 (2009)
DOI: https://doi.org/10.1016/j.optlaseng.2009.06.014

[87] T. Grósz, A. P. Kovács, M. Kiss, and R. Szipőcs, “Measurement of higher order chromatic dispersion in a photonic bandgap fiber: comparative study of spectral interferometric methods”, Applied Optics 53(9), 1929-1937 (2014)
DOI: https://doi.org/10.1364/AO.53.001929

[88] M. Takeda, H. Ina, and S. Kobayashi, “Fourier-transform method of fringe-pattern analysis for computer-based topography and interferometry”, Journal of the Optical Society of America 72(1), 156-160 (1982)
DOI: https://doi.org/10.1364/JOSA.72.000156

[89] L. Huang, Q. Kemao, B. Pan, and A. K. Asundi, “Comparison of Fourier transform, windowed Fourier transform, and wavelet transform methods for phase extraction from a single fringe pattern in fringe projection profilometry”, Optics and Lasers in Engineering 48(2), 141-148 (2010)
DOI: https://doi.org/10.1016/j.optlaseng.2009.04.003

[90] H. H. Li, “Refractive index of alkaline earth halides and its wavelength and temperature derivatives”, Journal of Physical and Chemical Reference Data 9(1), 161-289 (1980)
DOI: https://doi.org/10.1063/1.555616

[91] W. S. Rodney, and I. H. Malitson, “Refraction and Dispersion of Thallium Bromide Iodide”, Journal of the Optical Society of America 46(11), 956-961 (1956)
DOI: https://doi.org/10.1364/JOSA.46.000956

[92] H. H. Li, “Refractive index of silicon and germanium and its wavelength and temperature derivatives”, Journal of Physical and Chemical Reference Data 9(3), 561-658 (1980)
DOI: https://doi.org/10.1063/1.555624

[93] D. E. Zelmon, D. L. Small, and R. Page, “Refractive-index measurements of undoped yttrium aluminum garnet from 0.4 to 5.0 μm”, Applied Optics 37(21), 4933-4935 (1998)
DOI: https://doi.org/10.1364/AO.37.004933

[94] I. E. Gordon, L. S. Rothman, C. Hill, R. V. Kochanov, Y. Tan, P. F. Bernath, M. Birk, V. Boudon, A. Campargue, K. V. Chance, B. J. Drouin, J.-M. Flaud, R. R. Gamache, J. T. Hodges, D. Jacquemart, V. I. Perevalov, A. Perrin, K. P. Shine, M.-A. H. Smith, J. Tennyson, G. C. Toon, H. Tran, V. G. Tyuterev, A. Barbe, A. G. Császár, V. M. Devi, T. Furtenbacher, J. J. Harrison, J.-M. Hartmann, A. Jolly, T. J. Johnson, T. Karman, I. Kleiner, A. A. Kyuberis, J. Loos, O. M. Lyulin, S. T. Massie, S. N. Mikhailenko, N. Moazzen-Ahmadi, H. S. P. Müller, O. V. Naumenko, A. V. Nikitin, O. L. Polyansky, M. Rey, M. Rotger, S. W. Sharpe, K. Sung, E. Starikova, S. A. Tashkun, J. Vander Auwera, G. Wagner, J. Wilzewski, P. Wcisło, S. Yu, and E. J. Zak, “The HITRAN2016 molecular spectroscopic database”, Journal of Quantitative Spectroscopy and Radiative Transfer 203, 3-69 (2017)
DOI: https://doi.org/10.1016/j.jqsrt.2017.06.038

[95] https://www.optoman.com/show-inner-content/page-146.html

[96] http://www.tydexoptics.com/products/thz_assemblies/thz_low_pass_filter/

[97] D. Eimerl, L. Davis, S. Velsko, E. K. Graham, and A. Zalkin, “Optical, mechanical, and thermal properties of barium borate”, Journal of Applied Physics 62(5), 1968-1983 (1987)
DOI: https://doi.org/10.1063/1.339536

[98] D. N. Nikogosyan, “Beta barium borate (BBO)”, Applied Physics A 52(6), 359-368 (1991)
DOI: https://doi.org/10.1007/BF00323647

[99] H. H. Li, “Refractive index of alkali halides and its wavelength and temperature derivatives”, Journal of Physical and Chemical Reference Data 5(2), 329-528 (1976)
DOI: https://doi.org/10.1063/1.555536